Microfluidic Separation of Blood Components through Deterministic Lateral Displacement

John Alan Davis

A Dissertation
Presented to the Faculty
of Princeton University
in Candidacy for the Degree
of Doctor of Philosophy

Recommended for Acceptance
by the Department of
Electrical Engineering
Advisor: James Sturm

September 2008

© Copyright by John Alan Davis, 2008.
All Rights Reserved

Abstract

Microfluidic devices provide a controlled platform for the manipulation and control of volumetric amounts of fluid. Primary applications of microfluidic devices include single-cell based analysis and nanoliter scale measurement of biological materials and living organisms. One method of separation of these biological components in such applications is based on size. By breaking a heterogeneous sample into several homogenous components, each individual component can be independently analyzed and/or manipulated.

Deterministic lateral displacement (DLD) is an emerging technique for separating particles based on size in a microfluidic environment. This technique shows great promise as a means to continuously separate particles smaller than the feature size of a microfluidic array. As can be appreciated, particles ideally travel one of two types of path within a microfabricated array of posts depending on their size. Thus, the microfluidic device employing the DLD technique functions like a continuously operable filter, separating large from small particles, or providing particle size measurement.

As a focus of this study, the separation of blood into its primary components is shown. White blood cell isolation with 100% accuracy and separation of red blood cells and platelets from blood plasma is demonstrated through the use of the DLD. Herein is included the use of traditional blood techniques, such as the flow cytometry, to confirm these results. The DLD techniques are explored and discussed, not only for blood, but for other types of particle separations through the development, analysis and testing for four different designs.

Acknowledgements

I would like to thank my advisors Jim Sturm and Bob Austin for keeping me on track. You were always a source of new and different perspectives to every problem. I greatly appreciate all of the help from the members of the Sturm and Austin labs especially David Inglis and Richard Huang.

I am grateful to David Lawrence and his whole research group at the Wadsworth Center, for helping me experiment in their lab and the use of their flow cytometer. I am indebted to Keith Morton for his help with etching, which saved me many trips to Cornell.

I have been blessed with a wonderful family that has been an unending source of support and encouragement. I especially want to thank my mom and dad for giving me strength to continue and hope to allow me to persevere. Finally, I give my deepest thanks to my wife Ethel, for her amazing love and support.

Contents

1 Introduction

Recent advancements in silicon integrated circuit technology produced drastic improvements to a variety of technology fields including biotechnology. The manufacture of smaller, cheaper, and more accurate devices, such as micron-size pumps, separators, and detectors are just a small sample of the contributions that microfabrication has provided.

Of particular importance is microfluidics or the use of microfabricated miniature devices to control and manipulate small volumes of fluid. These tiny devices, also referred to as "lab-on-a-chip," can for example be used to manipulate microorganisms, cells, proteins and even DNA. In other words, a series of experiments previously conducted in an entire lab, can now be performed using a single microfabricated chip.

As discussed hereinafter, microfabricated devices can be used to develop an improved method for separating microliter quantities of blood into its principle components, and separating white blood cells into their sub-types. To provide the full scope of the state of the technology, the following sections provide introductions to microfluidics and the blood analysis. The first subchapter 1.1 discusses a brief history of microfluidics, primarily focusing on separation technology while the second subchapter 1.2 discusses the current blood separation methods currently used in the medical field including advantages and disadvantages.

The final subchapters 1.3 and 1.4 will elaborate on the present work in microfluidic technology used on blood, as well as a number of microfluidic techniques under research, highlighting some of the advantages, and conclude with a brief introduction of the microfluidic device used in this thesis and a summary of each of the chapters.

1.1 Introduction to Microfluidics

Microfluidics entails fluids at volumes of a single a droplet, about 25 microliters. It consists of an area of fluid mechanics dealing with volumes large enough to still call a continuum, but small enough that surface tension, energy dissipation, and fluidic resistance start to dominate the system[1]. Microfluidics studies how fluid behavior changes, and how it can be worked with, and exploited for new applications.

Microfluidic devices are constructed using the same fabrication tools as computer chips including photosensitive polymers which are used to directly pattern a device in silicon, or to pattern silicon as a mold for a device in an elastomer such as polydimethylsiloxane (PDMS).

The first microfluidic device consisted of a working gas chromatograph on a silicon wafer by S. Terry *et al* [2] in 1979. In the early 90's an interest began in the fabrication of a micron-sized total analysis system (the μTAS)[3]. This μTAS could perform all kinds of functions including sample preparation, separation, mixing, chemical reactions and detection in an integrated microfluidic circuit. The creation of such devices is a major area of research today.

A number of these devices use some of the advantages that reducing the size provides. Faster temperature changes[4], ease in applying higher electric fields[5], reduced cost and easier use[6, 7] are all possible in a microfluidic device.

Separations are an important set of applications of microfluidic devices. Techniques for separation of cells play an important role in biology. Biological mixtures often consist of a wide variety of individual cell types, in varying concentrations. Scientists would like to study these individual components. An ideal separation technique should

be able to quickly differentiate a wide variety of components, from a small sample size, with low biological impact on the sample. [8]

The lab-on-a-chip technology is moving toward faster separations and analysis with more accessible devices. These devices have a wide range of biological applications like detection of biological weapons, and faster medical analysis[1, 9]. As the volumes analyzed become smaller, the lab-on-a-chip methods might be able to move from analysis of a population of cells, to the analysis of a single cell[10].

1.2 Traditional Blood Techniques

Blood is the fluid that circulates within vertebrates and is essential for the life of cells throughout an organism; it transports ion, gases and nutrients. It is a mixture of cells suspended in liquid called plasma. It also contains nutrients, hormones, clotting agents, transporting proteins such as albumin, and immune factors, such as immunoglobulins, as well as waste products to be filtered out by the kidneys. The cell component consists of three main classes, red blood cells, white blood cells and platelets, as shown in figure 1-1.

Red blood cells, or erythrocytes, whose primary function is to carry oxygen, make up to 45 percent of human blood volume. They are biconcave and discoidal (8 micron diameter by 2 micron thick), essentially similar to a doughnut shape with an indentation in the center replacing the hole. White blood cells, or leukocytes, are part of the immune system. There is approximately one white blood cell for every 1000 red blood cells in a healthy person, and they are roughly spherical and range from 5 to 20 microns in diameter[12]. There are three major types of white blood cells: granulocytes, lymphocytes and monocytes. Platelets, or thrombocytes, range in size of 1 to 3 micron in diameter.

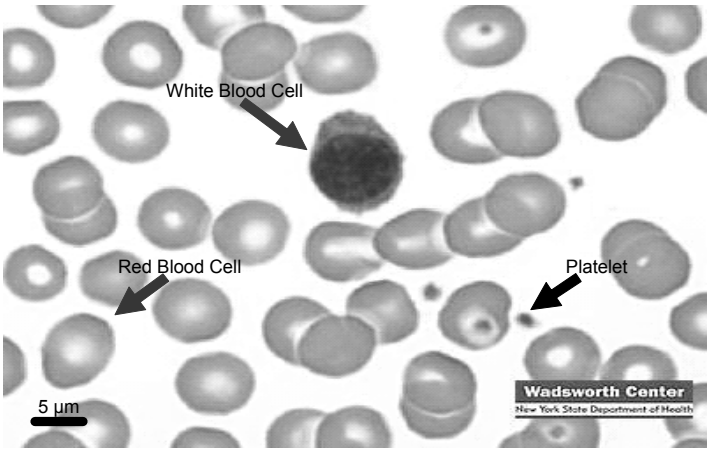

Figure 1-1: The three main cell components of blood are shown, white blood cells, red blood cells and platelets.[11]

They are responsible for helping the blood clot. There are on average 40 platelets for every white blood cell.[13, 14]

Blood, for transfusions, is frequently broken down into key components, such as red blood cells, platelets, and plasma since medical patients rarely require all of these components. Doctors can transfuse only the portion of blood needed by the patient's specific condition or disease, allowing the remaining components to be available to other patients. Once separated these components also have different storage times, from up to 10 years for frozen and treated red blood cells, to platelets which are stored at room temperature for only five days. Blood separation takes up to approximately one quarter of the time, cost and effort in hematological clinical diagnostics and prognostics[15]. [13, 14]

The most standard and widely used method to separate blood cell types is centrifugation and filtration. In centrifugation, the differences in density among the core cell types are utilized within a centrifuge that spins test tubes of cells. This requires large samples to be able to delineate regions, and a bulky machine to do the spinning. The red

blood cells, which are the densest, will settle to the bottom; the plasma will stay on top; and the white blood cells and platelets will remain suspended between the plasma and the red blood cells[16, 17]. This procedure can be greatly enhanced by the addition of a polysaccharide mixture, for increased resolution separation of individual cell types[18]. The cells can then be removed by various filtration methods.

In the late 70's advances were made to develop continuous flow cell sorting devices[19]. This lead to the development of a medical technology known as apheresis. This technique consists of a centrifuge and filter system in which the blood of a donor or patient is passed, and immediately returned in a continuous flow. A particular blood component is separated out, through the apparatus, and the remaining components are returned to circulation. This is particularly useful for platelets which have the shortest lifetime[13].

Presently, a major tool for the analysis of blood is the flow cytometer. Flow cytometry measures physical characteristics of single cells, as they flow in a fluid stream through a laser beam one cell at a time. The properties potentially measured from the scattered light include a particle's relative size, relative granularity or internal complexity, and relative fluorescence intensity. In the case of blood, antibodies specific to particular cells, which are conjugated to fluorescent dyes, are used. More advanced versions such as the FACSAria (BD Biosciences) flow cytometer are able to alter the destination of the cell based on this fluorescent data, and separate cell types. Additional work has been done to separate the blood components by various other physical properties, including electric charge[20] and magnetic field[21, 22, 23].

1.3 Separation Technology on a Chip

Attempts have been made to implement the traditional blood methods on a much smaller scale. Strong centrifugation is difficult to achieve at microscale dimensions, and the ones developed are cumbersome[24, 25]. Similar to flow cytometry, Fu *et al.*[7] designed a micro-fluorescence activated cell sorter, which propels specifically tagged cells at a T junction by an electric field. The micro Fluorescence Activated Cell Sorter (μFACS) may allow the huge and expensive conventional FACS machines to be replaced by a more sensitive disposable chip. Additionally, other novel separation methods are being developed. Both magnetic[26, 27] and electric forces[28] have been used to isolate, or separate types of blood cells, or to remove all cells from the native plasma[29]. These magnetic approaches use nanometer size beads, which bind to the target cell, similar to the fluorescent approach.

Microfabricated arrays have been used to separate cells based on deformability[30] and adhesiveness[31]. Ultrasound[32, 33] has also been used to create cell free plasma, as well as to separate blood components[34]. Becker[35] used a method which selects cells by balancing the dielectrophoretic and hydrodynamic forces; to separate human breast cancer cells from blood. Additional microfluidic methods have also included separation by leukocyte margination[36], and microchannel bends[37].

Diffusion-based devices, relying on the differences in size between cell components, have been used to separate cells. The device designed by the Austin group at Princeton known as the ratchet array[38, 39] uses a tilted array to separate based on differences in diffusion constants. These devices are however limited in velocity, because a given time is required for cells to diffuse to a new flow path. Thus the maximum speed is limited.

Some other size-based methods rely on filters[40, 41, 42], such as that of Mohamed *et al.*[43] who isolated rare blood components. The filtered component may be harvested by periodically stopping the flow into the filter and back-flushing to remove the desired particles from the filter mesh. Size-based filter methods have also been integrated with PCR amplification of genomic DNA from white blood cells[44]. In general, these processes are complex, involve fluorescent labeling, yield incomplete fractionation, clog easily, or introduce bias to the data.

As with other fields, miniaturization reduces consumption of materials, and leads directly to mass production. Many hope that microfluidic chips will one day revolutionize biotechnology in much the same way the semiconductor chips changed information technology. With the advancement of technology, perhaps one day we might be able to use a small handheld device to analyze blood samples, and detect diseases.

1.4 A Novel Deterministic Technique for Blood Separation

This thesis applies a novel microfluidic technique known as deterministic lateral displacement (DLD) for the separation of individual blood components. It was invented by Huang *et al.*[45] and is a microfluidic separation technique proving clear advantages over previous work. The first published use of the technique was to separate 0.9 from 1.0 micron polystyrene beads with 100% accuracy[45]. It was also used to demonstrate separation of large DNA molecules and blood cells[46, 47, 48]. Unlike filter-based methods[43], it can run continuously without clogging or stopping to be cleared. The technique is deterministic, which means particles follow a predetermined path through the device. Unlike diffusion based methods,[36] it does not depend on a random process to separate and

can in principle be run at very high speeds without degradation of performance. In fact, as will be shown later, the device performance increases with speed.

A number of different DLD design types are presented, all of which have the goal of separating blood components on the basis of size. Chapter 2 of this thesis will discuss exactly how a deterministic lateral displacement device works. Chapter 3 introduces different design options for more complex devices. Chapter 4 gives all of the experimental methods for both the fabrication of a device and design of a biological experiment. Chapter 5 presents the major fractionation results, separation of white blood cells, red blood cells and platelets within different designs. Chapter 6 discusses some of the complications when working with biological samples, namely the cells can be both non-rigid and non spherical. Chapter 7 will include an analysis of diffusion and other non idealities in device operation, followed by a conclusion in chapter 8.

2 Fundamental Fluidic Principles of Deterministic Lateral Displacement Devices

This chapter expands upon the concept of deterministic lateral displacement (DLD) as a method of cell separation. Subchapter 2.1 explains how the DLD device works, first with a broad discussion of the microfluidic device and how it is used. Subchapter 2.2 follows with by a more detailed section discussing the mechanics of the main functional region, summarizing the theory of Huang *et al.*[45]. After an introduction to fluid mechanics within the laminar regime in subchapter 2.3, subchapter 2.4 shows how to analytically determine the critical parameters of a DLD device. These theories were developed in collaboration with David Inglis[46,49]. The chapter finishes with subchapter 2.5 with some basic design paradigms for single DLD arrays, an original contribution.

2.1 The DLD Device

The DLD device uses an asymmetry between the average fluid flow direction and the axis of the array of microfluidic posts etched in silicon to separate micron size particles based on size. The array causes a lateral shift perpendicular to the average fluid flow for cells larger than a critical size. However, I would like to begin by discussing all of the other portions of the device which are necessary to take the blood from a single mixture to a number of different separated mixtures.

Figure 2-1 illustrates the key components of a device, namely an input region, an array region, and output region. The input region consists of a fluidic channel to deliver the sample to the array for separation. A uniform fluid flow in the array along side that of the input stream, is required for the DLD to function. Extra channels deliver this

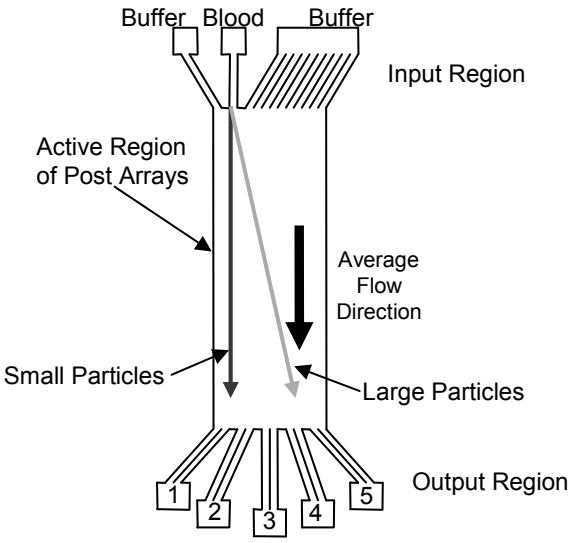

Figure 2-1: Picture of a typical DLD separation device with the three main regions marked along side a schematic. The separation is done in an array of posts at the center of the device. The top and bottom regions are input and output channels respectively.

additional liquid, called buffer, to carry the cells to be separated. This buffer is a mixture of salts designed to support the blood cells, as the cells are removed from the native blood solution. Within the array region, the fluid flows from the input to the output, small cells follow the fluid, and large cells move at an angle with respect to the fluid, as will be discussed in detail. The output region consists of a number of different channels, so that each of the different components that have been separated can be individually collected.

The device is placed into a plexiglass chuck as shown in figure 2-2, so that a constant pressure can be applied to all of the input or output wells. This constant pressure creates a flow between the input and output channels, through the functional array. The functional array will cause different amounts of lateral displacement as a function of cell size.

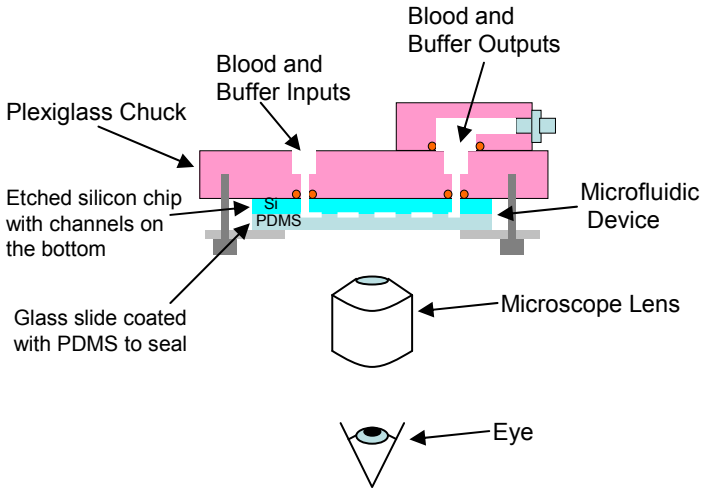

Figure 2-2: Picture of the microfluidic device within a plexiglass chuck. The Silicon and PDMS device is held into position with a metal plate with screws into the chuck. O-rings are used to create a fluidic seal between the chuck and the device. The chuck can then be connected to other tubing so buffer and blood can travel into and out of the device.

2.2 DLD Basics

The DLD device comprises a functional region consisting of an array of microposts or uniform columns constructed in a rigid material, such as silicon. This functional region is where the separation of particles takes place. The array is altered in such a way that the array axis differs from the flow direction. This can be accomplished by rotating a rectangular array, or by each row of posts being slightly offset laterally with respect to the previous row above it, as shown in figure 2-3. The following geometry is defined to describe the device. The posts all have an equal diameter (P), all the gaps perpendicular to the fluid flow have a width (G), and the spacing (center to center) between the posts is λ. The lateral shift between the adjacent post rows is called σ, and θ is the angle of

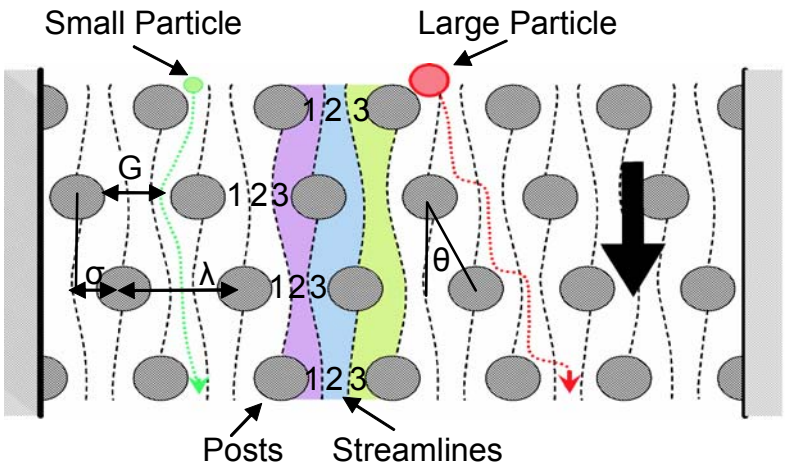

Figure 2-3: Schematic illustrating the separation by deterministic lateral displacement in an array of microposts, with an example row shift fraction of one third. This one-third shift fraction creates three equal flux streamlines. Dashed lines identify the boundaries between the streamlines, which are assigned an index, 1, 2, or 3, in the gaps between the posts. The green and red dotted lines depict the paths of particles both smaller and larger then the critical threshold, respectively. Small particles stay within a flow stream and large particles are displaced at each obstacle. G is the clear spacing between the gap, λ is the center to center post separation, and σ is the shift of the post centers in adjacent rows.

asymmetry of the array, as shown in figure 2-3. An additional parameter, the relative shift fraction (ε) or the relative change in position of the post compared to the previous row is

$$\varepsilon = \sigma / \lambda . \qquad \textbf{(2-1)}$$

Then ε and θ are related by

$$\varepsilon = \tan(\theta) ; \qquad \textbf{(2-2)}$$

this relative shift fraction ε is the key parameter in the design of a DLD device.

The basic principle is simple but subtle, and can be best understood by looking at the fluid divided into a number of streamlines. A streamline is defined as a region of flow in which, ignoring diffusion, the same group of molecules follow the same path throughout the array. For example, in figure 2-3 the fluid within a single gap is divided into three colored streams. The walls on each side of the array force the average fluid direction to be vertical. The asymmetry in the post array creates a bifurcation of the fluid flow leaving the gap of the previous row. In the example, the purple portion of the fluid leaving the gap flows to the left of the obstacle, while the blue and green flow to the right.

With a value of ε is 1/3, as shown in the example, the array is laterally shifted by one third of a row period from one row to the next, and one third of the fluid volume from the preceding gap bifurcates to the left at each row. Therefore the fluid can conceptually be divided into three streamline regions. As this process repeats, and one third of the original gap volume is bifurcated at each row, resulting in the streamlines returning to their original relative position within a single gap after 3 rows. This repeating cycle leads to fluid located in the original first position will move to positions 3, 2, and back to 1 in successive rows. In arrays with a different value of ε, the fluid would be conceptually divided into 1/ ε streamlines each of equal volume. Small particles, similar to the water molecules, will follow the streamlines cyclically through the gaps, moving in an average flow direction matching the fluid, thus they would travel straight through the array parallel to the sidewalls.

Consider a large particle flowing into a region adjacent to a post, as shown in figure 2-3. If its radius is larger than the width of the first streamline, it simply won't be able to

fit, and will be displaced laterally by the post into the second streamline. At the next row, the second streamline cycles into the first, and the particle is displaced again. This process repeats at each row, with the overall trajectory of the large particle not being in the direction of the fluid, but at the angle θ determined by the geometry of the array.

A single array separates particles based on a single size threshold, hereinafter the critical diameter D_C. All particles above that size are displaced and travel at the angle θ of the array, and all particles below that size travel at a direction equal to the average fluid flow. This critical diameter D_C is about twice the width of the first streamline adjacent to the post in the gap (labeled "1" in figure 2-3), and is proportional to both the gap size (G) and the shift fraction (ε).

These streamlines are defined to be of equal volumetric flow rate, but not necessarily equal width. In fact, because a pressure-driven flow creates a parabolic velocity profile across a gap (as derived in section 2.2.2), the flow next the post is moving much slower than the flow in the middle of the gap. The first width of the first streamline can be a factor of two or more larger than the width expected if this effect is removed. This width of this first streamline is a key parameter in determining the critical diameter in an array, and will be derived in section 2.4. First, we must take a step back, and look at some of the governing fluid mechanics behind the functionality of this device.

2.3 Introduction to Fluid Mechanics

Fluid mechanics is the analysis of action of forces on matter, specifically fluids like liquids and gasses. It is based on the assumption, that at the scale of interest, the fluid is a continuum. The following section will introduce the basic equations, and a

dimensionless number, and discuss what their significance, and application to the novel DLD devices. Any basic textbook in the area will have a derivation of these equations[50].

2.3.1 Navier-Stokes and the Reynolds Number

The underlining equation for fluidic mechanics is the Navier-Stokes equation. It is derived from the basic assumptions of conservation of mass, momentum and energy. It states

$$\rho\frac{\partial\vec{v}}{\partial t}+\rho(\vec{v}\bullet\nabla)\vec{v}=-\nabla p+\mu\nabla^2\vec{v} \qquad \textbf{(2-3)}$$

where ρ is the density of the fluid, v is the velocity vector, p is the pressure and μ is viscosity. This equation can be used to describe a large number of phenomena for both liquid and gas flow; however it is complex enough that only a few simple applications can be directly solved. Therefore additional assumptions are often made to solve the equation for more complex situations. A number of dimensionless numbers are used in fluid mechanics to evaluate these approximations. The most important of these dimensionless numbers is called the Reynolds number.

The Reynolds number (Re) is the ratio between the inertial forces and the viscous forces, and thus quantifies the relative importance of these two forces on the flow.

$$\mathrm{Re}=\frac{\rho vL}{\mu} \qquad \textbf{(2-4)}$$

where v is the local speed of the fluid (here up to 5 mm/sec) and L is a characteristic length (here approximately 10 micron) and ρ and μ are the values for water (10^3 kg/m^3 and 10^{-3} Pa·sec). If Re < 1, the viscous damping quickly removes kinetic energy

(translational and rotational) from a fluid element; therefore, the inertial forces can be ignored, and removed from the equation. This results in Stokes' equation

$$\rho \frac{\partial \vec{v}}{\partial t} = -\nabla p + \mu \nabla^2 \vec{v} . \qquad \textbf{(2-5)}$$

This simple linear equation describes laminar flow, where the fluid experiences no turbulence and the velocity fields are the direct result of pressure gradients. Under these conditions the flow profile is very easy to qualitatively predict such as shown in section 2.2. Given the identified characteristic numbers, Re = 0.05; therefore, velocities as high as 100 mm/sec are possible within my geometries, without having to worry about deviations from the Stokes' approximation.

2.3.2 Velocity Profiles in Simple Geometries

The velocity profile across a single gap is integral to calculating the streamline width. As a first order estimation, the gap can be approximated as a single infinitely long channel of width G. Because all devices discussed here a ratio of depth E to gap size G (aspect ratio) of at least 5 (typical values for E and G being 50 micron and 10 micron respectively), the depth dimension can be ignored, resulting in a two dimensional calculation. The channel is infinite in the y direction, and of width G in the x direction. For the steady state solution, the left term of equation 2-5 is set to zero. Because there are no variations along the channel, the pressure will drop uniformly along the length of the channel. Therefore the pressure p is simply a linear function of y and will be defined as

$$p = -ky \qquad \textbf{(2-6)}$$

where k is a constant. The velocity vector has a number of boundary conditions. Because of the symmetry of the problem, the velocity must only be in the y direction. Because of friction between the channel walls and the fluid, the velocity of the fluid goes to zero, that is the fluid cannot move or slip directly next to a stationary wall. This is called the "no slip" condition, and is used in many calculations.

Using these boundary conditions in equation 2-5 provides two equations for the two components of velocity

$$v_x = 0 \qquad \textbf{(2-7)}$$

and

$$-k = \mu \frac{d^2 v_y}{dx^2}, \qquad \textbf{(2-8)}$$

which has the solution

$$v_y = \frac{k}{2\mu}\left(Gx - x^2\right). \qquad \textbf{(2-9)}$$

This is a parabolic curve across the width of the gap, with a maximum at the center, and dropping to zero at both boundaries. Solving equation 2-9 for the maximum velocity which occurs at the middle of the channel (v_{max}) gives

$$v_{\max} = \frac{kG^2}{8\mu}. \qquad \textbf{(2-10)}$$

Alternately, we can write equation 2-9 as

$$\vec{v}_y = 4v_{\max}\left(\frac{x}{G} - \frac{x^2}{G^2}\right) \qquad \textbf{(2-11)}$$

which references the maximum velocity, v_{max}, and will be useful in the derivations to follow.

To test the validity of this parabolic model, a finite element analysis of a section of posts is constructed. An introduction and more detailed information about finite element analysis are located in section 2.5. Figure 2-4 shows the solution to this parabolic equation compared to a finite element analysis of the velocity in a channel constructed using Femlab (Comsol Inc. Burlington, MA). The Femlab simulation shows this simple parabolic approximation is a reasonable estimation for the velocity profile between two walls. This will model the fluid flow between the two posts in each gap within the DLD device.

This model has also been qualitatively confirmed by optically observing individual

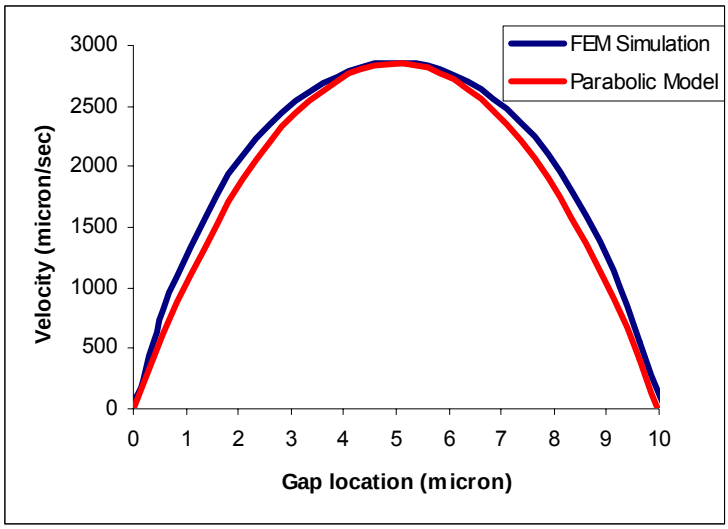

Figure 2-4: The simple two dimensional model of a fluidic channel compared to a finite element analysis of a gap within a DLD array of width 10 micron. The linear pressure drop will create a parabolic velocity distribution, as shown.

particles within the device. The individually tracked cells are observed to speed up and slow down as their relative location within the gap changes. That is, while a particle is passing through a gap toward the center, it will travel more quickly then when passing through a gap toward the edges.

2.3.3 Fluidic Resistance of a Simple Geometry

One term which will be used in describing and designing DLD devices is the fluidic resistance (R), where R is defined as

$$R = \Delta P / Q \qquad \textbf{(2-12)}$$

where ΔP is the change in pressure (in Pa) and Q is the volumetric fluid flux (in m^3/sec). The position velocity relationship found in equations 2-10, can be used to develop the fluidic resistance of a non-infinite channel, of length L, width G and depth E, where E >> G (In boundaries of the aspect ratio E/G in these devices of 5 or greater, the three dimensional parabolic profile is dominated by the terms from the small dimension G.) The pressure relationship is from equation 2-6, and volumetric flux is the average fluid velocity times the width and depth of the channel, therefore

$$R = kL / V_{avg} GE \cdot \qquad \textbf{(2-13)}$$

Substituting equation 2-10 into equation 2-13, where for a parabola

$$v_{\max} = 3/2\, v_{avg}, \qquad \textbf{(2-14)}$$

gives

$$R = 12\mu L / G^3 E \cdot \qquad \textbf{(2-15)}$$

This equation, along with others for some more complex geometries are found in Kovacs[51], and derived in Foster and Parker[52]. The pressure drop can now be estimated for a single gap in the geometry, by calculating the fluidic resistance and using an average velocity. With a gap and length of 10 micron, and a depth of 50 micron, the fluidic resistance of a single gap on the order of 2.4×10^{12} N sec/m^5, and the pressure drop from a single gap is about 2.4 Pa when the average velocity is 2 mm/sec. This equation will be particularly useful in the design of cascade devices discussed in section 3.1.3.

2.3.4 Shear Stress on Particles within a Simple Geometry

As the particles to be sorted travel through the gap they will experience different pressures and stresses. As the flow travels between posts, it will speed up because of the narrowing in area for the fluid to travel. Because of this narrowing of the flow between the posts, particles in between the gaps will experience the largest stress. These effects are particularly important in the analysis of biological samples, which are sensitive to changes to stress and pressure.

The shear stress across a cell can be examined with a simple model to see if it has a major effect within the device. The variation in velocity profile across the width of the gap causes a shear stress across the lateral direction of the cell. Shear forces play an important role in the immune system, and are known to activate platelets[53]. According to Newton,

$$\tau = \mu\gamma \qquad \textbf{(2-16)}$$

where τ is the shear stress and γ is the shear rate. For the simple geometry with a velocity gradient only in a single direction,

$$\gamma = \frac{dV_Y}{dx} \qquad \textbf{(2-17)}$$

which is measured in 1/s. For the velocity profile in equation 2-11, the shear rate is maximum at the wall, and has the value

$$\gamma = \frac{4v_{\max}}{G}. \qquad \textbf{(2-18)}$$

This results in a value of shear stress of 0.8 Pa for a speed of 2 mm/sec and a 10 micron gap. According to literature[53, 54], this is on the order of the shear stress experienced in some of the larger arteries (0.3 Pa), but well below the higher values stressed in the capillaries (10 Pa). Therefore shear stress is not expected to have a negative effect on the cell.

2.4 Derivation of the Critical Diameter in DLD Array

With a better understanding of the basics of fluid mechanics, this section returns to a development of the governing equations of the DLD. As discussed previously, the critical hydrodynamic diameter is approximately equal to twice the width of the first streamline, assuming the particle itself doesn't alter the streamlines. Therefore,

$$D_C = 2\zeta G\varepsilon \qquad \textbf{(2-19)}$$

where ζ is a variable parameter which is a function of ε and post geometry that accommodates the velocity distribution between the posts. By making the simplification of square posts, (orientated with sides parallel to the side walls of the device), we can approximate the velocity distribution between the posts, as the parabolic solution found in equation 2-11 (which assumes the length of the channel between the posts is infinitely

long). The effects of this simplification are further discussed in subchapter 7.1. At each post, a fraction of the fluid (equal to the shift fraction ε) is bifurcated. By calculating a shift in the total flux necessary for this same bifurcation, one can calculate the width of that first streamline. Therefore the ratio of the flux within the first streamline to the total flux is equal to the shift fraction, or

$$\int_0^{\zeta G} v_y dx = \varepsilon \int_0^{G} v_y dx . \qquad \textbf{(2-20)}$$

Substituting equation 2-11 in 2-20 results in a cubic equation for ζ,

$$-2\zeta^3 + 3\zeta^2 = \varepsilon , \qquad \textbf{(2-21)}$$

which can be numerically solved, for ε = 0 to 0.5, and is displayed in figure 2-5. For example, a device which has an ε = 0.1, gives only one real solution to equation 2-21 of ζ = 1.96. Thus the critical diameter is 3.92 Gε, about twice as wide as the expected values of 2 Gε for even width stream lines.

To compare this theory with a measured critical diameter, data was collected over about 20 different devices over a range of G from 1.3 micron to 38 micron and ε from 0.005 to 0.5, including the devices presented here. Polystyrene beads varying in size from 0.9 micron to 22 micron, with many of experiments with beads in the range of 5 and 10 micron (the size range useful for blood cells). The data was normalized by dividing the particle size by the gap width, and is presented in figure 2-5.

The threshold criterion for a particle within a region consisted of lateral movement of at least half of the designed displacement. For each combination of ε and G, an open circle was placed on the graph if a particle or cell was observed to laterally displace greater then half the designed distance. However if the particle did not displace enough

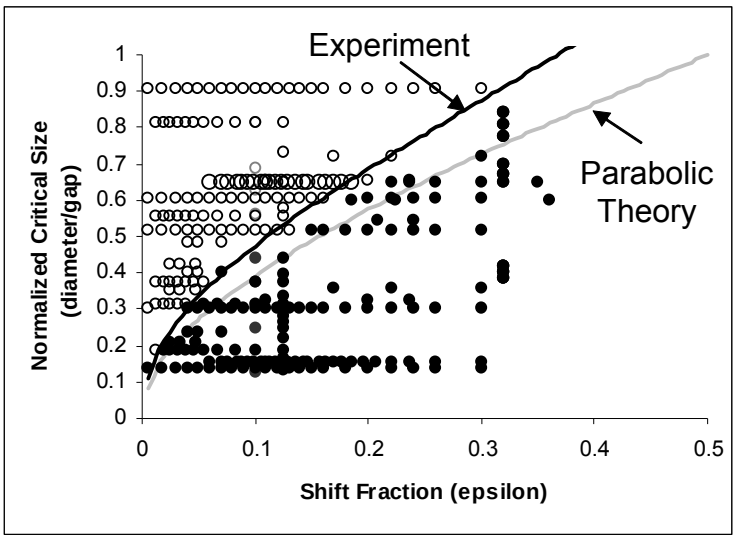

Figure 2-5: A collection of data marking the displacing and straight particles as a function of shift fraction and normalized critical size. Displaced particles are marked with an open circle and straight particles are filled. The gray line is the solution to the cubic equation developed from a parabolic profile. The black line is a power law fit to the data used for the design of devices in this thesis, with terms A=1.4 and B=0.48. For example, a shift fraction of .1 yields a critical diameter of 0.46 times the gap size. [55]

when traveling through the region, the data point was marked with a solid circle. The large majority of particles were observed to either displace fully or not at all, showing the clear bifurcating separation of particles.

This data is compared with a parabolic model, as shown in the figure the parabolic relationship underestimates the critical size. This parabolic relationship assumes perfectly vertical flow between the square posts, and infinite length of post. However, the constructed devices have short, rounded posts, and therefore the flow patterns will be significantly more complex, as the fluid travels around the posts.

The data from the experiments shown in figure 2-5, was used to find a best fit model for the critical threshold. It was found that

$$D_C = 1.4G\varepsilon^{0.48} \quad \textbf{(2-22)}$$

was the best at matching the data. Therefore equation 2-22 was used to design all the thresholds discussed herein.

In general, a smaller epsilon results in an array with a smaller critical size for a given gap. However, the smaller epsilon has a smaller separation angle, and therefore requires a longer device for separation. Assuming an input stream width of 5λ (where λ is the center to center post separation), ignoring diffusion, and a critical diameter of half the gap (ε = 0.1); it takes about 100 rows to separate particles, while for a critical diameter of one fifth the gap (ε = 0.02), it takes 500 rows. For a value of λ = 20 micron, the two sections would need to be about 2 mm and 1 cm long, respectively.

Additionally, at smaller epsilon, the streamlines are narrower, and the particles are more sensitive to thermal motion (diffusion discussed in chapter 7). These two criteria contribute an experimental rule of thumb of a lower limit on epsilon of 0.02, which gives a size critical diameter of about one fifth the gap size[49]. For the devices herein, epsilon was limited 0.04, which gives a critical diameter of three to four times smaller then the gap. An upper limit should also be set at a reasonable level below G of 0.4 epsilon, which corresponds to a critical diameter of 3/4G.

2.5 Array Physics and Design

Using the theory and design for a single gap, this section evaluates a slightly bigger picture and analyzes some of the relationships of a uniform large array of posts. Particularly, an equation for the pressure – velocity (ie fluidic resistance) similar to equation 2-15 for a channel but in this case for a complete uniform array, will be

developed. Because of the higher-order effects of round posts; and much more complex velocity profiles, an analytical solution will not be possible, and a finite element analysis will be used.

Finite element analysis is a numerical method in which the geometry of interest is divided into a large but finite number of discrete regions in a grid. The governing equations, in this case Navier-Stokes, can then be solved numerically across all of the elements. The accuracy of the answer can simply be improved by increasing the number of elements. The commercial computer software package called Femlab (Comsol Inc. Burlington, MA) performs this computation. It was used to simulate the array in two dimensions, maintaining the assumption that the depth of the device is much greater then the gaps, so the profile is dominated by the two dimensions. An example of an array and a velocity profile are shown in figure 2-6.

Running a number of simulations, in which width, depth and gap size were varied led to the development of the following relationship for the fluidic resistance of an array,

$$R \approx 4.6\left(\mu\beta / \alpha G^2 E\right), \qquad \textbf{(2-23)}$$

where α is the total width of the array region, β is the total length of the array region, E is the depth of the device and μ is the viscosity of the fluid. This was developed for a value of epsilon of 0.1, and the post size equal to the gap size. As can be expected, the resistance is proportional to the ratio between the length and width of the array (β/α). However the resistance of a complete array is inversely proportional to the square of the gap size (not the gap size cubed). This is because as the gap size is decreased for a given width array, (while the average fluid velocity goes as the inverse of G) the total number of gaps increases giving the fluid parallel paths which divide the resistance. That the

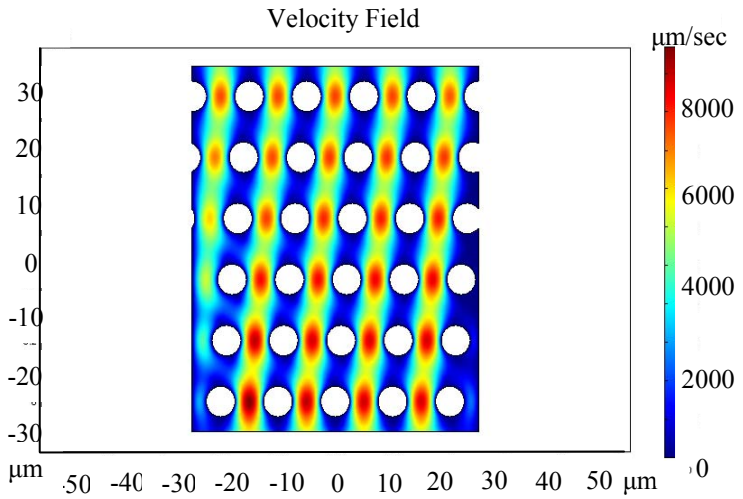

Figure 2-6: An example of the velocity field solved with a finite element analysis model. The array consists of 10 micron posts and 10 micron gaps, with a shift fraction of $\varepsilon = 0.1$ (a shift of 2 micron for each row). A difference in pressure is applied across the top to the bottom of the array, and the velocity at each element is measured. The velocity profile shows the posts create regions of slow (blue) and fast (red) fluid movement. The highest velocity is centered between the gaps, and a parabolic velocity profile across the gap is confirmed.

dependence of the resistance goes as the inverse of the square of the gap size for the array is still important, and will be something to consider as devices of smaller size are developed because of the required pressures.

The resistance calculated is used to estimate the average velocity for a given applied pressure. For example, the chirped device in section 3.2.2 consists of a total array size of 4000 micron by 4.6 cm. The gaps are 10 micron and it is etched to a depth of 50 micron. Using equation 2-23 gives a fluidic resistance of 1.1×10^{13} Pa s/m^3. A typical average flow velocity is 1500 micron/sec, this is the average flow velocity across the gap between the posts and corresponds to a volumetric fluid flux (Q) of 3.0×10^{-10} m^3/s. Using

equation 2-12 gives an applied pressure for the array of 3.2 kPa or about 0.5 psi. In addition, in section 3.1.3 a device known as the cascade array will require channels next to the functional region to have equal fluidic resistance to the array. These calculations will be crucial to the functionality of that device.

3 Design Options for Complex DLD Devices

The previous chapter focused on the physics and understanding of a single functional array. Now this chapter expands on theory to explain how to design complex multi-threshold devices. Beginning with device functionality, subchapter 3.1 discusses options available to tailor the design to a particular application. Subchapter 3.2 will characterize the various methods developed for using the DLD technique to separate wider ranges of particle sizes than possible with a single array.

3.1 Separation Modes and Device Functionality

The first step in design is the layout of the input and output channels, for which a typical example is shown in figure 3-1. The design must consist of a set of channels which create and maintain the vertical flow and hence the separation mechanism. Each of these channels must be designed to have equal fluidic resistance. The channels connect to pads 1.5 mm in size consisting of dispersed posts for support of the ceiling lid. These inlet and outlet pads are also used for alignment of the connection holes. The input region consists of a number of channels or fluid injectors across the top of the functional array. One of these channels is connected to the sample cell well, while the others are simply connected to buffer reservoirs. It has been found that either a centrally located input throat or one located next to the wall of a device function can be used. Positioning the throat closer to one side of the device increases the amount of useful array area (since the particles are only laterally displaced in a single direction). However, if the device throat is directly next to the wall, care must be taken in the layout of the mask along the wall so that no gaps are smaller than G to prevent cells from getting stuck.

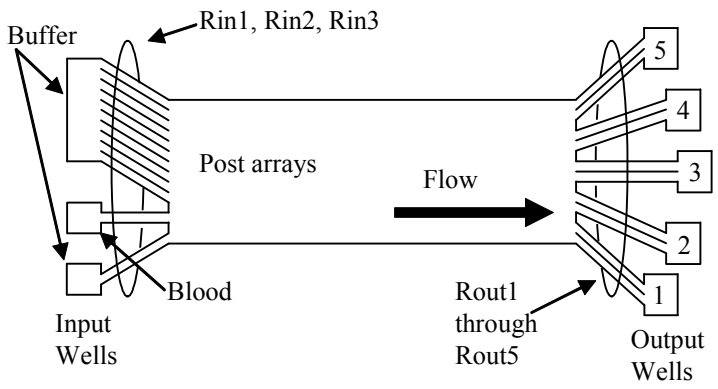

Figure 3-1: Schematic of the input and output regions of a typical DLD blood separation device. The device consists of pads for where holes can be placed for loading and unloading of the sample. Between these pads and the post arrays are channels of equal fluidic resistance. This resistance creates the uniform flow necessary within the array.

The output of the device can be divided to flow into a number of wells depending on the number of separate subgroups desired. When the output groups are not needed, all of the fractionation can be returned to a single well, such as when all data has already been obtained by visually inspecting the location of the cells within the device.

3.1.1 Input and Output Channel Design

As shown in figure 3-1 the input and output regions of the device consist of a number of a channels of varying length. A set of smaller channels are used, rather than an open section of flow, to support the PDMS roof of the device. Equation 2-15 was used to compute the width and length of each of channel to have the same fluidic resistance, thus maintaining the parallel flow entering and exiting the device. Table 3-1 shows the width

Resistance In:	Ch. Width (micron)	Ch. Length (mm)
R1	112	10.8
R2	50	9
R3	112	10.8
Fluidic Resistance of each channel: 4.3 X 10^7 N sec/m^5		
Resistance Out:	Ch. Width (micron)	Ch. Length (mm)
R1	57	11.3
R2	75	15
R3	80	16
R4	75	15
R5	57	11.3
Fluidic Resistance of each region: 3.55 X 10^8 N sec/m^5		

Table 3-1: The design parameters for a set of balanced channels for the input and output regions of a device.

and length of input and output channels for a typical DLD device like the one shown in figure 3-1.

3.1.2 Separation Modes

The input stream width entering a DLD device directly affects the types of applications for that device. These types of devices are summarized in table 3-2. Two different functional modes are defined herein. The first, designed for high throughput, is called the preparative device (PD). The device consists of a wide throat width (on the order of one half of the width of the active area), so larger volumes may be prepared, and high volume flow rates for the input blood are possible. The preparative device is ideal for separating a larger sample for use in other applications, such as a plasma transfusion. Such a device is demonstrated in collaboration with D. Inglis to remove all of cells from whole blood to leave residual plasma[46, 55].

Example Name	Operation Mode	Injector Width	Design Principle
Fractionation (FD)	Analytical	Narrow: on order of G	chirped ε, fixed G
Preparative Separation (PD)	Preparative	Wide: on order of half of the array width	Cascaded regions of different G

Table 3-2: Operation modes of a prototypical separation device.

The second design type is an analytical design called a fractionating device (FD). The device consists of a narrow throat width (on the order of 3 to 5 times the largest particle). It fractionates an input stream into multiple outputs based on size, and can analyze extremely small sample volumes. It has a number of applications including analyzing the small changes in the size of white blood cells. All of the experimental results discussed here are from fractionating devices.

3.1.3 Limitations of Single Arrays

Second, after the input-output portion of the device design, attention should be directed to the post region where separation will take place. A single functional array has only one threshold, or separation criteria, creating two deterministic directions for particles. This single array has only one single separation criteria. All particles above the threshold are separated from all particles below. Additionally, the single uniform array will have an upper size limit equal to the gap size. Particles larger than the gap size will get stuck, and clog the device. Accordingly, applications of this device are limited.

Through experimentation, three other types of devices have been designed which go beyond the basic single array discussed in chapter 2; these designs are pictured in figure 3.2. The multiple array device shown in figure 3.2A is simply two or more single arrays placed one after the other. In each subsequent array, only the gap is varied so regions

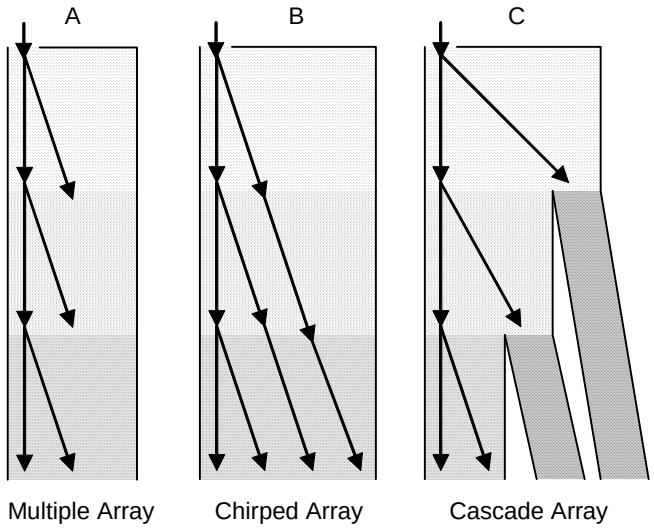

Figure 3-2: The basic design layout for each of the types of devices used in this thesis. In the multiple design (A), the arrays have different gap sizes, for different separation criteria. Note for this design, the particles of one array can get stuck at the entrance to the next array. The chirped design (B), achieves a separation from varying the shift fraction, which solves the clogging problem. The cascade design (C) increases the size range of particles separated by adding channels.

with a smaller gap will separate smaller particles[45]. However, in our first such argument, no care was taken to avoid clogging within this device due to the decreasing G, and so particles of interest separated in the first array could become trapped at the entrance to smaller arrays. Nevertheless the principle is shown and data collected to create the theories in chapter 2.

The chirped device in figure 3.2B is a set of successive arrays which are designed (as described in section 3.2.2) to separate smaller particles in the next array without clogging due to the larger particles. Therefore, the gap is fixed throughout the device, and the shift fraction (ε) is varied to change the critical threshold, allowing for a continuous flow

device. Finally, the cascade design shown in figure 3.2C uses additional microfluidic channels to increase the types of separations which are possible.

3.1.4 Dynamic Range

As discussed herein, the four types of separation arrays are mentioned for size criteria of both separation and clogging. Therefore it is important to define a mathematical term to describe the range of sizes at which each device will work.

The range over which a device is functional is an important evaluation of separation technologies. Generally, dynamic range refers to the ratio between the largest and smallest values of a variable quantity; here the dynamic range is used to refer to the ratio of the largest critical diameter which can be separated without clogging to smallest critical diameter within the device. Table 3-3 gives the dynamic range as well as some additional parameters for each design type.

For our single array device, there is only one critical diameter. The largest separation criterion equals the smallest so the DR is 1. The multiple array device clogs easily because only the gaps of the device are altered; therefore, the DR is not useful for continuous operation. As stated in section 2.4.1, the limits of a practical critical diameter are G/5 and 3G/4 (results from epsilon = 0.02 and epsilon = 0.4). Therefore the chirped array, with a single gap and varied shift fraction, using these criteria will have a DR of ~3.75. The cascade device, with the additional features of more microfluidic channels, is designed to go beyond these limits and can have a DR of 20 or more. Further explanation for each device is given in the next section.

Design Name	Design Principle	Mode	Non-clogging Dynamic Range
Single Array	fixed ε fixed G	Binary	1
Multiple Array	fixed ε varied G	Stepped	-
Chirped Array	chirped ε fixed G	Stepped	~ 3 to 5
Cascade Array	multiple G, chirped ε	Multiple Regions with removal of larger particles	~ 20 or more

Table 3-3: The basic principles used in the design of the four different DLD arrays.

3.2 Separation Array Types

Beyond the single array, more refined designs have included the multiple array, the chirped array and the cascade array, all of which were shown in figure 3.2. These designs improve upon the basic single array design in order to increase the size of particles to be separated as well as different applications. The following sections will review the criteria that can be changed in consecutive arrays, and discuss what is necessary to maintain a continuous flow functioning device.

3.2.1 Multiple Array Design

As shown in equation 2.19, the critical diameter D_C is a function of the gap size. In this design, arrays with differing gap sizes were each placed consecutively. The change in gap size varies the critical threshold, creating various output streams. Each additional array results in an additional output stream consisting of a new range of sizes.

An example of a multiple array design criterion is shown in table 3.4 with an example of experimental particle paths in figure 3-3. The device comprises three sections, each with a fixed epsilon of 0.1 (an angle of 5.7°), and varied gaps of 5, 10 and 20 micron.

Critical Size	Epsilon	Angle	Length	Displacement
micron		degrees	mm	micron
2.5	0.1	5.7	5.3	530
5.0	0.1	5.7	5.3	530
10.0	0.1	5.7	5.3	530

Table 3-4: The design criteria of the multiple array design. Three regions consist of different gap sizes, 5, 10 and 20 micron respectively.

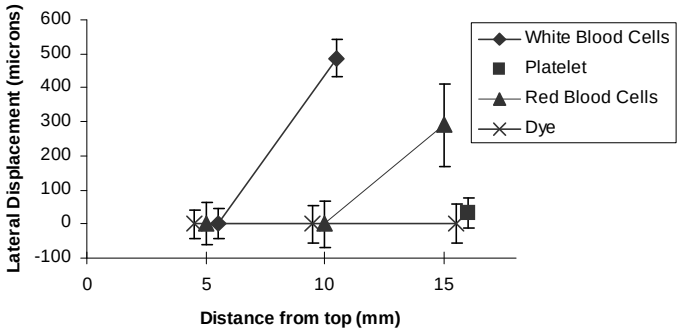

Figure 3-3: An experimental position versus displacement graph for the bottom two sections of the multiple array device, showing the paths of white blood cells, red blood cells, platelets and a background dye. Note, the white blood cells get stuck at the end of the second region (10mm).

The dye and the platelets (PLT) are both smaller than the smallest critical diameter, so they travel straight through the device. The red blood cells (RBC) are smaller then the critical size for both the first and second region but larger than the critical size of the final region, and are laterally displaced there. The white blood cells (WBC) are the largest, and therefore separate in the second region. Since the second region causes the white

blood cells to displace and separate while the third region causes the red blood cells to laterally displace and separate at the end of the device, red blood cells, white blood cells and platelets are observed in different locations of the device.

In this early design, care was not taken in maintaining a non-clogging continuous flow through the entire device. So it is important to note the DR can not be measured as particles separated in the first array are going to become trapped in the second.

In this device, the separation angle is fixed for each region, so each array is the same size with the same amount. This design has another disadvantage; because of the variations in gap size, the critical size is sensitive to the accuracy of the etching step. An over or under etch can cause a non-linear shift across the critical thresholds of each region. This makes the fabrication of smaller devices with only the gap altered more difficult. Nevertheless, this device demonstrated the fundamental feasibility of separating blood cell types. Further details are given in subchapter 5.1.

3.2.2 Chirped Array Design

Equation 2.19 which gives the critical particle diameter, has not only a gap dependence but also a shift fraction (ε) dependence. In this design, the threshold of each region is varied slightly in critical diameter, so a chirped (a term borrowed from varying over a range of frequencies) output of sizes is created. Unlike the multiple array, epsilon is varied (with only one or two gap values used throughout the device).

Because the critical diameter is a nonlinear function of shift fraction, a device based on changes in shift fraction is more computationally complex in design preparation. Additionally, since each separation angle is different, the length of each region must be calculated for a uniform distance for displacing particles in each region of the device.

This type of device is linearly sensitive to etching since the change would be uniform to all gaps within the device. All of the chirped arrays discussed herein consist of only one or two gap sizes in which epsilon is varied.

Examples of a chirped design criterion are shown in table 3.5 with an example of the input-output curve in figure 3-4. The device consists of 13 sections, each with a fixed gap of 10 micron and a varied epsilon from 0.04 to 0.4. The device was designed so each array varies in threshold from 3 to 9 micron at 0.5 micron intervals, which is a DR of 3. Thus, particles larger than 9 micron diameter are bumped in all regions, while those below 3 micron flow straight through the device. Particles between 3 and 9 micron begin

		Version A				Version B		
	Critical Size	Gap	Epsilon	Angle	Length	Gap	Epsilon	Angle
	Micron	micron		Degrees	micron	micron		Degrees
1	3	10	.004	2.31	9834*	10	.004	2.31
2	3.5	10	.056	3.19	1496	10	.056	3.19
3	4	10	.073	4.21	1122	10	.073	4.21
4	4.5	10	.094	5.38	880	10	.094	5.38
5	5	10	.117	6.71	704	10	.117	6.71
6	5.5	10	.143	8.18	572	10	.143	8.18
7	6	10	.171	9.8	484	10	.171	9.8
8	6.5	10	.202	11.6	418	10	.202	11.6
9	7	10	.236	13.5	352	10	.236	13.5
10	7.5	10	.272	15.6	308	12	.186	10.7
11	8	10	.311	17.9	264	12	.213	12.2
12	8.5	10	.354	20.3	242	12	.242	13.9
13	9	10	.398	22.8	198	12	.272	15.6

Table 3-5: The two designs of a chirped device used in this thesis. Shift fraction and separation angle is calculated for each desired critical size. Then the length of each section is calculated to maintain an equal lateral displacement in each region (in the version A case, 83 micron). Note the first region marked with a star, has a displacement of three times the other regions, to help the separation of white cells from the main blood stream.

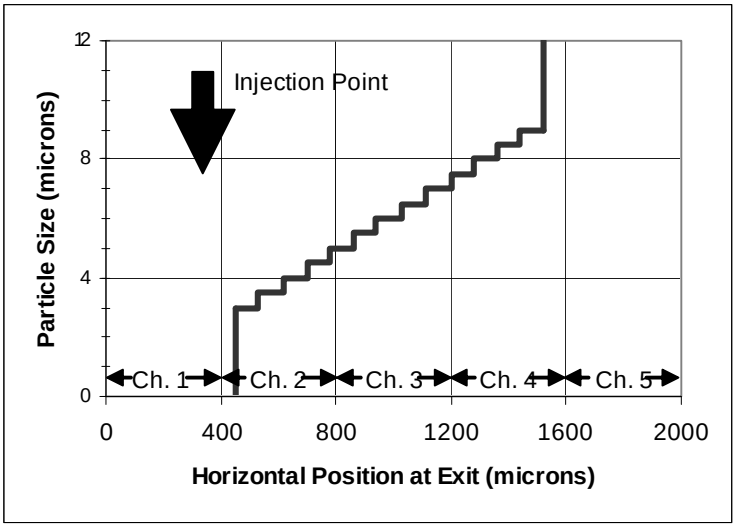

Figure 3-4: The input output function of chirped device: The function shows the designed output location for the range of particle sizes within this device. The output is further subdivided into 5 exit channels which can be collected and analyzed. The injection point is marked which lead to red blood cells in the main stream being located in both the first and second channel.

by displacing in the upper sections of the device, which have the smaller D_C. Once these particles enter a region in which they are below the D_C, they switch and begin flowing straight. This chirped design has the advantage that because G is fixed (or is only slightly varied throughout the array), particles which match the largest critical diameter in the array will not clog the region with the smallest critical size. This is the practical limit of the dynamic range. Further experiments with blood are in subchapter 5.2.

3.2.3 Cascade Design

Some applications, such as blood, use very heterogeneous liquids with varying particle size differing by more than a factor of 10, which is beyond the upper limit in dynamic range of the previous designs. More design variations are needed to expand the

range, and create a non-clogging device with a higher DR; these variations will be referred to as the cascade design.

In order to further increase this dynamic range, consecutive regions (chirped or single) can be cascaded successively, each with a slightly smaller critical size. However, these devices need additional output channels beyond the chirped array design. After the larger particles have been separated in one section, they need to be removed from the active region of the device, as not to clog the next section. Two different methods for this removal, shown in figure 3-5, have been developed. Both methods include channels (closed) or obstacles (open) that are larger than the next array, but vary in positioning.

The right most design depicted is the open array, because the larger obstacle region is

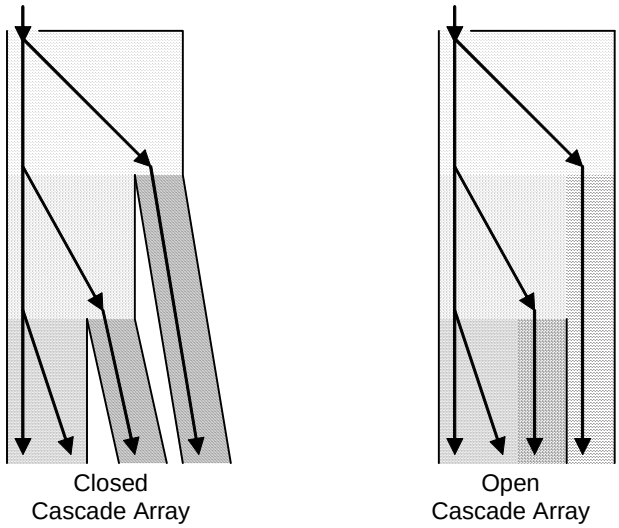

Figure 3-5: Topographical representation of closed and open cascade design implementations. The closed version includes vertical exits after each region, with the fluidic resistance balanced by lengthened channels. The open version comprises an open wall to the side of the next section of the array, consisting of a serpentine pattern of larger obstacles with a balanced fluidic resistance.

always fluidically accessible to the smaller post array. Particles can enter the obstacle region at any row. An example of this type of design is the Plasma Separation Design constructed by Inglis [46, 55].

The left most design is called the closed design. The particle removal is done by a set of exit channels at the end each region to remove streams of larger particles. The closed design connects to the array only at a single vertical point, and has a closed side wall between the channels and the array. The closed cascade device was selected for further experimentation as discussed in subchapter 5.3 herein.

An exemplary closed cascade array, shown in table 3-6, provides an input-output curve, shown in figure 3-6. This array includes three cascaded regions, with three vertical exit locations, one for each functional region. The first two cascade regions consist of single threshold array, while the third region comprises two threshold arrays. The largest particles are separated in the first region and as to not clog the second region, are transported out of the device by the exit channels. This process is repeated at the end of the second region. These additions allow the cascade design to have dynamic ranges of 20 or more.

Section	Critical Size	Gap	Epsilon	Angle	Length	Displacement
		micron		degrees	Mm	Micron
1	7.00	16	.089	5.08	25.5	2500
2	3.33	8	.080	4.59	21.9	1750
3	1.5	4	.064	3.68	7.8	500
	0.67	2	.050	2.88	9.9	500

Table 3-6: Exemplary array values for a closed cascade array with four functional sections. The device employs 16 micron wide side channel after the first region and 8 micron wide side channels after the second region, preventing larger cells from clogging the smaller regions.

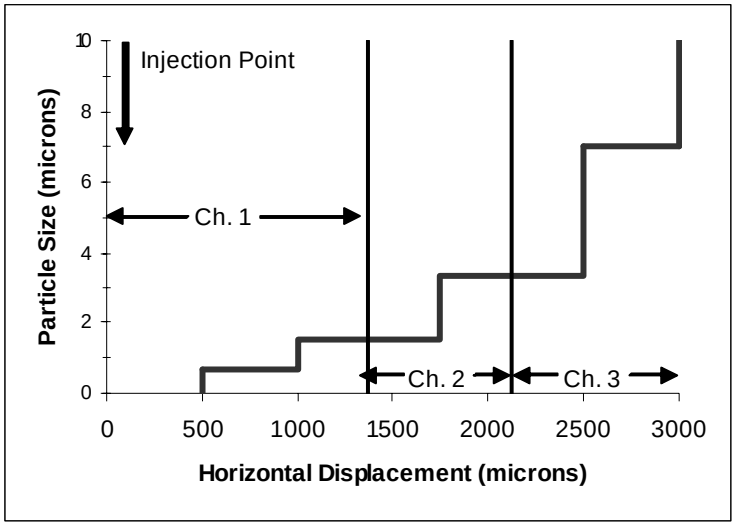

Figure 3-6: The input output relationship within the cascade device. The three channels mark the location of each of the functional regions and subsequent exit regions.

All cascade devices need important fluidic engineering to maintain the expected vertical flow through the device. At each successive functional region, fluidic resistance increases as a result of the smaller gaps. The exit or obstacle portion of the design must be built with comparable resistance to ensure vertical flow. The effective shift fraction (ε) will change unless the fluid flow at the end of each section near the parallel exit channel is maintained. A change in ε will result in change in the overall displacement as shown in the example simulation in figure 3.7. It will also change the critical threshold. The closed cascade device has added fluidic resistance obtained by long exit side channels with higher resistance to maintain the fluidic balance and vertical flow.

In order to fluidically balance the device and maintain a straight vertical profile, the fluidic channels must be matched to the resistance of the array. An equivalent resistance 'circuit' of the device is shown in figure 3-8. Each array of posts with a fixed gap is modeled with a single resistance (with a prefix R). Additionally, each side channel is

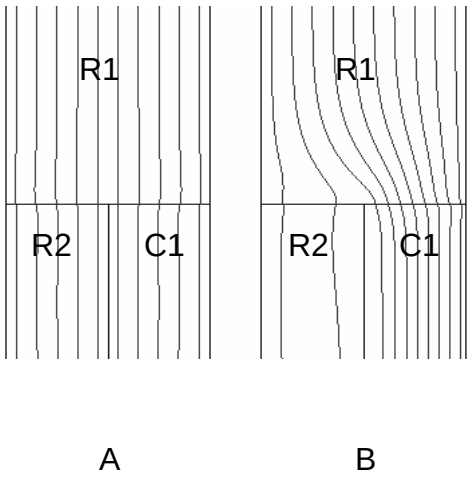

Figure 3-7: Streamline examples of a cascade device at the interconnection regions, using blocks to represent array regions. Simulated regions, R1 and R2 model an array of posts, while region C1 is a balancing region consisting of lengthy channels to carry the large particles from the device. (A) is a balanced device, streamlines are nearly vertical throughout the device. Any deviations in the straight streamlines are an artifact of the finite element analysis. (B) is an unbalanced, closed device where the channels for large particles has too low of a resistance. Since the streamlines are shifted to the right, particles smaller than the critical size will be displaced into the exit channels.

modeled with a single resistance (with a prefix of C). Equation 2-15 and equation 2-23 were developed to calculate the fluidic resistance of a channel and a DLD array respectively. These calculations are necessary to determine the number and length of side channels. Channel widths are selected to account for particle size, and to maintain low fluidic resistance.

The fluidic resistance of each array is calculated using equation 2-23 (shown in table 3-7). To maintain the constant vertical flow within the array, the pressure drop across the device at any point must be equal. Therefore, the resistance of the side channel must be

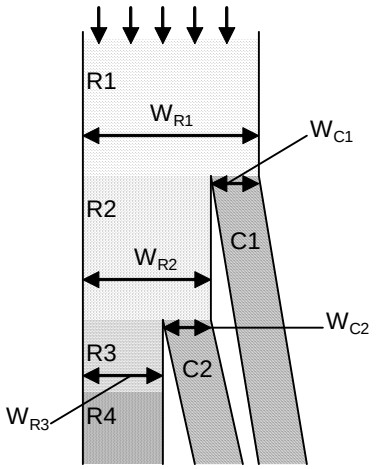

Figure 3-8: The design of a cascade device with two side channels for an equivalent fluidic circuit analysis. Each array and set of channels is modeled by a fluidic resistance, and conventional circuit analysis is used to balance the flow of each region.

Arrays		Side Channels	
Section 2: 8 micron gap 2100 micron wide 21.9 mm long	R2 $2.81X10^{10}$ N sec/m^5	C1 10 channels 16 micron wide 18.2 cm long	$5.33X10^{10}$ N sec/m^5
Section 3 and 4 4 and 2 micron gap 1400 micron wide 9.9 and 7.8 mm long	R3+R4 $2.82X10^{10}$ N sec/m^5	C2 15 channels 8 micron wide 3.35 cm long	$5.23X10^{10}$ N sec/m^5

Table 3-7: Channel designs necessary to balance the cascade device herein.

inversely proportional to the width of the portion of fluid entering that section (from equation 2-12). For a generic interface

$$W_C \times C = W_R \times R \,. \qquad \textbf{(3-1)}$$

Equation 3-1 defines an equal pressure drop and a constant vertical flow, maintaining the deterministic path desired.

For devices with multiple cascade exit regions, it is necessary to work backwards from the last exit region. Each previous exit region is designed to match the other parallel fluid paths. For example, the cascade device developed herein has a 1400 micron (W_{R2}) wide second region and a 1200 micron (W_{R3}) wide third region. Accordingly, the C2 region has a higher fluidic resistance, as it is only accepts the flow from 700 (W_{C2}) of the 2100 micron. This is represented by

$$W_{C2} \times C2 = W_{R3} \times (R3 + R4). \quad \textbf{(3-2)}$$

For the first section, the functional region is 3000 micron wide in contrast to the 2100 micron wide second post region. Therefore the first exit region is 900 micron wide (W_{C1}). However in this case the equivalent resistance of the entire region beyond the second array must be considered,

$$W_{C1} \times C1 = W_{R2} \times R_{eqv} \quad \textbf{(3-3)}$$

where for this device

$$R_{eqv} = R2 + C2 \| (R3 + R4). \quad \textbf{(3-4)}$$

Knowing the total resistance of each region, a channel width was selected to prevent particles from clogging. Equation 2-15 was modified for a set of N parallel channels,

$$R = {}^{12\mu L}\!/_{NW^3 E}. \quad \textbf{(3-5)}$$

The parameters W, N and L are chosen to realistically fit the region of interest. Table 3-7 provides the resistances and parameters for the cascade design used herein and described in table 3-6 and figures 3-6 and 3-8.

Each array and group of channels is simulated in a finite element analysis to demonstrate optimum designs relative to unbalanced designs. This can be achieved by drawing each region of exit channels and each array as a single region. The regions with posts are simulated by replacing the actual viscosity of the fluid in that region with

$$\mu' = 4.6\left(\mu / G^2\right). \qquad \textbf{(3-6)}$$

The correct pressure-velocity relationship is maintained by changing the viscosity of the simulation for each individual post region. This simulation confirms the calculations of the cascade design, as shown in table 3-7. A simulation of a single closed interface between two array regions and an exit channel is presented herein. Figure 3-7 shows this simulation with both an unbalanced and a balanced cascade design.

4 Experimental Methods

The experimental procedures are divided into four major sections. Subchapter 4.1 is an in depth description of exactly how to fabricate a complete DLD design, from the choice of materials to a finished device that is ready to be loaded with buffer. This is followed by the blood preparation procedures in subchapter 4.2. Subchapter 4.3 describes all of the procedures involved in running a separation experiment, including device preparation. The chapter concludes with subchapter 4.4 a post-run analysis looking at cell removal from the chirped design and analysis by other conventional methods.

4.1 Fabrication

The fabrication of a device consists of a number of steps, each of which will have a section herein. These combine the personal observations and experiments of the author, as well as many other present and previous members of the PRISM laboratory to develop what I consider the 'best' way to build a DLD device.

4.1.1 Device and Mask Design

Using the methods discussed in chapter 2 and 3, a device is first designed, including basic layout and size requirements. The design consists of one mask, which has a single etch to place the location of the fluidic channels. If possible more then one device can be placed on the same mask. Each design is drawn using a Computer-Aided Design program such as L-edit (Tanner Research, Monrovia, CA), which was used for the designs herein. A 6-inch glass plate with the mask patterned in chrome can then be

purchased from Photosciences (Torrance, CA). The Photosciences fast track program is particularly useful because in the large size range (>3 micron) the company has a turn around time of 48 hours. The mask should consist of a single layer transferred to the chrome, in which the location of the etched regions is transparent.

4.1.2 Material Options

Devices have been constructed in silicon, PDMS, and fused silica. Each has advantages and disadvantages. The main advantage of fused silica processing is the transparency for optical measurements and the ability to use large electric fields to drive the fluid electro-osmotically. Since neither of these is needed for blood applications, that material is not used herein. Silicon processing is the most understood, and has the largest number of options for etching. It also is able to support very high aspect ratios. PDMS has the advantage of having high bio-compatibility[56]. However, the softer PDMS can only support much lower aspect ratio posts. Therefore silicon is the base material for all devices herein.

4.1.3 Lithography

All devices were constructed on 100-mm silicon wafers. The wafers were cleaned with piranha etch consisting of a ratio of 3:1 H_2SO_4 and H_2O_2 followed by a 1 minute dip in 10:1 HF and H_2O. AZ-5209 (Clariant, Charlotte, NC) photoresist was used. The spinner recipe consisted of 75 RPM for 10 seconds at an acceleration of 500 RPM/sec^2 to allow for an even distribution of resist, followed by 3000 RPM for 30 seconds and 1000 RPM/sec^2 deceleration. This gave a thickness of 0.9 micron, which was found to be optimum for features greater then 1 micron. The wafers were soft-baked for 2 minutes at

95° C, and cooled for 5 minutes. The photoresist was exposed for 24 seconds using the MA-6 mask aligner (Suss MicroTec, Doylestown, PA) in hard contact mode. The wafer was developed for 75 seconds in 1:1.2 MIF 312 (Clariant, Charlotte, NC) and H_2O. A final hard bake was 4 minutes at 120° C.

4.1.4 Etching

All wafers were etched with a Bosch etching process[57] either at Cornell (Cornell Nanofabrication Facility), or assisted by a member of the Chou research group at Princeton. The Bosch process was used to give nearly vertical sidewalls, and typical aspect ratios of greater then 6. The depth of the devices was varied from 10 to 75 micron, with a sample SEM in figure 4.1. An oxygen plasma clean was found to be the quickest way to remove the remaining resist, which was toughened from the Bosch process. This was done in the Plasmatherm 790 at Princeton (Plasmatherm, Unaxis) with a pressure of 100mTorr, 40 sccm O^2, and 100W for 5 minutes.

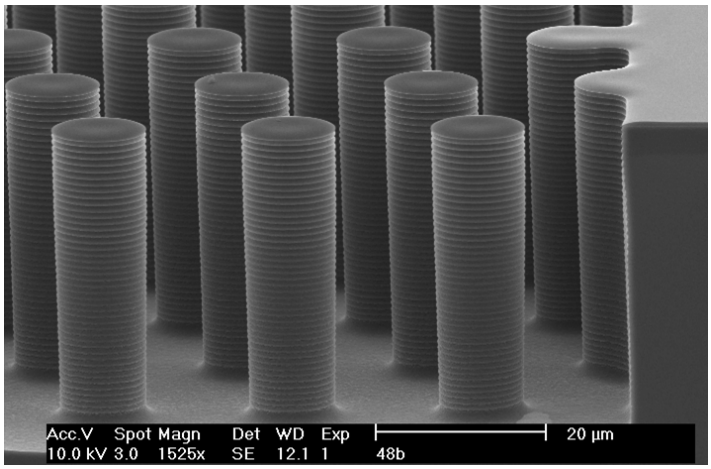

Figure 4-1: Scanning electron microscopy image of the posts of a DLD device etched at Princeton with the assistance of Keith Morton. Note the scalloped edges of the posts created by the Bosch process.[57]

4.1.5 Device Separation and Inlet Wells

The individual devices were separated and the excess silicon removed from the sides. Wafers were carefully cleaved, or sawed using a K&S 982-6 Wafer Saw (Kulicke & Soffa). All of the devices used in herein were separated by the wafer saw. A thick layer of photoresist (> 50 micron) was spun onto each of the wafers, and baked out (>5 min) to create a protective layer against saw dust. The written procedures were followed for the wafer saw programmed to cut silicon[58]. Each individual device was cleaned with acetone and IPA.

As described in subchapter 2.1, the device under test was placed upside down with a plexiglass chuck on top of the wafer. Fluid entered the device through the plexiglass. Therefore holes through the silicon to connect the device to the outside world. The best method found for placing connection holes through the silicon wafer was a sand blasting dental tool, which produced 0.5 to 1 mm holes. The device was protected from sand dust created during this process. First a crystallized wax was heated on a very thin piece of glass. This glass was placed over the region for sandblasting. The glass was an additional layer of protection which slows the rate of sandblasting. This process was repeated for each region of holes and for both sides of the wafer. Then a very thick (1mm) layer of photoresist was applied to the top of the wafer, by pouring a small amount on to the wafer, and baking out for 10 minutes. The process will melt the wax again, so aluminum foil was used to avoid leaving a mess on the hot plate. Finally a layer of tape was used to protect the important device region.

The tool in figure 4.2 was used to create the sandblasted holes. The nozzle fires sand at the wafer, and drills a single hole. By positioning the nozzle at each of the desired locations, all of the connections through the wafer are drilled.

The procedure is as follows.

1. Place the sand gun into a fixed stand positioned about 3 mm above the wafer stand.
2. Adjust the sand setting with a test run on a dummy wafer. Align the desired location of the hole between gun and its reflection in the silicon. The thickness of the wax and glass allows for a very short burst of sand to be used to double check alignment.
3. Blast until the wafer 'sounds' like it has been completely cut (change in pitch because of lower resistance to the sand), and then an additional 2 or 3 seconds.

Figure 4-2: The setup used for sandblasting holes through the silicon wafer, to allow fluid and cells to enter and leave the device from the back.

4. Remove to verify. When complete with each hole from the top, turn the wafer over, and redo each of the holes for 5 seconds. This will widen the hole enough for a pipette tip as well as straighten the side walls, about 1 mm.

After all of the blasting, first rinse the whole device in the sink next to the tool. This will remove the gross particles. Then, in a solvent hood, remove the tape, and rinse the device with IPA. This will only strip the very top layer of photoresist, dislodging more particles. The glass slides and wax are removed with acetone. This must be done very carefully to never let acetone dry on the device or the wax and acetone mixture will not be easily removable. The acetone is quickly rinsed with IPA. A final additional oxygen plasma, as described above is required.

After cleaning, some of the devices were coated with a fluoro-silane vapor (SIT 8174.0, Gelest Inc. Kent, ME). This coated the inside of the channels and decreased the cell adhesion.

4.1.6 Sealing

PDMS from Dow Corning (Midland, MI) was used, which was mixed at a ratio of 10 to 1, PDMS to curing agent by weight. The mixture was stirred for at least 5 minutes, and degassed to remove bubbles under house vacuum for 30 minutes. Two methods were used to create the PDMS sealing layer. In one method, a thin glass side was coated with PDMS and spun to create a layer of about 25 micron. Alternatively, a thicker layer of about 1mm was poured directly into a Petri dish. In both cases, they were cured over night at a temperature of about 80° C. These layers were applied to the device directly after plasma cleaning or fluoro-silane deposition. Devices which sat for a few hours after sealing before loading fluid were found to have a stronger seal.

4.1.7 Fluidic Connections

A plexiglass chuck was designed to interface the etched silicon wafer with applied pressures, and to allow volumes to flow (see figure 2-2). A chuck, shown in figure 4-3, was connected with the device by a number of O-rings. The device was held into position with 4 to 6 screws into a metal plate. Drilled into the plexiglass were a number of different kind of plastic interconnects, tailored to particular applications. Herein, interconnects were removable so that samples could be easily pipetted in and out, and tubes were connected for application of pressure to create flow.

4.2 Blood Preparation

Blood was freshly obtained from a self finger prick with a lancelet (BD, Franklin Lakes, NJ). A typical blood draw consists of 50 microliters. The blood was placed into a

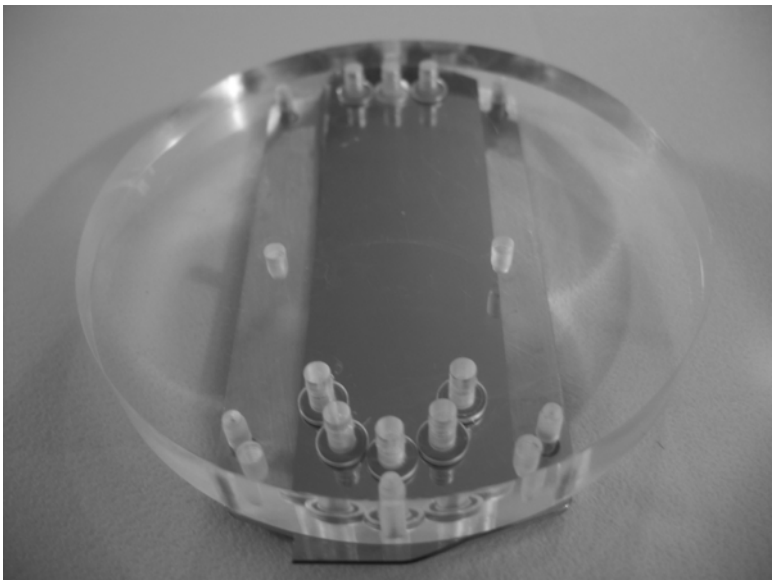

Figure 4-3: A sample chuck used for loading and unloading fluid into my microfluidic device.

blood collection tube (BD) which was pre-coated with either heparin or lithium heparin as an anticoagulant. The blood cells easily settle so it is important to agitate before each additional step.

White blood cells were stained in two ways. Hoechst 33342 is a nuclear stain that only affects cells with a nucleus, so it stains all white cells but not red cells and platelets. One microliter of stain was used for 50 microliters of blood. The mixture was incubated for 15 minutes at 37° C. The second fluorescent method used antibodies to target specific types of cells. A number of different antibody markers were used which were tagged with the fluorescent marker PE and observed under a microscope, or additional fluorescent tags were used for multicolor imaging within a flow cytometer. All markers were obtained from BD Biosciences. Antibodies to CD45, CD3 and CD19 were used to delineate all leukocytes (general white blood cell marker), T lymphocytes and B lymphocytes, respectively. Antibody to CD62P was used to quantify platelets.

The markers were stored at 5° C. Each was allowed to reach room temperature before being placed into the blood sample. The stain was added at a ratio of 1:5 with the blood, and then incubated for 15 minutes at room temperature. If the staining was done after the blood has been run through the device, the decrease in the cell concentration because of the dilution from buffer in the device must be taken into account. It is possible to do both staining procedures on the same blood consecutively. Simply do the Hoechst incubation before the CD antibodies are added, since the CD antibodies will be negatively affected by the higher incubation temperature of the Hoechst procedure.

4.3 Microfluidic Experimental Procedures

The microfluidic experimental procedures are broken down into four sections. They are the device preparation, the microfluidic setup, the actual experiment and the cleanup. The sealed device first needs to be loaded for the fluidic experiment. I discuss the equipment setup that was used for the majority of the experiments. A basic protocol is given for a typical experimental run. Finally a section about cleanup is included.

4.3.1 Device Preparation and Loading

The chuck mentioned in section 3.2.2 was first cleaned with soap, rinsed and dried. New O-rings were used for each experiment. The sealed device was positioned onto the chuck, and aligned to the O-rings, by using a light source to look through the sandblasted holes. The metal brace to hold the wafer in position was lightly screwed into position as seen in figure 4-3 (and figure 2-2). The alignment was double checked, and the screws carefully tightened until a seal was observed in all of the O-rings.

One of two blood buffer solutions were used within each device: autoMACS running buffer (Miltenyi Biotech, Auburn, CA), or phosphate-buffered saline, with biovine serum albumin (BSA) and 0.09% sodium azide. A 2 g/l solution of the triblock copolymer F108 (BASF, Mount Olive, NJ) was added to reduce cell adhesion to the device[59]. Solubility of the F108 was assisted by agitation, and the mixed buffer was degassed in a vacuum for a few hours, so bubbles did not form within the device when a negative pressure was used to create a flow.

The buffer was loaded into the inlet wells at one end of the device, and a negative pressure (typically with a syringe) was applied to all of the exit ports to draw the buffer into the device and out the other end. A plexiglass attachment was used to apply the

pressure equally on all exit wells. Bubbles were observed to form within the device. These bubbles will completely disrupt linear flow within the device if not removed. Also the complex geometries often trap the bubbles, making it hard for them to simply flow out of the device. The high gas solubility of the PDMS facilitates bubble removal.

Placing the loaded device and chuck into a vacuum of about 0.5 psi, without any other fluidic connections for 15 minutes, followed by room pressure for 15 more minutes allows additional bubbles to degas. Repeating this process facilitates the removal of all bubbles. I often let the device sit overnight, to make sure all bubbles have had a chance to dissolve, and allow the F108 to completely passivate the surface. Any stationary bubbles will disrupt the flow of fluid through the device: one should check again the removal of all bubbles before loading the device with any sample, by applying a small negative pressure with a syringe and seeing if any bubbles form. If no bubbles are seen, the device is ready for testing.

4.3.2 Experimental Microfluidic Setup

All experiments conducted in Princeton were performed on an inverted microscope in a bio-safety level two environment in the Austin Lab at Princeton University. Illumination consisted of both a white light and a mercury-xenon fluorescent lamp, which has emissions of interest at 360 and 550 nm. Two fluorescent tags were used Hoescht 33342 which will be absorb light at 360 nm and emit at 450 nm, and phycoerythrin (PE) which will absorb light at 550 nm and emit at 585 nm. The microscope was equipped with mirror cubes to observe these two markers independently. The setup is shown in figure 4-4.

Figure 4-4: The microscope setup used herein. The device in a chuck is placed on the stage of the inverted microscope. Fluidic connections are made from the top. The CCD camera is visible in the lower left corner.

Imaging consisted of two camera options. The majority of data was visualized using a CCD camera which gave color imaging. This was used for the majority of the images in this thesis because it allowed for easy contrast between red blood cells with white light, and white blood cells with fluorescent tags. For more difficult contrast images of platelets (ie to notice the location of weak fluorescent tags) a Hamamatsu black and white camera was used. Data collection was either stored by digital tape recorder or either camera was directly connected to a computer.

With the device under test, flow was created with either a negative or positive pressure on the order of 0.2 psi. With negative pressure, a vacuum was applied to all of the exit wells equally by either a syringe or a vacuum pump. For the application of positive pressure to the entrance wells, a homemade system was used to create precise pressures. Herein, all multiple and chirped devices were driven with negative pressure

(subchapters 5.1 and 5.2) while the cascade devices were with positive pressure (subchapter 5.3).

4.3.3 Experimental Procedure

After the buffer loading was complete, a typical blood run consisted of 5 microliters of blood pipetted into the blood input well of the device after staining and agitation. Excess buffer from the exit wells was removed and all input wells were loaded with fresh buffer. One should be sure the blood well was less full then the other entrance wells (at least 1mm difference in height), as a difference will cause slight flows between the wells before the pressure is applied. This insures the cells do not enter the device early and flow into the buffer wells, contaminating them. The pipette for loading blood was placed into the blood well, about 1mm up from the O-ring, as shown in figure 4-5. The blood was slowly pipetted in, allowing it to sink down into the wafer region. If instead, the cells are pipetted directly into the O-ring, it is possible to force the cells all the way into the device and contaminate the buffer channels.

Even with the anticoagulant, the physical agitation of the cells eventually causes them to stick. Usually after about an hour of running, a significant number of cells stick within the device. These stuck cells obstruct the flow pattern and the device is no longer functional. Therefore all experiment times were less then an hour.

A typical run involves observation of the interested stained cells within the microscope, at various speeds. Areas of interest include the exit channels of the device to observe the final fractionation, as well as within the array to observe the detailed mechanics of the paths of cells. A digital tape recorder is used to watch regions until the

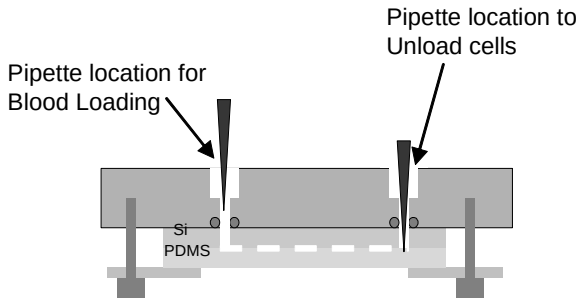

Figure 4-5: The location of the pipette when loading and unloading blood cells into the chuck.

desired numbers of cells have passed. Variations in this procedure are noted with the results of each individual experiment discussed in chapter 5.

4.3.4 Cleanup and Device Reuse

After the experiment, and removal of all interested cells, (as described in subchapter 4.4), waste was disposed in the red biohazard container, and all non-disposables were cleaned with freshly diluted bleach. The PDMS and glass portion of the device can be removed, and the silicon portion reused. To clean the silicon, first rinse it with acetone and IPA to remove gross contamination. Then clean it with piranha etch consisting of a ratio of 3:1 H_2SO_4 and H_2O_2 for at least 15 minutes. Finally an oxygen plasma treatment as described above is used to prepare the device for sealing with a newly cured PDMS layer.

4.4 Post Run Analysis

To analyze the output of the microfluidic devices, cells were removed and analyzed by conventional means. There were a number of technical issues that were first resolved

in order for a measurable concentration blood cells to be obtained. The two conventional methods for looking at concentrations of cells are the hemocytometer and the flow cytometer. Procedures for working with both of these are described in this section.

4.4.1 Cell Removal

As can be easily observed if a test tube is left overnight, blood cells are affected by gravity and settle out of solution. This effect is strong enough that it can be observed to take place within the input or outlet well of a DLD device during the time it takes for a complete experiment (on the order of an hour).

To explore settling, the input well was analyzed. The concentration of cells entering the device was measured by counting the number of white blood cells (by optical inspection), and compared to the concentration of the whole blood used. Figure 4-6 shows the concentration over time. Note the concentration of the unmixed case first goes up and then decreases over time, until a large spike at the end. It is unclear if this spike at the end is because of floating cells at the end of the liquid in the input well, or if settled cells are finally dislodged by the surface tension of the end of the fluid.

A method to counter act this effect is the addition of micro stir bars to agitate the cells and combat settling. A 2-mm micro stir bar is placed in the plexiglass well and driven by a motor and an external magnet. This technique was found to be particularly useful on the input blood well. Placing the stirbar inside the blood inlet well mitigated the effects of settling as shown in figure 4-6.

For the data collected in figure of 4-6, in both experiments a total of about 2,000 white blood cells were counted. One microliter of whole blood was pippetted into the inlet well, therefore a concentration of 2000 white blood cells per microliter was counted.

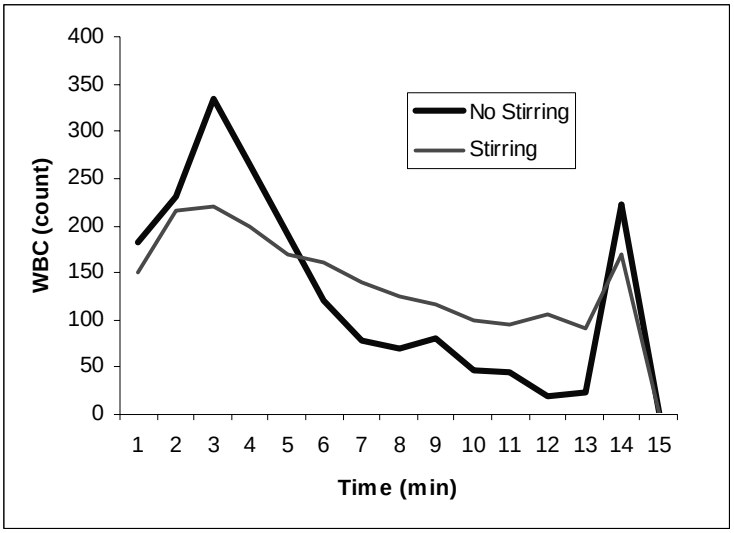

Figure 4-6: Measurement of white blood cell count at the end of a device over time. The first spike in both curves is due to settling in the input well, and the spike at the end occurs as the input well supply is exhausted. Stirring reduces but does not eliminate the spikes.

This is a reasonable white blood cell concentration, as will be discussed further in section 5.2.5.

The stirring effect was not found to be as beneficial on the exit wells, because of the much lower concentration of cells. The cells were found to be mostly located in the sand-blasted silicon region. Therefore the fabrication process of sand blasting from both sides, as described in section 4.1.5 which widens the sand blasted holes so the pipette can be placed to remove the cells directly from this region was used, as shown in figure 4-5.

After completion of the experimental run, each individual output well was pipetted out. The pipette must be placed through the hole in the silicon until it is observed to displace the PDMS seal, because the cells will settle down to the PDMS layer. The pipette was then pulled up slightly until it is no longer seen to displace the cap and suction was applied. This removal of fluid will create a pressure difference between the

exit wells, and a small flow. Therefore, be sure to complete the process quickly as cells are observed to flow back into the device from the wells. Starting with the most important well, the removal was performed in a single suction on each well. All of the results from this thesis used this technique to cell removal. Ideally, in future designs, this would be completed by an automated system which applies the same pressure to all wells for removal. Settling will be an important issue in future three dimensional fluidic systems designed for blood. Mixing within the exit wells of the device will be a necessary and important addition for a fully functional total analysis system.

4.4.2 Hemocytometry

The hemocytometer is a device which holds a known volume and has grid lines to easily count cells under a microscope. It can be used to measure the concentration of cells in output wells.

The hemocytometer was used to compare cell counts with those optically observed. An experiment was conducted to compare cell count observed within the device to those counted outside the device. A run in a chirped device was conducted and the position of the cells exiting the device was measured and is shown in figure 4-7. The device had five exit sections collecting volume from lateral regions indicted in figure 4-7 with dark black lines. There were several exit channels leading to each exit well. The white blood cell count from visual inspection of the flow in each exit channel is shown with a blue bar. Eight 1.0 microliter volumes were removed and measured from each exit channel for the analysis of both red and white blood cells by the hemocytometer. Table 4-1 shows the average concentration of cells counted within the exit channels of the device.

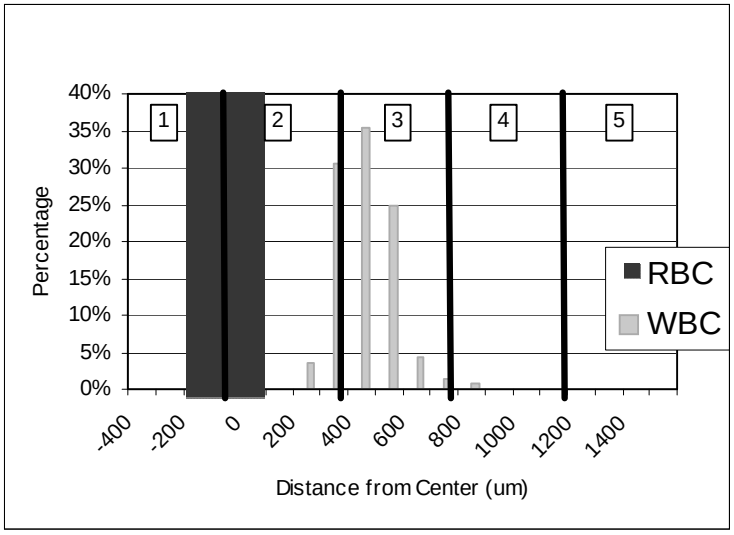

Figure 4-7: Observed count of the red and white blood cells versus position in exit channels for the same experiment as that of the hemocytometry measurement. The red bar is the region where red blood cells are observed. The blue bars are histogram showing concentration of white blood cells.

The two methods agreed that no white blood cells were located in the first and last columns. The three center columns were found to have concentrations of the same order of magnitude. The third exit well showed the most agreement, and had the majority of the cells. The center column had 67% of the cells for the hemocytometer measurement compared to 64% of the total cell count with visual measurement. The second and fourth columns had 26% and 7% in the hemocytometer, respectively, compared to 34% and 1% for the visual measurement.

The hemocytometer shows for white blood cells, the concentrations were found to qualitatively correspond to what was observed exiting the array, with the majority of the cells in the center channels, and no cells present on the edge exit wells. An interesting observation was made with the red cells. Within the device, no red blood cells were observed within the far three channels. However, while the majority of red cells were in

Hemocytometer Measurements taken outside of device:					
Well	1	2	3	4	5
Reds	593K	1.28M	6.72K	7.65K	450
Whites	0	1.23K	3.24K	338	0
Ratio	INF	1030	2.07	22.7	INF

Table 4-1: Cell counts obtained from the hemocytometer from the cells removed from the device. For example, channel 3 has 67% of the total white blood cell count compared to the 64% total in the histogram in figure 4-7.

the first two wells, about 3% of the red cells were observed in the third and fourth channel when counted with the hemocytometer. These red blood cells would have been displaced within the device, and not easily seen optically. Some of the experiments in chapter 6 will verify the displacement of the red cells, and subchapter 6.3 will give some theories about an explanation.

4.4.3 Flow Cytometry

Flow cytometry is a technology that measures physical characteristics of single cells, as they flow in a fluid stream which crosses a laser beam. The properties measured include a particle's relative size, relative granularity or internal complexity, and relative fluorescence intensity, based on attachement of fluorochrome conjugated antibodies to expressed proteins. These characteristics are measured using an optical detector that records how the cell or particle scatters incident laser light and emits fluorescence.[60]

A flow cytometer is made up of fluidic systems, optics, and electronics. The fluidics transports cells with a stream to the laser beam; and the optics consist of multiple lasers to illuminate the particles and a set of optical filters and detectors. Some instruments are also equipped with a sorting feature, and are capable of using real time collected data to

make sorting decisions, and deflect particles. Any suspended particle or cell from 0.2–150 micrometers in size is suitable for analysis[60].

There are a large number of antibody types developed for a wide varity of cell types. Each of these antibodies can then have a different fluorescence emission. These flourescent antibodies are used to detect different cell types. Complex multi-channel analysis and sorting decisions are all possible. However, herein flow cytometry was used to quantify the presence of leukocyte subsets eluded from a particular outport. Unfortunitely, flow cytometry is a tool designed to look at tens of thousands of cells, while I was looking for hundreds, or even a single white blood cell to verify whether any came out of the left most channel. While the thresholds for detection can be easily adjusted, one must then be conserned with false positives, from background noise. Therefore, the experience of the Wadsworth Center in the New York State Department of Health (NYSDoH), particularly Renji Song was used as a guide to select the best device parameters. It is also very important to clean the machine with DI water after each run, because this analysis is of samples with much lower concentrations then is typical for flow cytometry.

4.4.4 Flow Cytometry Analysis

Because of the large concentration differences between the red and white blood cells, the flow cytometry analysis of each cell type will be done separately. For the analysis of white blood cells, the red blood cells were lyzed. In order to get an accurate measurement of concentration, each set of mixtures was placed into a Trucount test tube (BD Biosciences), which contains an exact number of fluorescent beads, to allow calculations of cell concentrations.

Samples were analyzed on a FACScan (BD Biosciences) flow cytometer at the Wadsworth Center in collaboration with Dr. David Lawrence. The conventional flow cytometry analysis of forward scatter (FSC), side scatter (SSC), and up to three fluorescent colors can be conducted. The samples were not washed, as is typically part of the lyzing procedure, so there was still a large concentration of small broken red blood cell pieces. Therefore, a more informative picture is found by gating on the intensity of fluorescent tag on CD45, which is shown in figure 4-8. Three sections are clearly visible. All of the red blood cell pieces were found in the region of low fluorescent intensity, while all white blood cells which will be tagged with the CD45 antibody will fluoresce at a higher intensity. Finally, the Trucount beads are designed to fluoresce at a very high

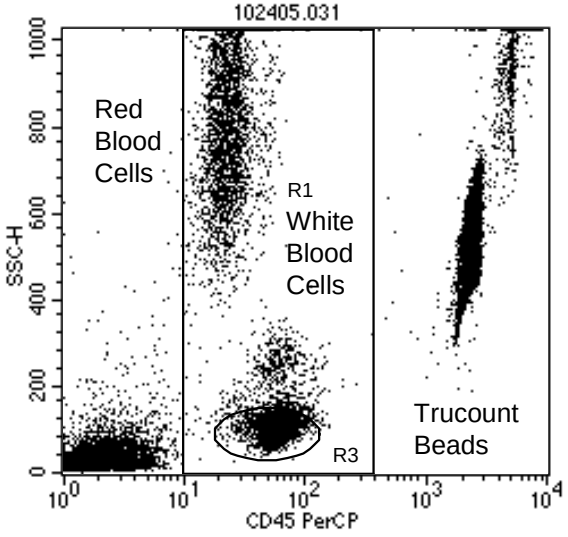

Figure 4-8: A flow cytometry measurement of whole blood with trucount beads. The x axis, a log scale, is concentration of PerCP with CD45. The y axis is the side scatter concentration. Red blood cells are not tagged. White blood cells are tagged to fluoresce, and Trucount beads emit at a much higher intensity. The Region R3 marks lymphocytes with a circle. Region R1 consists of all particles found of intermediate intensity, delineating the white blood cells.

intensity, to be clearly separate from the biological sample. The cell concentration can be calculated by counting the number of beads in this third section.

After the initial data measurement, the stored data was analyzed with a number of plots. For example, the whole blood data was gated so only the particles located in the middle section of figure 4-8 are analyzed (marked as R1). Each fluorescent color can be gated, and graphed versus another color or either forward or side scatter. An example of a forward versus side scatter, just looking at the white blood cells of whole blood gated is shown in figure 4-9. Lymphocytes, monocytes and granulocytes are grouped based on forward and side scatter. For example, region R2 are lymphocytes and region R7 are monocytes. These regions were outlined with the assistance of the experts of the Lawrence Group at the Wadsworth Center in agreement with literature[61].

Figure 4-10 shows the results of gating for the particular white cells of interest. The

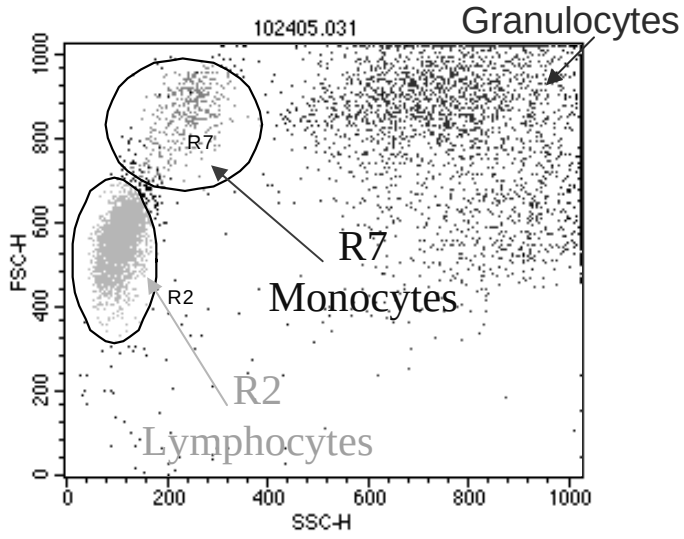

Figure 4-9: A forward scatter versus side scatter plot of whole blood, gated for just the white blood cells. Note the three major types of white blood cells are marked in different colors.

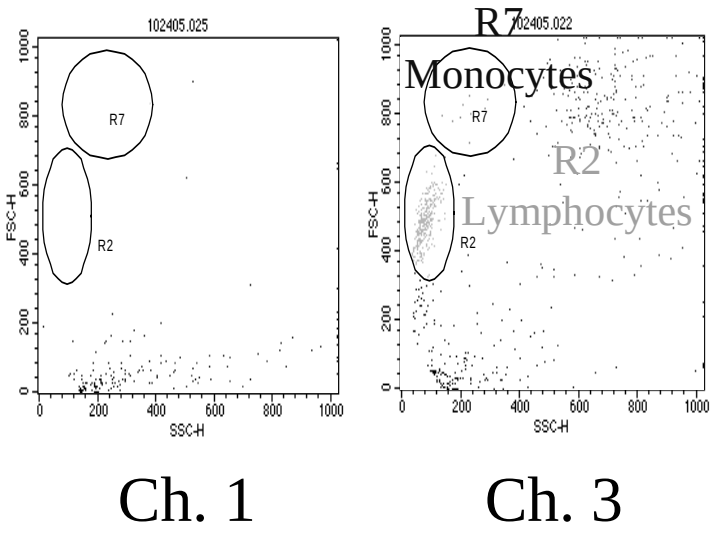

Figure 4-10: Data collected on the forward versus side scatter of cells from a DLD device, with flow cytometry. The first channel is the un-displaced location, while the third channel is the location designed for the majority of white blood cells.

experiment and the results will be expanded upon in section 5.2.4. White blood cells are not observed in the first channel, which is the location where the fluid travels straight through the device. However, the third channel has a large concentration of white blood cells, as they were displaced within the device. In summary, this section verifies the resulting cell counts observed optically exiting the device matches the flow cytometry concentrations measured within the exit wells.

5 Fractionation of Red Blood Cells, White Blood Cells and Platelets

A large number of various experiments on separation of blood components were conducted, and these summarize the most successful or interesting observations. The results are presented not in chronological order, but in an order matching an overall theme for the direction of the research. The chapter has been divided into four parts, one for the results obtained from each of the three different device types: multiple (5.1), chirped (5.2) and cascade arrays (5.3), and a final section on cell viability (5.4).

5.1 Multiple Array Separations

The multiple array device was the first successful separation of blood into its main components of red and white cells and platelets. It consisted of two different regions, the first of which separates the white blood cells from the red blood cells, and the second of which separates red blood cells from plasma.

5.1.1 Device Description

The multiple array device design was described in detail in section 3.2.1, and in table 3.4 and figure 3.3, with an additional schematic of the device shown in figure 5.1. The first region, with a critical size of 10 micron, was larger than the majority of cells. The second array region consisted of a post and gap size of 10 micron. This gave a critical threshold of about 5 micron, ideal for the separation of white blood cells from the whole blood mixture. The third region consisted of a post and gap size of 5 micron, which gives a critical threshold of about 2.5 micron. This criterion allowed the red blood cells to be

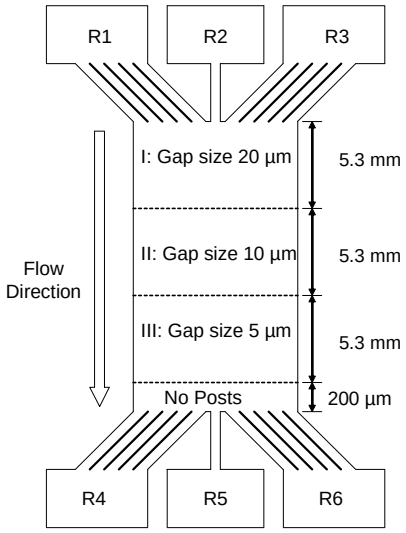

Figure 5-1: A schematic of the first successful blood separation device. This multiple array device is physically described in section 3.2.1.

displaced from the rest of the blood mixture which included platelets and plasma. The device was intended to be an analytical mode device, meaning only small volumes of blood would be studied. Because of an error in the design of the channel from R2, the flow stream of the blood was widened from 20 to about 200 micron when entering the device. The injection was located at the center of the array, and all of the outputs were connected to a single output well. The device had no method for removal of the separated streams after separation. Therefore, all data was taken by imaging the flow of blood through the device.

5.1.2 Separation of White Blood Cells

A blood run was conducted as described in section 4.2, with the following clarifications. White blood cells were stained with Hoechst 33342 nuclear stain. The higher density of red blood cells prevented individual counting. Instead, the light

scattering of the red blood cells was used, by microphotographic image analysis. The final position of both red and white cells was measured at the end of the second array. Using equation 2-15, the fluidic resistance of this device was $1.0x10^{12}$ N sec/m^5. This corresponded to velocity of 200 micron/sec at a pressure of 0.1 psi. The cell positions before and after the array are shown in figure 5-2. Within the region, the white cells immediately began to separate from the smaller blood components. With diameter sizes greater then 5 micron, the white cells were above the critical threshold size for the region and no longer followed the streamlines. They were instead displaced at each row of posts. At the end of region, the white blood cells were displaced an average of 490 microns from the flow of red blood cells and dye in solution, with an average displacement angle of 5.3°. This was close to the ideal displacement angle of 5.7°, implying the white blood cells were successfully displaced at nearly every row in this region. The white blood cells were completely separated from the red blood cells. Not one white blood cell (out of 200 observed) was seen within the flow of the red blood cells at the end of region. The red blood cells were observed to continue straight through this region. Figure 5-3 shows white blood cells separated from the red blood cell stream within the posts of the device.

5.1.3 Separation of Red Blood Cells from Plasma and Platelets

For this experiment, again the procedures in chapter 4 were followed with the following clarifications. The platelets were stained with CD-62P labeled with PE and not washed. This portion of labeled antibodies did not bind to the platelets and remained in solution. Since these molecules were significantly smaller than the critical size for any of

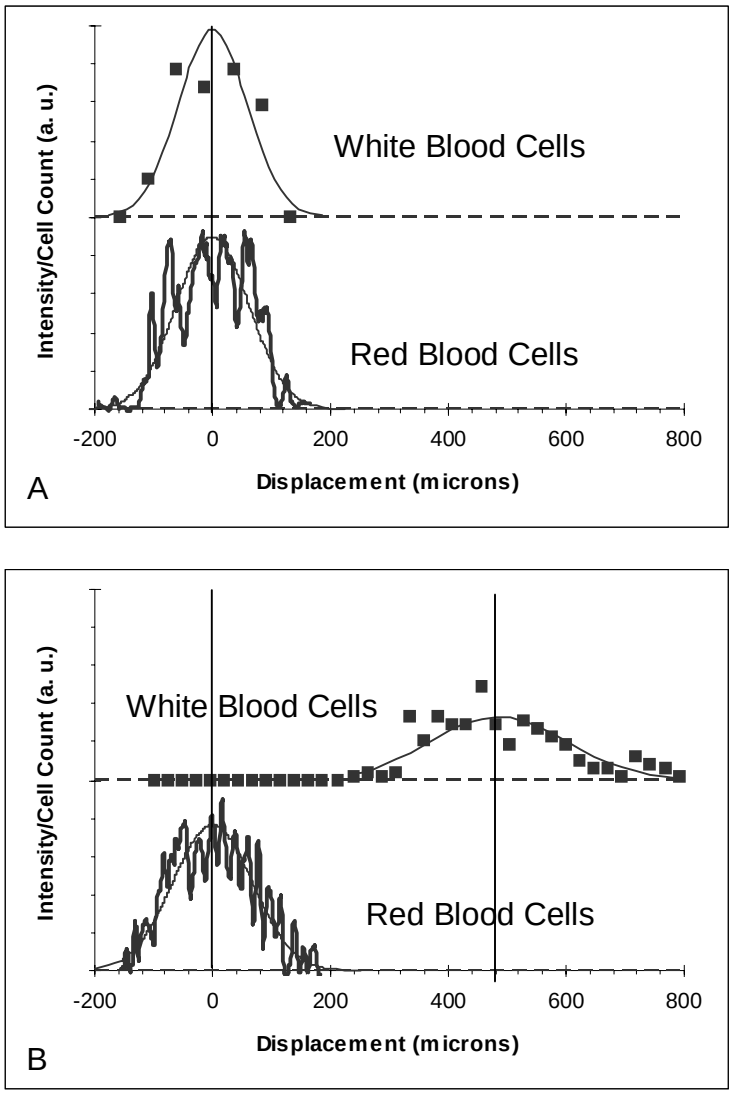

Figure 5-2: First successful separation of white and red blood cells in a DLD. A and B are histograms of cells versus lateral displacement at the beginning and end respectively, of a single functional region of gap size 10 micron and shift fraction of 0.1. The white cells were individually counted while red cell intensity was measured optically. The spikes in the optical measurement are an artifact of the posts.

the regions, they were used as a marker for plasma flow through the device. The observations of this experiment are shown in figure 5-4. In the third region with a threshold of about 2.5 micron, the red blood cells were displaced. By the end of the region, the red blood cells were completely separated from the remaining dye in solution

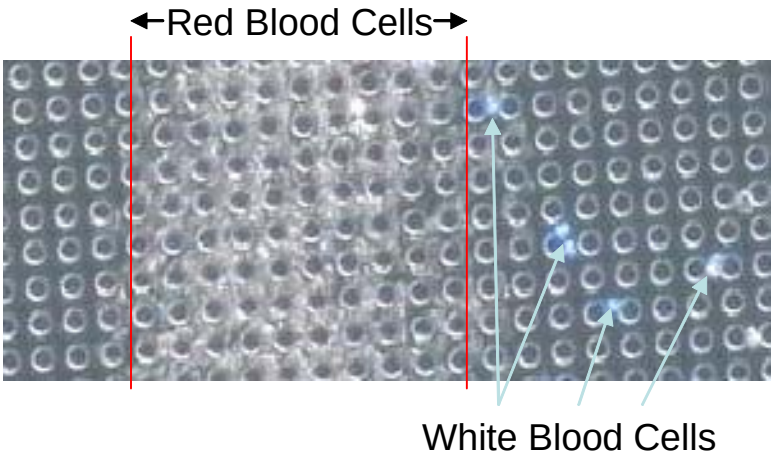

Figure 5-3:A picture of white and red blood cells within a DLD device, located high in the device, near the input, where the white blood cells just start to displace from the red blood cell stream.

and displaced an average of 390 micron from the background dye. This gave a separation angle of 4.3°, less then the ideal angle of 5.7 °. Figure 5-5 shows a picture of the red blood cells displaced.

Platelets stained with the CD62P marker were clearly observed exiting the device on average very slightly displaced (18 micron), as seen in figure 5-4B from the background dye, and far less then that of the red blood cells. Little or no displacement of the 2-micron size platelets (see section 3.2.1) was expected in this region because of the critical threshold of ~2.5 micron.

Technologically, there was no overlap of red blood cells with white blood cells, which were all separated in the second region. Therefore, white blood cells, red blood cells and platelets were all successfully separated. Displacements of white blood cells

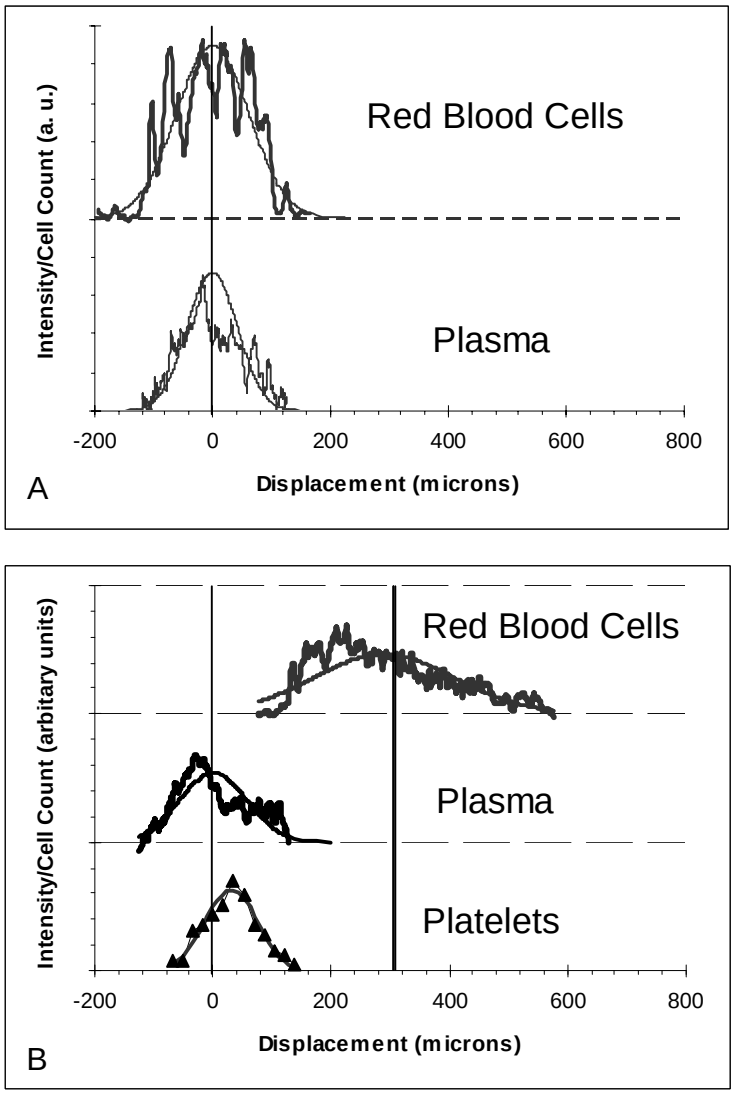

Figure 5-4: Displacement of red blood cells in a DLD. The device consists of a 2.5 micron gap and a 0.1 shift fraction. A and B are histograms of the position of red blood cells and plasma at the start and end of a third region which is displayed in figure 5-1. For both, the intensity is measured by the optical intensity. Additionally, platelets are observed and individually counted after exiting the device.

and red blood cells were observed. However, the degree of the separation was not measurable because individual red blood cells could not be imaged.

In this particular device all of the white blood cells get stuck in the beginning of the smallest array of the device. Therefore the large white blood cells are not separable from

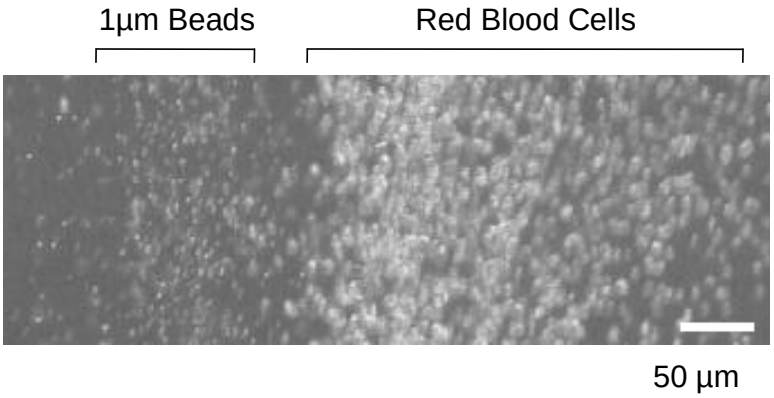

Figure 5-5: A picture of red blood cells and 1 micron red beads at the end of a multiple array design. The red blood cells are displaced in this device. The 1 micron beads mark the location of the plasma, as they were not displaced.

the red blood cells in a continuous flow within the device. In the rest of the chapter chirped and cascade designs are introduced and these alternative designs overcome this fault.

5.2 Chirped Array Separations:

Continuous Separation of White and Red Blood Cells

After the initial success, the focus of the designs shifted to creating a continuous separation and toward better understanding of the white blood cells for applications to immunology. Two different devices were used, A and B. They had a larger number of functional array regions (thirteen), each with a slightly different output criterion. The goal of both devices was to vary the critical threshold going from 3 to 9 microns with 0.5 micron steps.

Both devices consisted of a functional region 4.5 cm in length (the section of the device is arrays of posts), and were designed to fit the same chuck. They were etched to a depth of 50 micron and used a PDMS cap. Both version A and B were described in detail in section 3.2.2 with table 3.5 and figure 3.4. Version A was 2 mm wide, while Version B was twice as wide at 4 mm. Both designs consist of a significantly longer first region to enhance the separation between the white blood cell data and the native blood. The version B device is shown in figure 5-6 and the design criteria and input-output curve is presented in figure 5-7.

The design was an analytical mode, with a narrow throat of 50 micron, located at the far left side of the array, and both designs consisted of 5 evenly spaced outlet sections from which the cells could be easily collected and removed for other analysis.

5.2.1 White Blood Cell Size Measurements

The first task for the chirped device was to measure the size of white blood cells. The primary result of a device designed with these critical thresholds is a histogram of the separated individual white blood cells, based on size. An example is shown in figure 5-8.

The average white blood cell size is 6.7, which compares with 6.8 from the study by

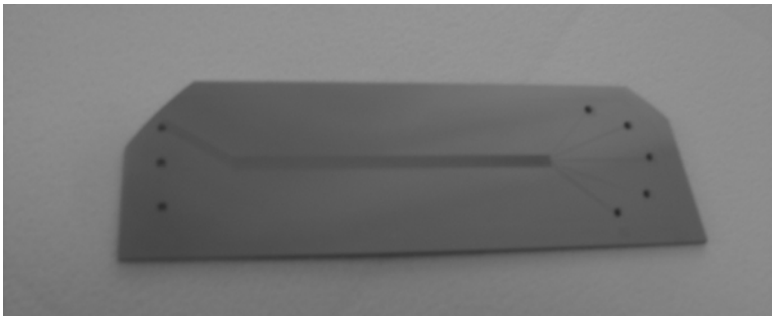

Figure 5-6: A picture of a chirped design with 13 different separation regions.

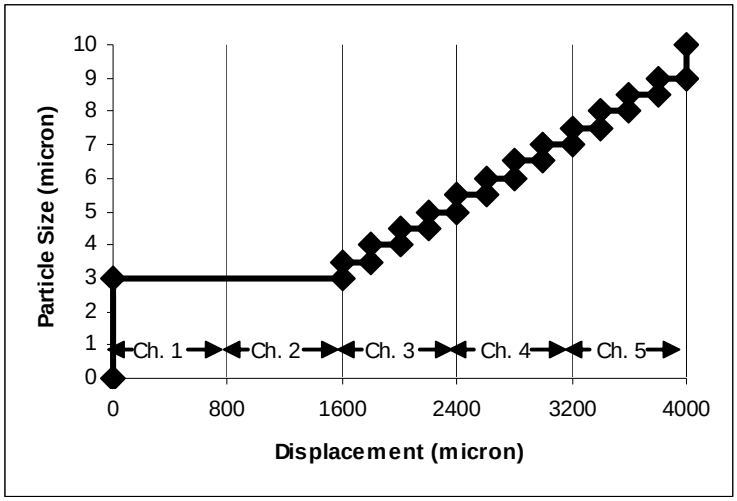

Figure 5-7: The transfer curve for the version B of a chirped device (Version A is shown in figure 3-4). The width of the device was doubled compared to version A, and the separation between the red blood cell stream and the white cells was increased. Channels 1 through 5 refer to what is collected by the output wells.

Schmid-Schöenbein *et al.*[12], which used a scanning electron microscope to measure cell size. Additionally, two sets of polystyrene beads of size, 5.0 micron and 8.4 micron, were used as a calibration. The expected size of the device does correspond to the displacement of the cells to various output channels. This allows the evaluation of the change in size of the white blood cells caused by environmental changes including the salt concentration of the buffer, and biological changes as can occur with cancers such as lymphoma (in section 6.3.5).

5.2.2 Effects of Salt Concentration on Size

It is known that the salt concentration of the buffer used to suspend the blood cells can change the size of cells through an osmotic effect. Similar to the approach in Schmid-Schöenbein *et al.*[12], the blood buffer used within the device was replaced with a

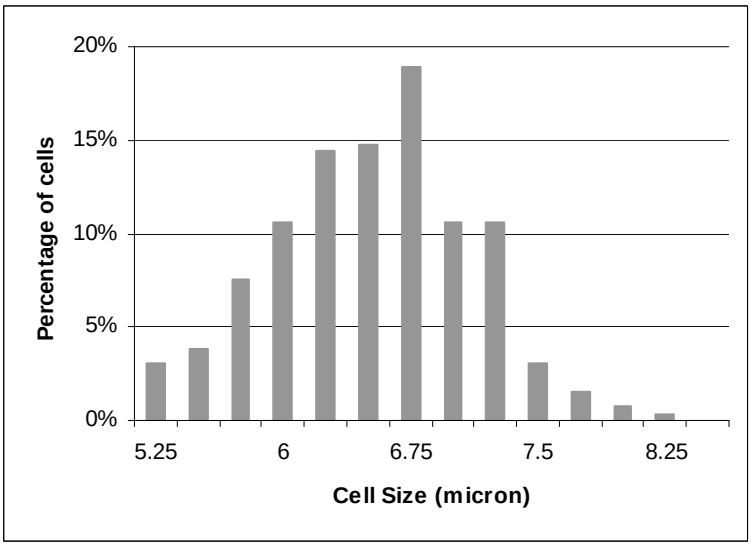

Figure 5-8: A histogram of white blood cells from a chirped version B device.

buffer of lower (150 mmol) and higher (450 mmol) osmolarity, along with a control of normal (300 mmol) osmolarity. Decreasing the osmolarity increases the size of the cell, while increasing it has the opposite effect. This is because the cell is trying to compensate for the change in salt concentration by increasing or decreasing the intake of solution. The procedure for this experiment for running blood was discussed in section 4.3, with the following additions. The three blood samples were analyzed. All white cells were labeled with Hoescht 33342 and the final position was measured. A histogram of cell count versus the effective hydrodynamic cell size is displayed in figure 5-9. The hydrodynamic cell size is defined as the size of a rigid spherical bead which has the same output location. The average white blood cell size was measured to be 6.3, 6.5 and 6.9 micron for the three osmolarities, compared to 6.1, 6.8 and 9.0 from the study of Schmid-Schöenbein *et al.*[12]. Clearly a change is occurring induced by environmental changes, which is confirmed by the DLD.

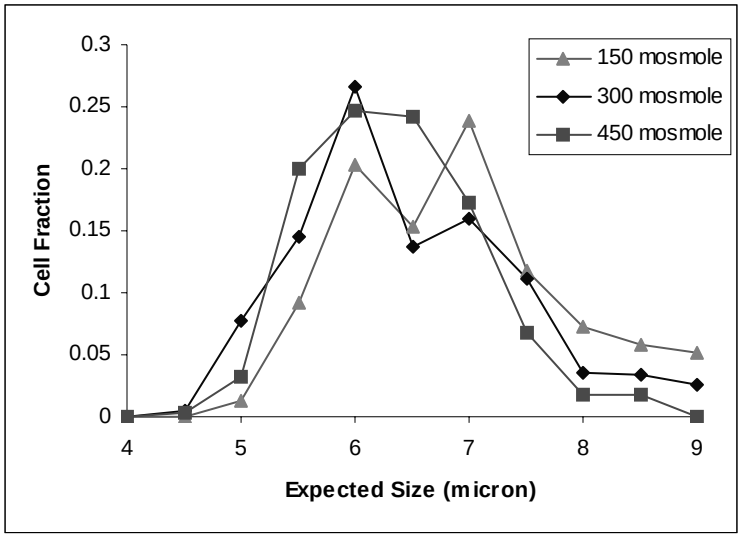

Figure 5-9: Histogram of cell fractionation versus hydrodynamic cell size showing the change of size of the white blood cells because of change in blood buffer. Average size changes from 6.5 micron to 6.3 micron and 6.9 micron. The effects are most obvious by looking at the change in cell fraction of the 8 to 9 micron cells.

5.2.3 External Analysis of Fractionated Cells

With successful analysis of samples within the device, the next important addition was the analysis of the separated output streams off chip by a standard accepted technique. Experiments were conducted in a chirped device. The solutions of each well were pipetted out of the device and analyzed by conventional flow cytometry or hemocytometry, as described in subchapter 4.4.

A large number of flow cytometry experiments were run with the assistance of the flow cytometry lab at Wadsworth Center in the New York State Deptartment of Health (NYSDoH), with a summary of results presented herein. Each experiment consisted of dividing the output of each channel in half in order to analyze both the red and white cell

concentration, as described in section 4.4.4. To identify white blood cells in the output and differentiate between different subpopulations, half of each channel output was stained by using antibodies to the following: CD45 (a generic WBC marker, tagged with fluorescent Per-CP), CD19 (a B lymphocyte marker, tagged with phycoerythrin, PE), and CD3 (a T lymphocyte marker, tagged with FITC), and lysed with FACSlyze to remove the red cells. The conventional flow cytometry analysis of forward scatter, side scatter, and three fluorescent colors was conducted, as described in section 4.4.4. A typical flow cytometry measurement is shown in figure 4-10.

5.2.4 Flow Cytometry Results

First the white blood cell analysis was conducted on a version A device by analyzing lyzed solutions from each of the chip's five output wells. Lymphocytes, monocytes, and granulocytes were grouped based on forward and side scatter. Lymphocyte analysis consisted of first gating on CD45 particles with low side scatter, followed by quantification of CD19 and CD3 cells by fluorescence, as shown in figure 5-10. The top figures are forward versus side scatter with only light scatter. Note red cells have been lyzed, so a small number of little particles remain in the mixture. The bottom figures take advantage of gating to look at a particular region, and fluorescence within the measured data. Only cells in region R2 which had above a threshold level of CD45 fluoresce were selected. This subset of particles is shown on the bottom figures. The fluorescent tags with antibodies for CD3 and CD 19 are the x and y axis respectively. Channel 1 is the straight direction channel, the location of cells which do not displace. Channel 3 is the center exit channel, in which the majority of lymphocytes were located.

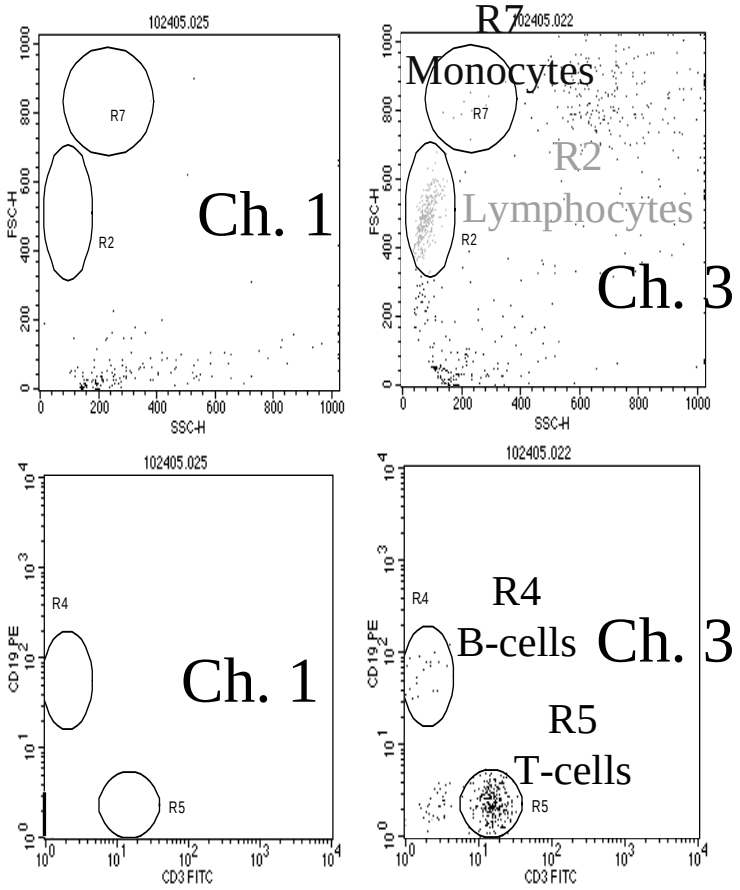

Figure 5-10: To identify the location of WBC, the output was removed, lyzed for removal of RBC, and stained using antibodies: CD45 Per-CP (WBC marker) CD19 PE (B-lymphocyte marker) CD3 FITC (T-lymphocyte marker). Forward scatter and side scatter were also used to group different kinds of WBC, as shown.

In figure 5-10, the top figures show no white cells in the first channel and a significant concentration of white blood cells in the third channel. Note a few pieces of lyzed red blood cells are visible in the figure. The bottom figures show no particles matching the gating criteria for lymphocytes were found in the first channel. All lymphocytes were displaced, and bumped out of the region where the fluid traveled straight through the device. The bottom right figure shows the various lymphocytes

which were found in the third channel. T-cells are shown as positive in CD3, and B-cells are positive with CD19. A small population of cells which are negative to both antibodies are seen, and these cells are other types of lymphocytes.

5.2.5 Analysis of Flow Cytometry Data

The data was tabulated for each channel, and the total cell count concentration for each white cell type was calculated and is shown in figure 5-11. One hundred percent of the lymphocytes (B cells and T cells) and monocytes were displaced into channels 3 and 4. Cells displaced between 400 and 800 micron from the undeflected flow (800 and 1,200 micron from the wall), were ideally extracted from channel 3 (hard sphere size of 4.5–7 micron), whereas cells displaced 800–1,200 micron were ideally in channel 4 (hard sphere contact size of 7–9 micron). Conventional methods of measuring white cells show

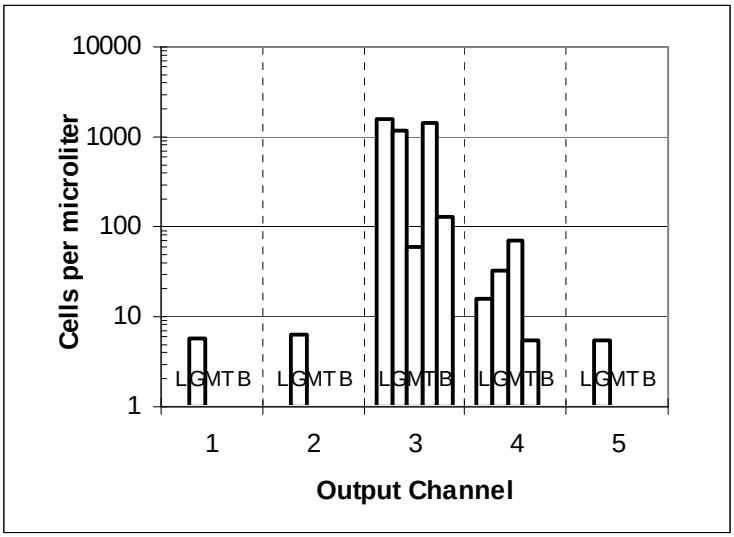

Figure 5-11: Flow cytometry measurement of the concentration of white blood cells in each exit channel of the version A device. Lymphocyte (L), Granulocyte (G), Monocyte (M), T Cell (T) and B Cell (B) concentrations are shown. 99% of white blood cells are displaced into channels 3 and 4.

them to be on average larger than 4.5 micron[12, 13], which agrees with our results. It is also well known that resting lymphocytes are smaller than monocytes by SEM and flow cytometry[12, 13]. For lymphocytes and monocytes, the ratios of cells in channel 3 to cells in channel 4 were 100 to 1 and 1 to 1, respectively. The smaller lymphocytes, on average, were displaced significantly less than the larger monocytes. Most of the lymphocytes behaved like hard spheres of size smaller than 7 micron, whereas half of the monocytes were displaced below the 7 micron threshold and the other half above the threshold.

The analysis of granulocytes prevents me from claiming 100% deflection of all white cells out of main stream. A concentration of 12 granulocytes per microliter per channel was calculated from flow cytometry for channel 1 (versus 1,192 and 37 for channels 3 and 4 respectively). This result limits the claim to 99% of granulocytes and 99.6% of all white blood cells being displaced in channels 3 and 4. Because of the well known tendency of granulocytes to produce a wide range of forward and side scattering intensities, background counts may be incorrectly identified as granulocytes, especially because there is no definitive marker for granulocytes. Additionally, granulocytes may be more like red blood cells because they have equivalent density, in that unlike lymphocytes and monocytes they are separated at a different density by centrifugation[13].

The second flow cytometric analysis was designed to measure the number of red blood cells in each output channel. All cells producing forward and side scatter in the flow cytometry plots were counted as potential cells (except the Trucount beads) and the expected white blood cell concentration in each channel (based on the lysed blood values) were subtracted to give a raw red blood cell count for each channel. The total results for all five channels are calculated and the concentrations are displayed in figure

5-12. A total of 3 x 10^6 red cells were detected, with 99% of the cells in channels 1 and 2. A flow cytometry analysis of the running buffer (with Trucount beads added) without blood gave a background concentration of 2,000 particles per microliter within the forward and side scatter area used for flow cytometry analysis of white and red blood cells. Thus, the concentration of red blood cells in channels 4 and 5 (raw signal of less then 1,900 particles per microliter) is not significant and is probably due to background (debris and electronic noise).

There were a statistically significant number of red blood cells in channel 3 (26,000 cells per microliter or 0.9% of the total red cell count), which act as hard sphere particles of size 4.5 – 7 micron. Because of the unique shape and deformability of the red blood cells, red blood cells do not always behave as if they have a clear hard sphere threshold. This will be discussed further in subchapter 6.1. Nevertheless, an enrichment of the

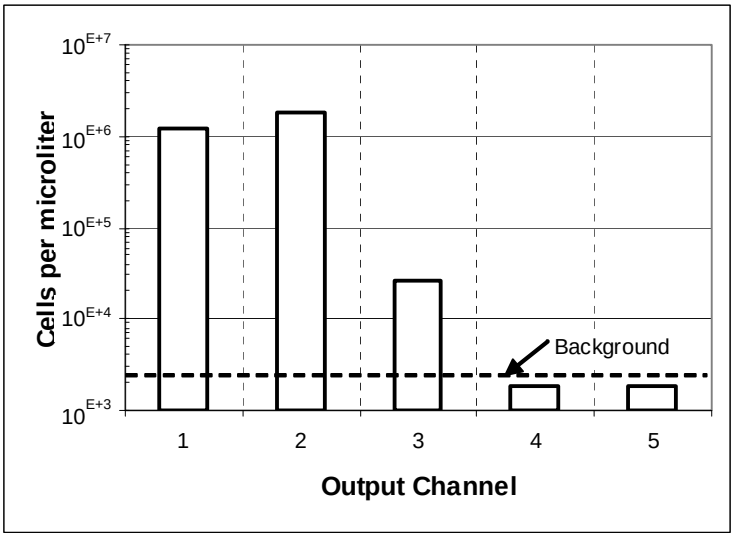

Figure 5-12: Flow cytometry measurement of the concentration of red blood cells within a version A device. Background concentration of just Trucount beads is displayed.

white to red blood cell ratio of over 110-fold from that of the initial blood specimen was obtained from channels 3 and 4 of our microfluidic device.

5.3 Cascade Device

The final group of experiments was conducted in a cascade device. As discussed in section 3.2.3, the cascade device allows the removal of large particles separated from the main flow in early stages, so that they do not enter into later sections with smaller gaps, and clog the device. This allows for a much higher dynamic range. The device here is a closed or single entrance device. Results of some bead separations are presented to verify the theory of the device, followed by a discussion of some basic blood separations.

5.3.1 Design and Bead Results

The cascade design consisted of three major regions, each with its own exit section. The design is presented in table 3-6 with the design curve in figure 3-6. The first two regions each consist of a single array, with gaps of 16 and 8 micron, designed to separate 7 and 3.3 micron particles. Each of these sections had a set of exit channels, balanced to maintain vertical flow. The final region consisted of two successive arrays of size 4 and 2 micron. The thresholds were designed to give a large DR of 20 for this device, as well as target the separation of the principle blood components. It was an analytical device to evaluate the addition of the cascade exits on a smaller scale.

The device was first tested with polystyrene beads. 200 nm, 2 micron and 8 micron fluorescent beads of different color (red, blue and green respectively) were chosen to showcase the important regions of activity for the device. The large 8 micron beads took

the path of the white blood cells, while the 2 micron and 200 nm beads followed the path of the red blood cells and plasma respectively. The image intensity of the fluorescent particles was collected from a single frame, and the results are shown in figure 5-13. The large green beads were observed to displace in the first region, and enter the first set of

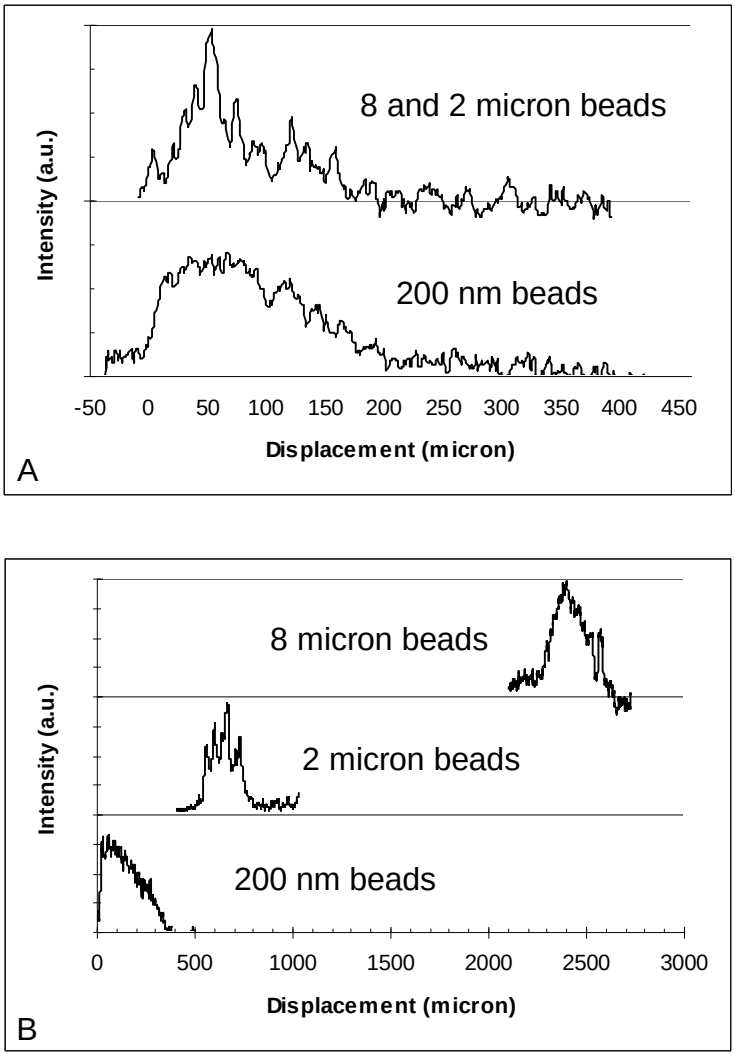

Figure 5-13: Histograms of Polystyrene beads versus lateral displacement. (A) is at the beginning of the first region of the device, and (B) is at the end of three regions of the device. Each of the three sizes of beads were successfully separated.

exit wells. The blue 2 micron particles were observed to travel through the first two regions, and displace in the third region. Because of a slight under etch of the last region of posts (2 micron gap) the majority of 2 micron particles got stuck at this interface. About 10% of the 2 micron beads continued into the final section and displaced within this region. The 200 nm red particles, below the threshold of all regions in the device, were observed to travel straight through the device, with some diffusional broadening.

5.3.2 Blood Results

The device was loaded with whole blood stained with Hoechst as described in the methods. The white blood cells were observed to begin being displaced immediately in the first region, which has a threshold of 7 micron. These cells were displaced the full 2500 micron and exited through the first set of exit channels.

Some red blood cells were observed to have a small displacement in all regions of the device. This occurred even though the region with largest critical diameter of 7.0 micron. The prominent results for the red cells are shown in figure 5-14. After the first region of threshold 7 micron, a tail of red blood cells was observed from the small percentage of displacement occurring. As will be discussed again in section 6.1, the effect was reduced with an increase in speed. A larger percentage of red blood cells were observed to begin displacing in the second section, with a wider distribution. A number of cells were observed to enter the exit channels at the end of this region. These cells are not displayed in the figure because their intensity was on the order of the intensity of the posts (noise of the image). All of the observed red blood cells began bumping in the third region with a 1.5 threshold. These cells continued to be displaced in the fourth region, as a large percentage (seen as a spike at 1000 micron in figure 5-14) and were observed to be

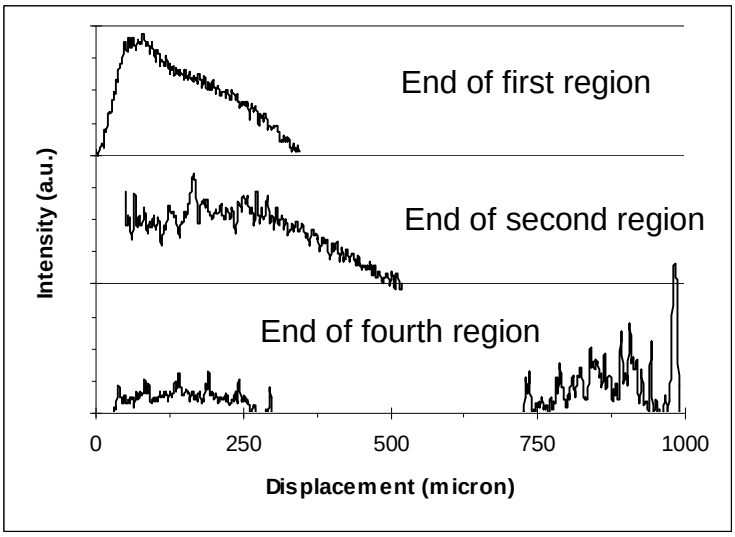

Figure 5-14: Histogram of red blood cell density versus lateral position measured at three points through the cascade device. A tail of displacing cells is observed in the first region, which increases in the second region. At the end of the device red blood cells are only observed on the far right. Spikes in the data on the bottom left are an artifact of the 50 micron wide exit channels.

leaving the device at the right wall of this final exit region. This displacement against the right wall was because of the unexpected displacement of the red blood cells in the first two regions. No red blood cells were observed optically in the straight region at the final exit. (0 to 250 micron in figure 5-14) The spikes in the fluorescent image are artifacts from the sides of the exit channels (they are every 50 micron).

By combining the results of these two experiments, it has been shown that observed red blood cells and particles above 2 micron have been separated from the straight stream, which is represented by the 200 nm particles. If the cascade device is to be further explored, an antibody for platelets should be mixed with tiny beads to mark the location of both platelets and plasma independently in the same experiment. Additionally flow cytometry should be used to verify the observed results.

Both the bead and blood experiments were complicated by clogging of the closed side cascade channels. The long narrow channels needed to balance the fluidic resistance were easily blocked if an aggregate or even a single cell became lodged within the channel. A single channel clogged would then disrupt the functionality of the device by altering the fluidic resistance.

The open entrance cascade device has been shown to be a superior design to the closed single entrance design when the results herein are compared to the results of Inglis[55]. Results from an open entrance device used to separate plasma from all cell components larger then a micron were shown in Davis *et al.*[46]. Therefore white and red cells were successfully separated from plasma in both devices. The closed design shows that it is much more susceptible to clogging. The very long narrow channels needed only a single obstacle to impede flow within the entire channel and stop the fractional capabilities of the device. This greatly decreased the functional time period of the device, and therefore its usefulness compared to an open design. In the future, a combination of the two designs might work best. A larger region than the closed design should be open to allow for the collection of cells. Then a closed, but serpentine region to follow will have the advantages of both types. From the open design, it will not clog easily because the serpentine region will have multiple wider paths and from the close design, since it is closed off from the post array, it will not continue to effect the streamlines as much in that region (as seen in figure 3-8).

In summary, a cascade device was constructed and successfully used to separate beads and blood cells. The cascade device demonstrates a method for significantly increasing the dynamic range with a complete removal of a flow stream.

5.4 Viability and Cell Interactions

Two additional effects, particular to biological samples were considered during the development of this thesis. Viability of the white blood cells was tested in a single experiment. This would be an area where a great deal of more experimentation is possible to expand the possible applications of the DLD device for blood. This section will also discuss some of the applications of running high density samples.

5.4.1 White Cell Viability

A single experiment was conducted to gauge the level of cell death of white blood cells which traveled through a DLD device. Flow cytometry allowed the study of cell viability. A blood run as described in chapter 4 was conducted in a chirped version B device. The content of each output well was collected, and stained with CD45 for white blood cell identification. Propidium iodide (PI) was added to check for viability. PI is a nuclear stain which is membrane impermeable to live cells. It penetrates damaged or dead cells. The mixture was placed into a Trucount tube so the exact measurement of cell concentration was possible. Two devices were prepared, one with the F108 treatment, and one without. F108 is the surfactant used to ease loading of the device, and there was concern it might affect cell viability. Two controls of blood not sent through the device were prepared, with and without F108. This experiment was conducted in Princeton, with the flow cytometry about 15 hours later at the Wadsworth Center in Albany. The results are shown in figure 6-12. The first important observation was the effects of surfactant F108 on the cell viability. There was not an appreciable increase in death due to F108 (an increase of, at most, 2%). Secondly, the device was found to increase the amount of cell death by about 6 to 8%. The high cell death in the control of

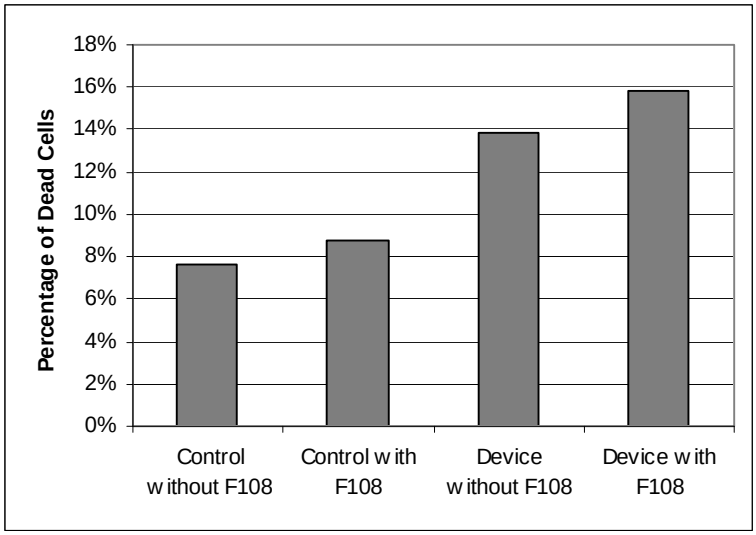

Figure 5-15: Percentage of dead cells found with PI and flow cytometry. Device runs were conducted about 30 minutes after blood was drawn, and flow cytometry was done approximately 15 hours after blood was drawn.

about 7% is attributed to lengthy time between blood removal and testing. Nevertheless, this experiment yielded over 84% viable white blood cells, even with the F108 treatment.

5.4.2 Cell Interactions

A final second-order issue is the cell-cell interactions and hydrodynamic interactions at high cell densities. Ideally, the device would be run at low enough cell concentrations so that interactions between the individual cells as they travel through the array are not important. However, this is impractical when working with whole blood and high blood processing rates. Cell-cell hydrodynamic interactions is a complex subject since there is no perturbative approach[62]. There are two main effects: hydrodynamic coupling of the cells to each other which can entrap a small cell in a larger cell's flow field and prevent separation of the small one from the large one[62], and entropic effects where larger cells

are moved by depletion forces to the outside of a channel[36]. These effects might be an explanation for the deviations of the blood cells from an ideal separation. Since I cannot conclusively identify the importance of these interactions, in the experiments within this thesis where it is not necessary to run whole blood I used diluted blood to mitigate the possible effects.

6 The Effects of Non-Rigid and Non-Spherical Properties of Cells

The majority of the information presented so far has ignored two major properties of blood cells. First, they are not rigid and are able to deform, if forces are applied to them. Thus their apparent size seems to change with different average velocity within the array. Second, some cells are not spherical, thus orientation of the cell will affect its path through the device. This chapter will focus on observed affects which can be attributed to these biological aspects of the blood cells. The first two subchapters will discuss observed velocity dependence of both red (6.1) and white (6.2) blood cells, and offer an explanation. Subchapter 6.3 will present two models for measuring the deformation of cells and compare them to other studies of cell deformation.

6.1 Effect of Fluid Velocity on Red Blood Cell Displacement

The lateral displacement and thus apparent size of both red and white blood cells in a microfluidic DLD device has been observed to change as a function of the fluid velocity through the device. This is in contrast to rigid polystyrene spheres, where apparent size was observed to be independent of speed. This section will summarize the results observed of red blood cells and discuss some possible explanations.

6.1.1 Non-Displaced Red Blood Cells

The dependence of final displacement of red blood cells on velocity was first observed in a multiple array device, as described in section 3.2.1. Section 5.1.3 described the results where red blood cells were separated from plasma. As the pressure was

increased to increase the velocity, the angle of separation between the center of the red blood cell stream and the plasma stream was found to decrease, as shown in figure 6-1. Above a peak velocity of 1250 micron per second within this device, the red blood cells and the plasma no longer separated because the red blood cells were no longer displacing. The location of the red blood cells was compared to the final location of the path of the dye, which had zero displacement due to the small size of the dye molecule.

Red blood cells have different shapes along different axis. The red blood cells are able to rotate, and possibly deform as they pass through narrow openings. As the velocity is increased, stronger forces on the red blood cell could deform it or rotate it so it aligns its long axis with fluid flow. Either of these changes would allow the red blood

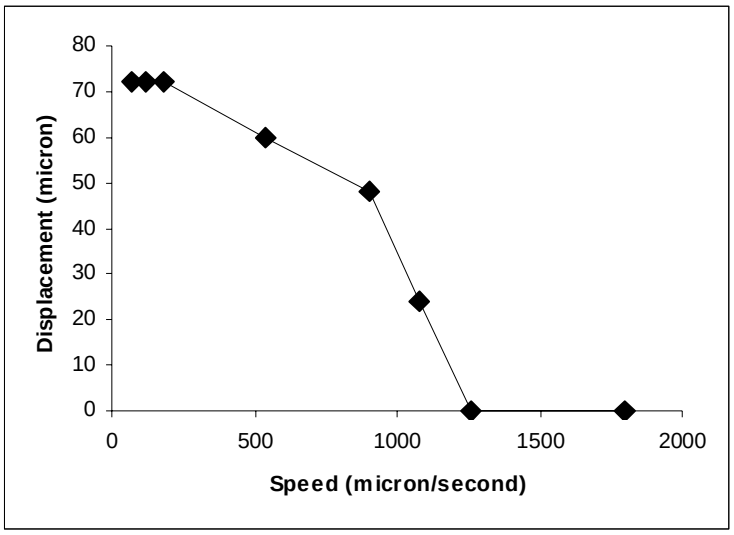

Figure 6-1: The fluid speed versus the average red blood cell displacement: The device consists of a 2.5 micron gap and a shift fraction of 0.1 for a critical size of 1.2 micron for rigid spherical particles. The average position of the red blood cells is measured relative to the location of a background dye. As the speed increases the red blood cells stop being displaced and travel straight through the array.

cells to “fit” into the width of the first streamline, and no longer displace within the device. This hypothesis would explain the dependence of the separation angle on fluid velocity.

6.1.2 Displaced Red Blood Cells

In the previous section, I discussed red blood cells which were expected to laterally displace but did not because of effects related to high fluid velocity. Experiments with the hemocytometer in section 4.4.2 showed additionally, red blood cells displacing in a device in which red blood cells are not expected to separate, i.e. a device designed to displace only large white blood cells. Therefore, an experiment was conducted to see the fluid velocity dependence of this effect.

Three individual experiments were conducted in chirped B devices, at three different speeds, 1000, 2000, and 4000 micron per second. While this device is designed for white blood cell fractionation, I wanted to analyze the small percentage of red blood cells which were observed to displace into regions with a hard sphere threshold of as high as 7 micron. The device consisted of 5 output channels, where all particles smaller than 3 micron were expect to travel straight into channel 1 (as shown in figure 5-7).

Flow cytometry was performed on the cells removed from each of the five exit wells of the device. The concentration of red blood cells was measured at three different applied pressures in each of the five exit wells, with the results shown in figure 6-2. The concentration of red blood cells which are not laterally displaced into channel 2 or greater increased from 99.32% to 99.92% of the total cells measured as the fluid velocity is increased from 1000 to 4000 micron/sec. The concentration of red blood cells in the second channel decreased by a factor of 4, as the velocity was doubled from 1000 to 2000

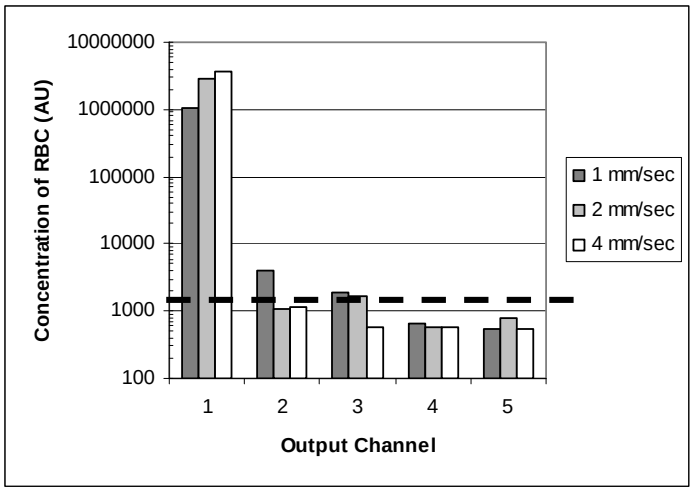

Figure 6-2: Concentration of red blood cells measured in the outlet wells of a chirped version B device with flow cytometry at different speeds. Concentration of displaced red blood cells decreases at higher speeds.

micron/sec. As with the previous section, it is unclear what the exact cause for this effect, with red blood cell deformation, orientation and rotation to be considered in future work.

6.1.3 Red Blood Cell Rotation

The rotation of non-spherical objects as they move through the arrays and/or distortion of deformable shapes due to shear is a complex subject. The shearing torques τ are due to the local curl $\nabla \times \vec{v}$ of the vector velocity field $\vec{v}(x, y, z)$ near surfaces, and the net force fields $\sum F$ are due to high pressure gradients ∇P as the fluid is forced through the gap G. These shearing torques and hydrostatic force fields can not only rotate and deform the cells, but in principle can lyse the cell if the shearing torques and hydrostatic pressure gradients become too high. The spatial dependence of $\vec{v}(x, y, z)$ can be computed in a straightforward way since the fluid flow is laminar, but unfortunately the

calculation of the shear fields and hydrostatic forces acting on non-spherical objects is quite difficult because large objects disturb the flow fields substantially. The hydrostatic pressure gradients in our device are actually quite small even at the pressures needed to move blood at 1000 micron/sec through the devices discussed. Indeed no obvious cell lysis occurs, although this must be checked more carefully. The rotation and distortion of compliant objects in the complex vector flow fields is a more serious issue that can change the effective critical diameter D_C. For example, a red blood cell has a large diameter of 8 microns but is only 2 micron thick, so if there is a preferential orientation of the cell in the gap flow pattern at high speeds there will be a dramatic change in the lateral displacement of the red blood cells. Another possibility is that the shear fields at high flows can deform the red blood cell into a sausage shape[59]. Further work is needed to determine if significant rotation or alignment of red blood cells is occurring.

6.2 Effect of Fluid Velocity on White Blood Cell Displacement

Because of the observed velocity dependence on the position of red blood cells, velocity dependence of white blood cells was also explored. Cells are significantly softer then polystyrene beads, and therefore are expected to deform within the DLD device. White blood cells are spherical so deformation, and not rotation is expected to be the primary effect. Two distinct groups of experiments were conducted to better understand these observations. One set of experiments targeted individual cells and tracked their path through the entire array. In order to do this tracking, the cells were traveling at slow velocity (10 micron per second). A second set was conducted at high velocity (greater than 1 mm per second), and average values for a larger population of cells were analyzed.

6.2.1 Single-Cell Low-Velocity Measurements

In order to better understand white blood cell dynamics within the DLD, a set of experiments was conducted at slow velocities, less than 10 micron/sec. For a particular experiment, individual white blood cells were tracked from the entrance to the exit of a chirped version A device. The slow velocity was necessary in order to maintain the cell within the microscope's field of view, as the cell traveled the entire length of the device. For each cell, the separation angle was measured in each of the 13 regions within the device. The previous bifurcation arguments state a particle should displace at the separation angle θ_S if above the critical size or at the zero angle keeping within the fluid stream if below the critical size.

At these slow speeds, cells were observed at non-ideal separation angles, that is angles between zero and θ_S. The total number of regions in which the separation angle was non-ideal gives a value for the change in size possible with in the device. If the separation angle was non-ideal for a single region, the particle size could be near the critical diameter for that region. For example, a 5 micron polystyrene bead within a region with a critical threshold of 5 micron has been observed to have a non-ideal separation angle ($\neq 0$ or θ_S). However, if this non-ideal behavior continues into a second region for same single particle, the particle would be acting at different times as if it has a different effective size. The number of regions over which particles were observed to have non ideal behavior ($0 < \theta < \theta_S$) is a measure of the extent of cell deformity over time within the array. A histogram of the number of regions over which the particles performed non-ideally is shown in figure 6-3.

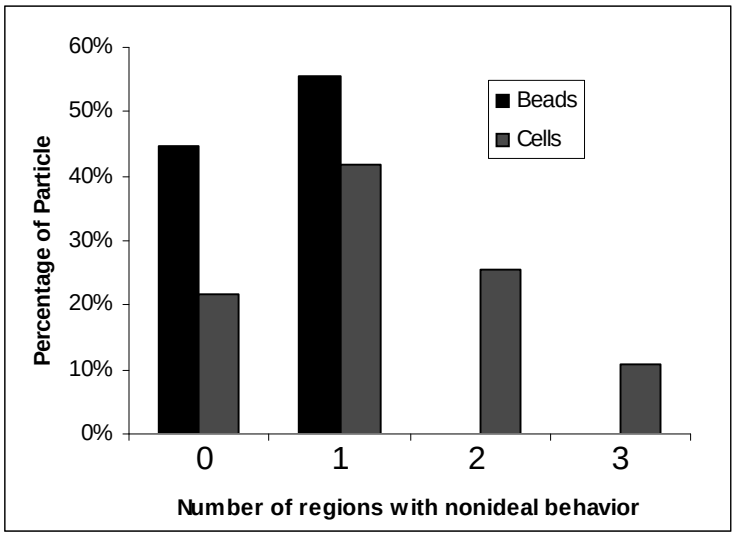

Figure 6-3: Comparison of the variation in beads and cells within a microfluidic DLD device. While a homogeneous bead solution can show a non-ideal separation angle for a single region, cells show variance in size over two or three regions.

Polystyrene beads are significantly more rigid then cells. In both this experiment and in high speed measurements of section 6.2.2, beads were observed to have non-deformable behavior. In this case, non-deformable beads can have at most non-ideal behavior over one region, if they are close in size to the critical threshold. White blood cells exhibited non-ideal behavior over a larger range. While this result was attributed to deformability, the cells and beads also differ in density, electrostatic interactions and surface chemistry. Thus the behavior of even spherical cells in a DLD array is complex. This dynamic behavior would be a good subject for future study.

6.2.2 Average High-Speed Measurements

A typical white blood cell run was conducted with a single chirped B device. The lateral displacement of over 200 white blood cells was measured at each of seven

different applied pressures at the output of the array, 4.5 cm after the injection point at the top of the array. The cells were videotaped at this position so both the velocity and position could be calculated. The velocity of 15 different cells was measured at each pressure and averaged to compute the average velocity of the white blood cells. The average position of the 200 cells was calculated for each pressure. This data is shown in figure 6-4. The average velocity ranged from 500 micron/sec to 6000 micron/sec.

The experiment was repeated with polystyrene beads at four different applied pressures within the same device design, as a control experiment, also shown in figure 6-4. As stated in the previous section, the polystyrene beads are significantly more rigid than cells. The assumed non-deformability of beads within this particular device was confirmed by the observed independence of speed.

As the speed increases, the effective diameter of the cell as it is measured by the DLD

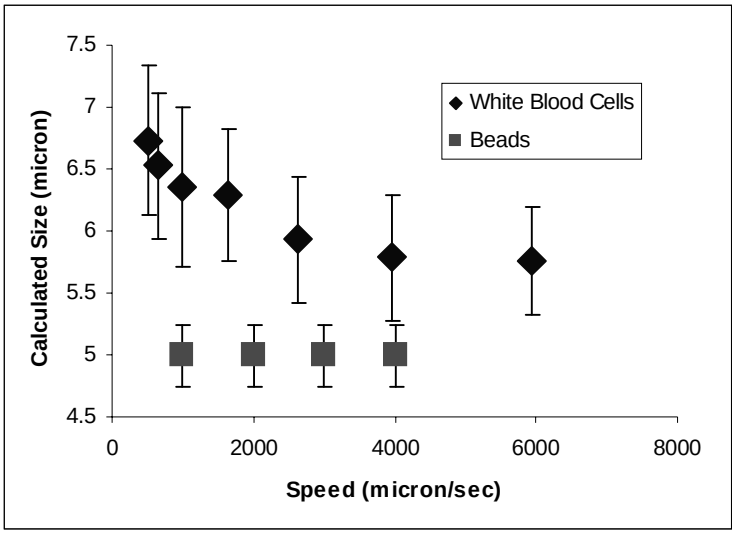

Figure 6-4: Change in effective size of white blood cells compared to polystyrene beads, as function of velocity.

decreases. Unlike red blood cells, white blood cells are spherical, so rotational effects are assumed to be negligible, but like red blood cells the white blood cells are able to deform. As the velocity increases, higher forces are applied to the cells, and larger deformations occur. These deformations enable the cell to have an effective smaller size in the DLD array. In the next section, two models are developed to quantify this deformation and compare it to other existing force deformation studies.

6.3 Model of Cell Deformation

A change in the average apparent size of white blood cells within a DLD device because of an increase in velocity has been observed. A model was developed which will quantify the effect, and compare it to other methods of measuring deformation. Because of the spherical shape of the white blood cells compared to the biconical disk shape of the red blood cells, analysis will focus on the white blood cells. This observed change in size because of the forces the cell experienced in the array was quantified, and compared to the observed changes in 'effective' cell size with existing data with models of cell deformability.

6.3.1 Deformation Model Background

An important part of blood cell function is the ability to deform and fit through capillaries. As small as 3 micron in diameter, the capillaries are able to carry much larger cells without clogging every second of every day. These large deformations, as well as the small ones observed within the DLD device are important to understanding device functionality; this can lead to a more fundamental understanding of cellular function and application. In particular, white blood cell deformation has been studied and measured

by a number of different techniques. Cells were deformed by being sucked into a glass pipette[64] and measuring the deformation as a function of time and force. A number of models have been developed based on these measurements. Since then, a number of other techniques for deforming and measuring the cells have been used. White blood cells have been forced against stationary beads and the area of contact measured[65], and AFM tips have been used to measure deformation by tapping a cell[66]. Again simple models such as an elastic model and cortical tension model have been used with these experiments to get a basic understanding of the deformation. Additionally, much more complex and in depth models were constructed by the Tran-Son-Tay group[67, 68].

The hypothesis herein is the interaction of a soft (deformable) cell with the post gives rise to the lateral displacement, deforms the cell so it acts smaller than its undisturbed size. An example of this is shown in figure 6-5. Further, because of the hydrostatically driven flow and the no slip condition at the obstacles, a parabolic flow profile is created. This creates a shear force on the cells as they pass through each gap, from the profile across the gap. The deformed cell itself can rotate under these forces, so that it presents its small axis perpendicular to the streamline in the critical gap region, or it stays in closer contact with the post. Thus it will behave in the array as a particle with a diameter smaller than that of an undisturbed cell.

6.3.2 Applied Forces on Cells in an Array

Consider the possible deformation of a cell impinging directly on a post. To calculate the deformation of a cell, one needs to know the forces on a cell and the deformability of a cell. To determine the forces, consider a cell which has run into a post and is instantaneously stopped by it. Figure 6-6 shows a velocity profile of two rows within a

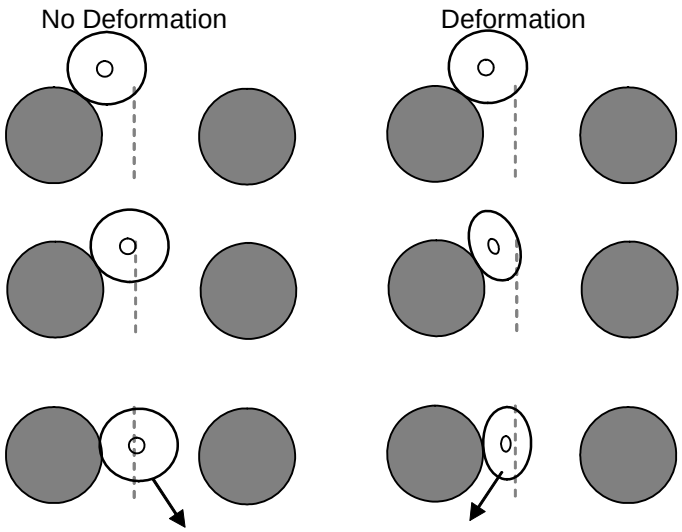

Figure 6-5: A series of consecutive schematics of cell deformation while interacting with a post within the DLD device. The left series shows a non-deforming cell larger then the critical size. The cell transitions over time through a gap and displaces because of the asymmetry in the fluid flow around the post. The right series shows a same size deforming cell through the same gap at the same three time instances. As the cell interacts with a post, forces cause a decrease in the effective size; hence, the cell is able to fit into the first streamline, and no longer laterally displace because of the post.

device, with a single cell located next to the post. Assuming the cell has stopped at this position, the cell is significantly slowed next to the post. For this simulation a pressure of 5 Pa was used over the two rows which gave a peak flow velocity at the center of the gap of 0.5 mm/sec.

A 2-D finite element analysis (Femlab, Comsol Inc. Burlington, MA) simulation was used to calculate the forces on a cell as a function of the average flow speed. The 2-D simulation assumes the post and cell are infinite cylinders and gives forces per unit depth. To get an estimate on the forces on a cell, these values were multiplied by the cell diameter. The average fluid velocity was determined from the velocity field.

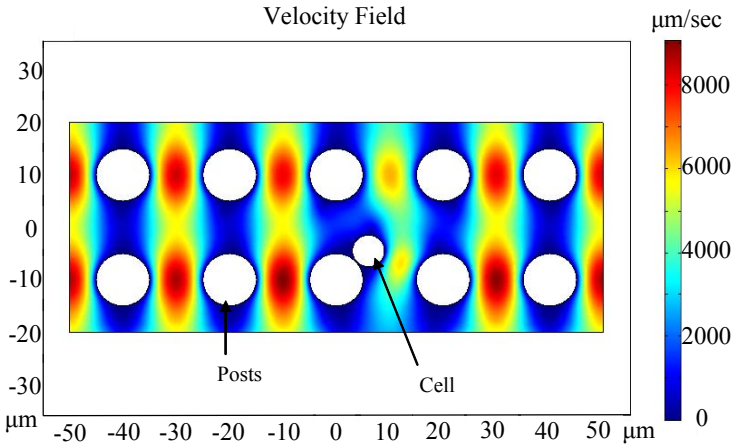

Figure 6-6: Finite element analysis of the velocity profile with a cell stopped next to the center post.

Conceptually, a cell was placed and held in position where it will impinge onto a post, while fluid was allowed to flow around it. The vector forces on the cell surface were then summed to obtain a total net force applied to the cell at a particular peak velocity. For example, with a 2 mm/sec peak velocity, a total net force of 47 pN/µm was calculated.

This was done for several applied pressures, and since the flow models were linear, a force on the average diameter cell (6.7 microns) was found to vary linearly with peak velocity v.

$$F = \frac{0.139\text{pN} \bullet \text{s}}{\mu\text{m}} v \qquad (6\text{-}1)$$

because 0.139 pN*s/micron is the slope of the force versus velocity relationship, for the average cell size of 6.7 micron. This force calculation was used within the two models to estimate the cell deformation.

6.3.3 Elastic Model

Two existing models have been used to relate the amount of deformation measured compared to an existing applied force. The elastic, or Hertz model, was described in detail by Landau and Liftshitz[69]. It is used to model two elastic spheres in contact, in a static situation. One sphere represents the cell (deformable) and the second incompressible sphere represents the post. Since the post is a cylinder and the cells are spherical, this is a first order approximation and only looks at a single two dimensional slice of the problem. An isotropic, incompressible medium was assumed. For sphere – sphere interaction

$$\delta = \left(\frac{3}{4} \frac{\left(1 - \nu^2\right) F}{E R_C^{1/2}} \right)^{2/3} \qquad (6\text{-}2)$$

where F is the applied force, E is the modulus of elasticity, ν is Poison ratio (assumed to be 0.5), R_C is the radius of the cell and δ is the change in radius of the cell. For example, a cell of 6 micron would change by 0.4 micron from a force of 210 pN, and an E of 140 Pa (corresponding to a peak velocity of ~1.5 mm/sec).

For each flow speed in figure 6-4, the assumed reduction in cell size was the same as the cellular deformation delta of equation 6-2. Using the force on the cell at a particular velocity (equation 6-1), the modulus of elasticity E of the cell was estimated. A baseline average size of 6.7 micron was assumed, from the slowest velocity measured (0.5 mm/s). For example, at a peak velocity of 1.2 mm/sec, the average size has decreased to 6.3 micron, a change of 0.4 micron, and combining this with an estimated force from equation 6-1, one finds a modulus of elasticity (E) of 120 Pa, shown in figure 6-7. The data shown is for velocities from 0.65 mm/sec to 4 mm/sec which corresponds to

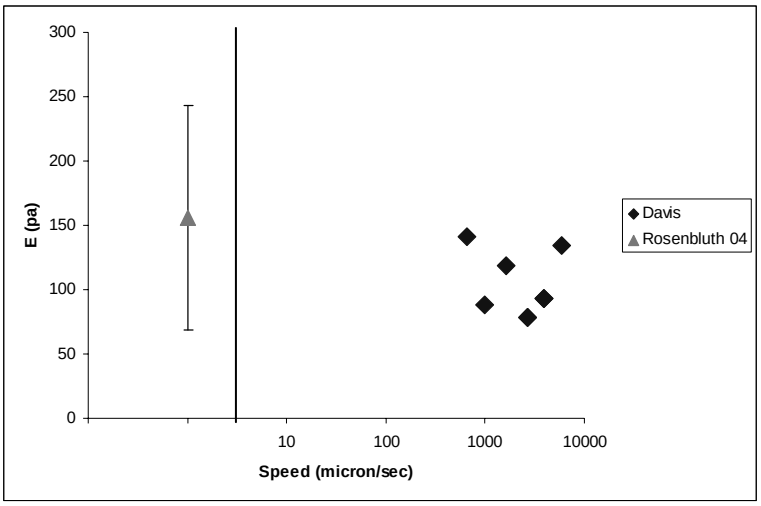

Figure 6-7: Calculated values of modulus of elasticity for our experiment at different speeds compared to existing literature.

deformations of 0.2 micron to 1 micron. The elasticity varies from 80 to 150 Pa. In comparison, Rosenbluth *et al* [66] calculated an average modulus of elasticity of 156 Pa for cells from an AFM experiment with much slower deformations (also shown in figure 6-7). Despite the great difference in velocities, and the crude nature of some approximations, the results are comparable. This shows that this model may be appropriate.

6.3.4 Cortical Tension Model

The second model for the deformation of cells when they hit a barrier assumes a cortical tension exists around a viscous liquid drop, and no intrinsic elasticity to the fluid within the cell. This model has been used extensively on neutrophils, a type of white blood cell[65]. It assumes a homogeneous viscous liquid, surrounded by a shell with a

particular uniform constant cortical (surface) tension. Following the approach of Lomakina *et al.*[65], from the Young-Laplace Equation

$$\Delta P = T_C \frac{dA}{dV} \qquad (6\text{-}3)$$

where ΔP is the change in pressure along the deforming surface, T_C is the cortical tension, and dA/dV is the change in cell area with respect to the change in cell volume. For our geometry (figure 6-8),

$$P = 2\,T_C\left(\frac{1}{R_P} + \frac{1}{R_C}\right) \qquad (6\text{-}4)$$

and

$$P = {}^{F}\!\!\diagup\!\!_{2\pi\,R_C\delta_C} \qquad (6\text{-}5)$$

where R_P is the post radius, R_C is the cell radius δ_C is the change in cell radius, and F is the applied force. By assuming the cell surface area does not stretch during the deformation

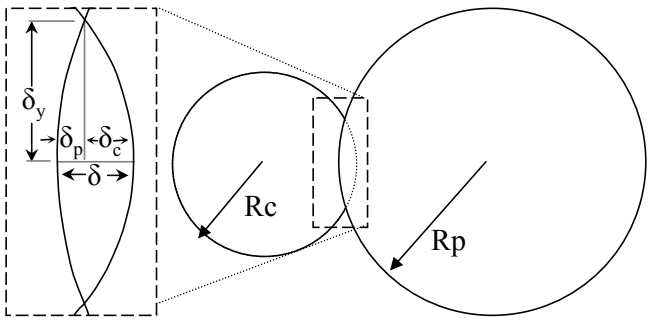

Figure 6-8: A diagram showing the important dimensions to be discussed in the cortical tension model to show white blood cell deformation at a post.

$$2\pi R_C \delta_C = 2\pi R_P \delta_P , \qquad (6\text{-}6)$$

one finds

$$T_C = \frac{F}{4\pi\left(\frac{1}{R_P}+\frac{1}{R_C}\right)\left\{R_C\left[\frac{\delta}{\left(1+R_C/R_P\right)}\right]\right\}} . \qquad (6\text{-}7)$$

Note this model predicts a deformation which is linear with the velocity (force), versus the elastic model which predicts a power to the two thirds relationship.

A similar approach as with the elastic model was used with the data to extract the effective cortical tension T_C. For example, the data measured a change of 0.4 micron for an average cell size of 6.7 micron at a velocity of 1.2 mm/sec. One finds a force on the cell of 167 pN and a cortical tension of 40 pN/micron. The values of cortical tension for the different measured velocities are shown in figure 6-9, along with data collected from other experiments in literature[64, 65, 66, 70, 71].

6.3.5 Model Comparison

Using the adjustable parameter of modulus of elasticity or cortical tension, both the elastic and cortical tension equations can be used to model the change in white blood cell size at increasing forces from increasing velocities. They are summarized in figure 6-10, using an E of 140 Pa and a cortical tension of 35 pN/um. The models predict different shapes of dependencies on speed, but within the available data it can not be discerned between the two. These two models give plausible explanations of the observed data.

Additionally, two lymphatic cell types were measured for velocity dependence, Jurkats and HL60. The elastic model was used to allow for comparison with the study by

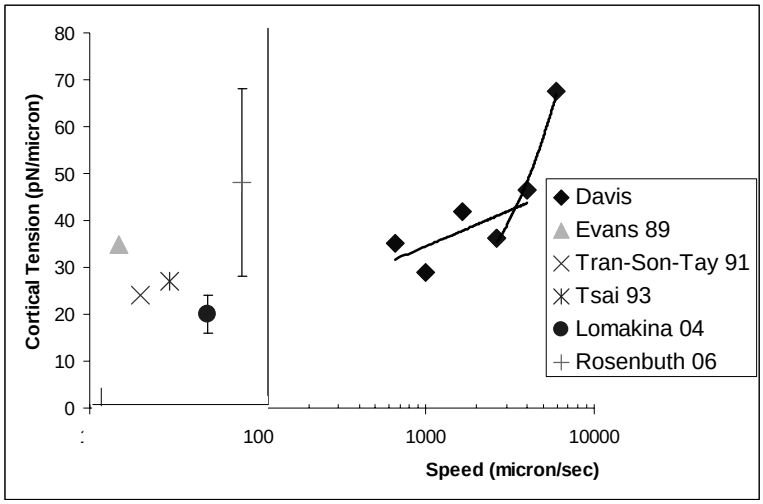

Figure 6-9: The calculated values of cortical tension for our measured data which is compared to the existing values from literature.

Rosenbluth *et al*[66] on similar cells. Both leukemia cells were found to be more stiff than normal cells, as shown figure 6-11. At a velocity of 2 mm/sec, the Jurkats have an average effective modulus of elasticity of 237 Pa (versus 109 Pa for normal lymphocytes), and the HL 60 the elasticity was found to be 357 Pa. This trend of their being stiffer than normal cells is consistent with Rosenbluth *et al*[66] who states HL 60 cells are significantly stiffer than normal cells (855 ± 670 Pa compared to 156 Pa for normal cells).

6.3.6 Time Scale Analysis

Any sort of deformation from interaction with the post, will eventually reform after the cell moves away from the post. This analysis consists of only a collection of the 'steady state' data where an average effect is measured, rather then looking at individual cells before, during and after post interaction. Therefore, there is no transient data. Other

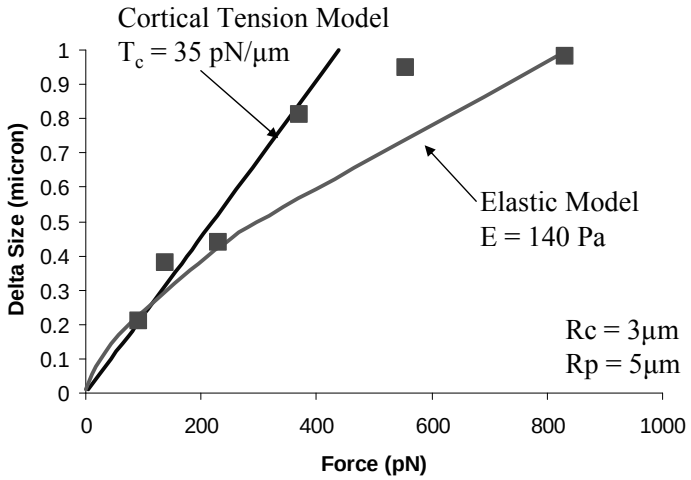

Figure 6-10: The extracted cortical tension (35pN/micron) and Elasticity (140 Pa) compared to the measured data.

experiments[64, 70] which measure a T_C also measure a cell viscosity (μ), in order to complete the cortical tension model. Using a value of viscosity of 200 poise[70] to calculate a first order approximation of the relaxation time:

$$t = \mu R / T_C \qquad (6\text{-}8)$$

which gives a value of t on the order of magnitude of about 20 seconds. A typical run was at speeds much faster then 100 micron/sec, so the transit time between posts is at most 0.2 seconds. With over two orders of magnitude difference in the time scales between transit time and relaxation time, the calculation supports our steady state assumption for the model. The cell will deform in the beginning of the device, and remained deformed as it passes, and it displaced at each row of the DLD.

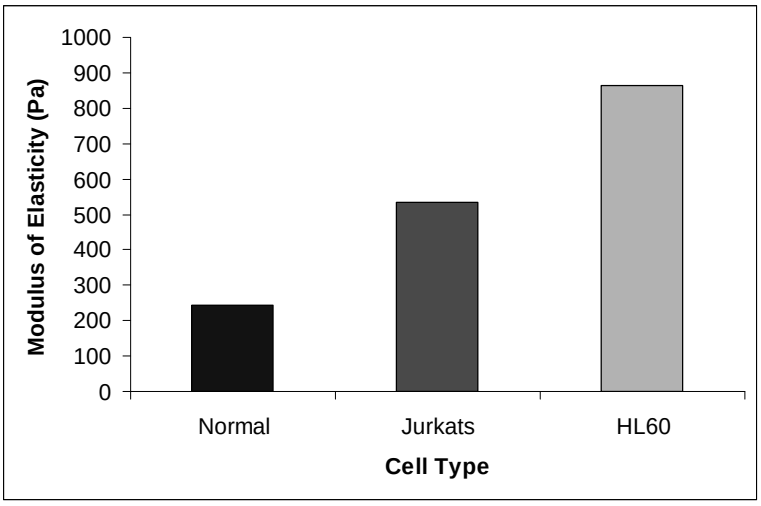

Figure 6-11: The modulus of elasticity measured by the DLD for two different leukemia cells compared to healthy white blood cells.

7 Degradation of DLD Performance due to Diffusion

In the course of the previous experiments a number of deviations from the ideal step function bifrugication have been observed. The DLD array concept does not rely on diffusion and random process as do some other separation technologies. However if particles diffuse between streamlines, the performance will be degraded. For example some large particles may not laterally displace when they are supposed to, if they diffuse out of that first streamline. Additionally, the path of small particles will spread out from their original streamline path over the course of a device.

This chapter will focus on taking diffusion into account in both theory and simulation. Some of the non-idealities will be explained and modeled, and will conclude with some general observations.

7.1 Diffusion

Some mention has been given to thermal motion within the fluid of these devices, and its impact on some of the results. This thermal motion of particles was observed by Fick, and is described as the motion of particles to minimize a concentration gradient. Particles will spread out much like a perfume spreads out over a room. These particles are said to diffuse, where Fick's second law describes this phenomena,

$$\partial\phi/\partial t = D_{dif}\nabla^2\phi \qquad (7\text{-}1)$$

where D_{dif} is known as the diffusion constant, and φ is the concentration. The Stokes Einstein relation states,

$$D_{dif} = \frac{k_B T}{3\pi\mu D_P} \qquad (7\text{-}2)$$

for a given particle diameter D_P where k_BT is the thermal energy at temperature T. Smaller particles diffuse faster. From these relationships, the important effects of diffusion within a DLD device are characterized.

7.1.1 Peclet Number

The Peclet number is a dimensionless number similar to the Reynolds number, discussed in chapter 2. It is an evaluation of the transportation mechanism of the particles transported by the fluid within a device. It is the ratio between the advection and diffusion rates, which can also be written as

$$Pe = \frac{v\,L}{D_{dif}} \qquad (7\text{-}3)$$

where v is the local speed of the fluid (in our case, up to a few 1000 micron/sec), L is a characteristic length over which diffusion competes with advection fluid transport. In the case of a DLD, the concerned advection time is between posts, and is compared to the diffusion time between streamlines. D_{dif} is from equation 7-2 for particles in the flow which are separated from the flow streamlines in the bumping process. If Pe >1 the advection rate is larger than the diffusion rate between rows of posts and the flow is "deterministic" in that small particles are basically confined to streamlines and the DLD physics works. Analysis of typical Pe numbers for ranges of size and speed within the devices is informative.

Unlike the Reynolds number, the Pe is not absolute for a given blood flow velocity since it is a function of particle size. Also, there are two different size scales for diffusion in the device to consider: the local scale of the posts where diffusion moves particles out of the streamlines and ruins the deterministic bumping process, and the total array length

size scale β where diffusion broadens the lines of separated objects and ruins resolution even in the presence of successful bumping. First is the diffusion which occurs between streamlines, while traveling the distance of a row to row spacing λ. If the particle diffuses into a different streamline a distance ελ away its separation is compromised.

In the experiments herein, the minimum characteristic advection length is λ which is as small as 5 micron. The smallest particles desired to separate are blood platelets with radius of as small as 1 micron. With a slow average operational speed v of 1000 micron/sec, the Pe for platelets is on the order of 10^3 so we can safely ignore diffusion of all blood cells. Proteins (which are roughly 5 nm in radius) in the blood plasma will have a Pe of roughly 2. While they will not displace because they are under the critical size, the proteins will broaden in distribution as they move through the array.

This brings up the second scale that we need to look at: the overall diffusion of small particles laterally when traveling the complete length β of the device. This is particularly important for the analysis of proteins and ions within the plasma, since diffusional broadening may result in the loss of plasma proteins into the area where the cells are displaced. This broadening, b can be computed simply from

$$b = \sqrt{D_{dif} \beta / v} \ . \qquad (7\text{-}4)$$

The typical length of our complete device is about 4 cm, at the typical speed of 1000 micron/sec, a protein will diffuse a distance laterally of 100 micron, while ions will diffuse a distance of 1000 micron. This broadening sets a limit to the purity of the separated material.

7.2 Model of Diffusion Effects on the DLD Device

The deterministic lateral displacement effect does not rely on diffusion. However, particles in the fluid do diffuse, an effect that will be greater for small particles and slower flow rates. Therefore as devices are designed for smaller particle sizes, the effects of diffusion will be of greater concern and need to be accounted for within the design.

7.2.1 Model Development

Ideally within a DLD device, the particles below the critical size travel along the direction of the average fluid flow, and those above the critical size travel at an angle of θ_S, with an abrupt transition at the critical size. However, previous work at Princeton[45] has shown that at slow flow rates, the transition from $\theta=0$ to θ_S for increasing particle size is not abrupt. Two different types of degradation are observed in experiments, particles slightly above the threshold are observed to displace less then the ideal amount with a path of $\theta < \theta_S$, while particles slightly below the threshold are observed to displace from the straight trajectory with a path of $\theta > 0$. Figure 7-1 shows these previously published results[45] at two different flow speeds, along with the ideal abrupt transition. That the curves are more ideal at higher flow speeds suggests that lateral diffusion of the particles is the primary force in the degradation of the performance.

A simple qualitative model was developed to explore the effects of diffusion on particles in the array. The model computes the probability density function (pdf) of a single particle entering the device as a function of the lateral output location along the bottom of the device. The program takes as input parameters: the post size (P), the gap size (G), the number of rows until a repeat (N, which is equal to $1/\varepsilon$), the number of repeated sections (R, so N*R equals the total number of rows), the average fluid velocity

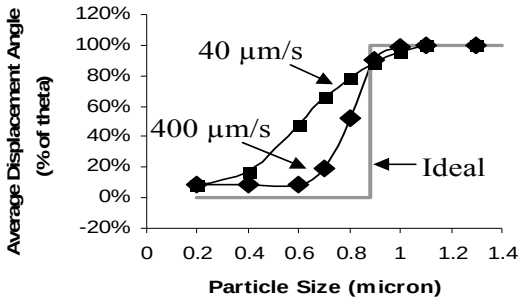

Figure 7-1: Reprint of data of displacement angle versus particle size for a single array device at two different speeds. The ideal performance of an abrupt change in the average displacement at 0.8 micron is dependent at low speeds.[45]

(V), a particle radius (r), and an initial probability density function at the input. Within each row of the device, the program determines the probability of an incoming particle in any streamline leaving the row in an adjacent streamline. The output information is fed into the next row as one moves down though the device. This approach allows us to simulate successive device regions that have different geometries.

A number of approximations are made. First, the obstacles will be modeled as squares. This allows the division of the device into two alternating, repeating regions (figure 7-2). The first region is called the unbounded region, and here, we assume the lateral diffusion of particles is unaffected by the obstacles. Lateral diffusion is allowed to occur freely between all streamlines in both directions. The second region, where the particles are located horizontally between the posts, we will call the bounded region. Diffusion in this region consists of two effects; diffusion out of the central streamlines will be similar to the unbounded region that is unaffected by the obstacles. While the two edge streamlines, those next to the obstacle will have diffusion of particles restricted to a

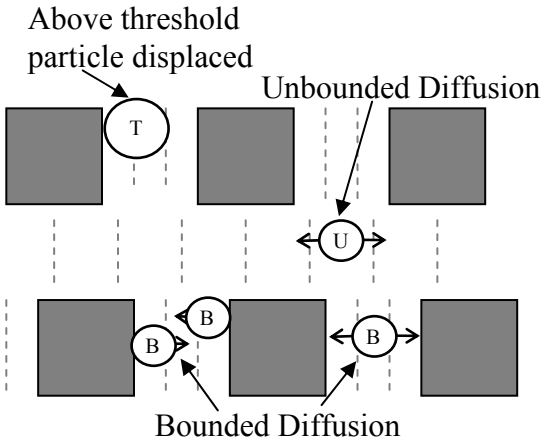

Figure 7-2: Representation of the model used to study the performance of the device. Some of the assumptions are illustrated with the model, i.e. square posts, equivalent width streamlines, and the division into unbounded and bounded regions of diffusion. Both central and edge diffusion are shown. Edge diffusion can only occur in the bounded region.

single direction, away from the obstacle. So we will define each streamline within the device as either a central streamline in which diffusion is possible in either direction, or an edge streamline with diffusion restricted to a single direction. The unbounded region will consist of only central streamlines, while the bounded region consists of a combination of both types.

As the second approximation, the model will assume plug flow, which gives the constant average velocity in each of the bounded (V_B) and unbounded (V_U) regions, which are related from the geometry by

$$V_B = V_U*\{G+P\}/G. \qquad (7\text{-}5)$$

Third, the further simplifying assumption of a constant streamline width of λ/N and G/N is made for the unbounded and bounded regions, respectively. The fluid velocity

distribution and streamline width is more complex, because the flow is not orthogonal to the posts but rather varies with both the length of the gap and post regions. Further, this ignores the assumed boundary condition of zero velocity at the walls, which is true for all pressure driven flow, and alters the width of the streamlines near the walls. However, it is the intent herein to create a tractable first order model to demonstrate the dominant physical direction in the bounded versus the unbounded region. These second order effects would be better modeled with a complete finite element analysis solving the underlining Navier-Stokes equation, a direction of future research within the Austin Lab.

7.2.2 Modeling of Exchange between Streamlines due to Diffusion

Within each row, the first effect modeled is the displacement caused by the post. All particles greater than critical radius r_c that are located in the first streamline to the right of each post are displaced into the next streamline to the right, with the critical size determined by equation 2-22. This is the ideal behavior.

The non-ideal behavior is modeled by solutions to the diffusion equation. We have discussed diffusion in streamlines of two types, central and edge. For the central streamlines, the incoming particle is assumed to be located at the center of the streamline for simplicity, and therefore a lateral diffusion of more than half the streamline width (W/2), will place the particle into an adjacent streamline. The probability (P_C) or particle density of a particle diffusing into an adjacent streamline as shown in figure 7-3A is calculated by solving the diffusion equation and evaluating

$$P_C = \int_{W/2}^{\infty} \frac{1}{\sqrt{4\pi D_{dif} t_c}} e^{-x^2/4D_{dif}t_c} dx \qquad (7\text{-}6)$$

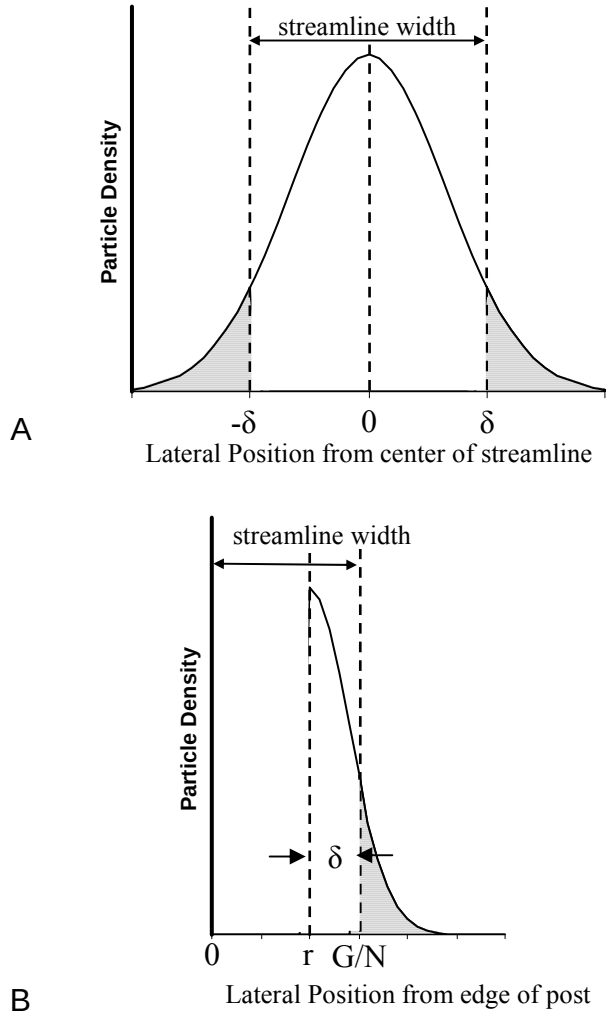

Figure 7-3: Representation of the model used to study the performance of the device. A) The particle density versus position at the end of the unbounded region, for a particle entering the region at x=0. B) The particle density versus position at the end of the bounded region, for a particle entering the region at x=r, a radius away from the post. For both graphs, δ is the position the particle must move to reach the next streamline, and the shaded region is the particle density which has moved to an adjacent streamline

where D_{dif} is the diffusion constant calculated from equation 7-2 for a given particle size r_p, μ is the viscosity, and t_c is the time spent in that region (distance between the posts for unbounded, and post length for bounded). Because of symmetry, P_C is the probability of

moving from a streamline z into streamlines z+1 and also into z-1, at each region. This equation is used for all diffusion within the unbounded region, where $t_c = G/V_U$, and $W = \lambda/N$. Additionally, it models the central streamlines of the bounded region where $t_c = G/V_B$, and $W = P/N$.

The diffusion of particles in the edge streamlines needs to be altered to take into account the obstacles. Diffusion on particles in the first and last streamline, because of the posts, can only move particles toward the center of the gap. Additionally, the particles just under the critical size will be too large to be centered at the middle of the gap in this region, and will be bumped to have a center one radius away from the left wall, when entering this region. Thus they only have to diffuse a smaller amount to move to the next streamline, a streamline width minus their radius (W – r). This probability is called the edge diffusion probability and is given as P_E and shown in figure 7-3B:

$$P_E = \int_{W-r}^{\infty} \frac{2}{\sqrt{4\pi D_{dif} t_E}} e^{-x^2/4D_{dif}t_E} dx \qquad (7\text{-}7)$$

where the time in this region is t_E. This integral gives the probability that a particle diffuses toward the center of the gap, i.e. a central streamline from an edge streamline. Within the bounded region, the only region in which the edge streamlines are located, $W = G/N$ and $t_E = P/V_B$.

Two additional approximations are important to note. First, all particles bumped or diffused to the next streamline are assumed to enter the next row at the center of the new streamline. In this way, the flow of particles can be followed through the array, yielding a two dimensional probability density function giving the density of particles versus horizontal location at each row as the particles move though the device. Second, the

diffusion coefficient is independent of location, as described in equation 7-2. However, particles in this size range are found to have a decrease in the diffusion constant near obstacles because fluid that a diffusive particle displaces has the freedom to move[72]. These have been neglected within the model.

7.2.3 Model Results

A number of simulations were run to analyze the various design parameters, and measure their effects on device performance. From the pdf, the average displacement of a particle was calculated, as well as the particle distribution width (standard deviation). Within these models, we were able to turn on and off diffusion in each of the two regions, in order to see their individual effects. An example result is shown in figure 7-4. This device consists of a single array with of gap size of 800 nm, shift fraction of 0.1, and a gap to post ratio of 1 which gives a critical diameter threshold of about 200 nm. It is observed that each of the two modes of diffusion produces a different effect.

7.2.4 Unbounded Diffusion

First let us consider the case of only unbounded diffusion. When only the unbounded diffusion is present there is an overall decrease in the efficiency of bumping, leading to their average displacement of $\theta < \theta_S$ (figure 7-4A). Diffusion in the unbounded region causes a general mixing between streamlines. Particles below the critical size, which are unaffected by the asymmetry, diffuse equally in both directions, as shown in figure 7.5A. Therefore, the average position of these sub-threshold particles is unaffected by this unbounded diffusion.

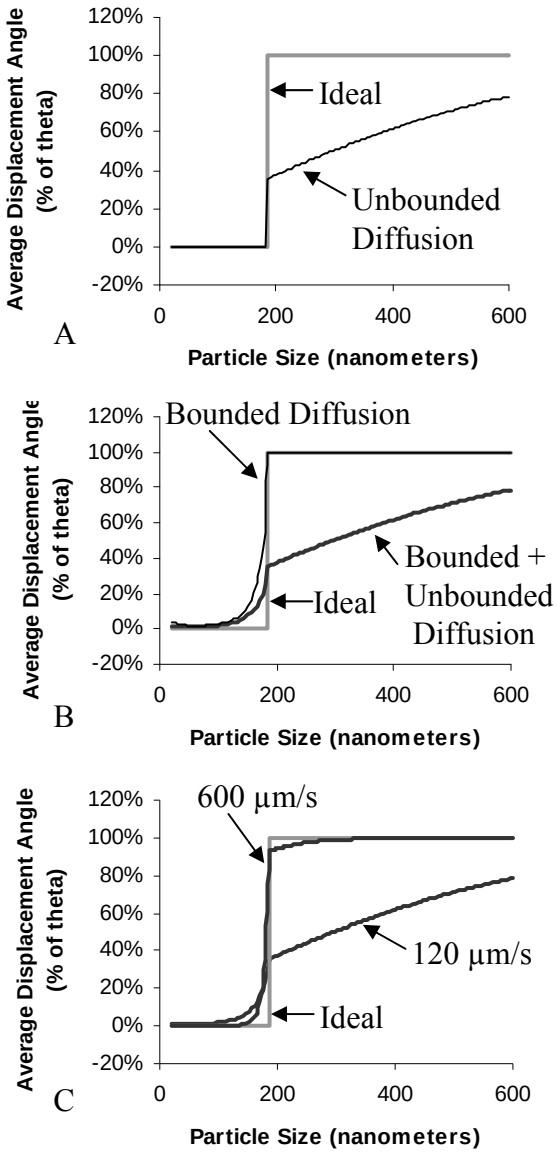

Figure 7-4: Simulations constructed using the model to analyze various forms of diffusion, with the ideal case as a reference. A) Only the unbounded diffusion is active. B) Only the bounded diffusion is active in one case, and both diffusions are active in the other. C) The model is evaluated at two different speeds, showing how diffusion's effect on performance can be overcome.

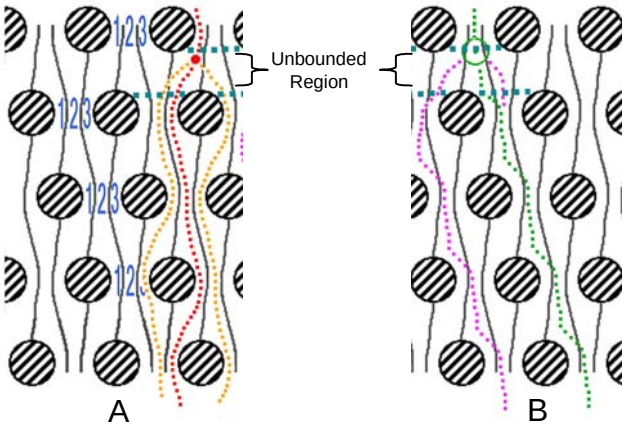

Figure 7-5: Picture of possible diffusional paths for A) a sub-threshold particle and B) a particle larger than the threshold, both within the unbounded region. The small particle density will broaden but maintain the same average position. The large particle density will decrease in average displacement because diffusion into the left streamline by a displaced particle will result in a decrease in performance.

Particles above the critical size will have different affects depending on the direction of diffusion. If a particle in streamline 1 (as determined by the streamline position in the next gap) moves to the right (to streamline 2), it simply has the same effect that would be caused by displacing into the next gap, shown by the short purple line to the right in figure 7.5B. If it did not diffuse, it would have shifted from streamline 1 to 2 at the next gap anyway. However; if it moves from streamline 1 to the left in the unbounded region (to streamline N), it will not shift in the upcoming gap, and this decreases the average angle at which the particle travels, shown by the long purple line to the left in figure 7.5B. Device performance is degraded, because these particles will have to have travel N-1 rows before they begin moving in the shifting mode, or displacing again.

7.2.5 Bounded Diffusion

Conversely, when only the bounded diffusion occurs (the diffusion next to the walls in the gaps), particles above the threshold are not adversely affected, as seen in figure 7-4B. However, particles slightly below the threshold are observed to have a non zero average displacement. The large particles are not able to be located in the first or last streamline, next to the posts, as they are too big, as shown in figure 7-6A, therefore they are not effected by the bound diffusion. For particles below the threshold, let's consider the leftmost streamline between the gaps, as shown in figure 7-6B. The particle can not diffuse left because of the post, and therefore can only diffuse right, into the second streamline. Thus it will not zigzag into the Nth streamline after the next row of posts, and has moved as if it has effectively been displaced by the post.

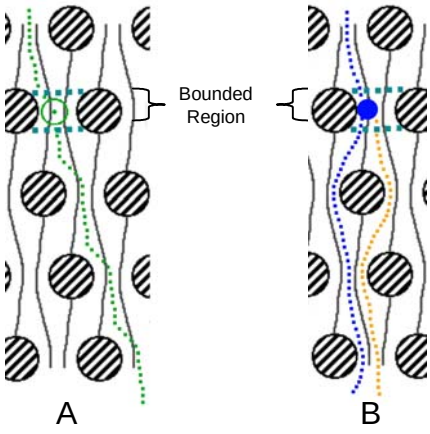

Figure 7-6: Picture of possible diffusional paths for A) a particle larger than the threshold and B) a particle slightly smaller than the threshold, both within the bounded region. The large particle density will be unaffected by the bounded region. The small particle density will broaden because diffusion limited to the direction of displacement is favored.

Similarly, bounded diffusion causes a particle in streamline N to move to streamline N-1. However, the combination of these diffusion directions of a bounded particle does not cancel because of the asymmetry of the array. The particle that diffused from the first streamline to the second will be subject to this effect in the subsequent gap, while the particle moving from the Nth to the Nth-1 streamline, must travel multiple rows before it is positioned next to the post again. Thus bounded diffusion causes sub-threshold particles to travel through the array with a greater than zero average separation angle.

This effect is highly dependent on the post to gap ratio. A larger post to gap ratio will have a larger relative bounded diffusion time period, and hence a larger sub threshold displacement.

It is important to note the role the velocity of the fluid plays in both of these effects. Since both diffusional effects are dependent on the time spent in each region, increasing the overall velocity enhances performance. Figure 7-4C shows the improvement of a 5-fold increase in velocity from 120 micron/sec to 600 micron/sec on the device described in this section, leading from what might be considered a "poor" performance to "near ideal" performance.

7.2.6 Scaling Analysis

Extending this analysis by a scaling approach gives a set of design criteria that can be used to design arrays for applications of arbitrary size. The Peclet number discussed in section 7.1.1, and equation 7-4 describes the width of diffusional broadening. As the device is scaled down, it is the Peclet number which needs to be maintained. This will keep the ratio of the advection rate to the diffusion rate fixed, so the same fraction of

particles will change streamlines. Thus a model for one velocity at one size can be used to predict performance at a different size.

As the diffusion increases at smaller scales a higher velocity is needed to increase the rate of advection by the same amount. For this approach, consider all lengths scaled by a constant C. For example, the post, P and gap, G will be replaced by P/C and G/C, r_C will be replaced by r_C/C, the shift fraction ε remains unchanged, so streamline widths and lengths will also scale as 1/C. Therefore the characteristic advection length L will be replaced by L/C. Since the diffusion constant D is inversely proportional to the particle size, as stated in equation 7-2, it scales to D*C. Using equation 7-3, in order to obtain the scaling factor necessary to have a constant Peclet number,

$$Pe = \frac{v\,L}{D_{dif}} = \frac{v'\,L'/C}{D'_{dif}\,C} \qquad (7\text{-}8)$$

the scaled velocity must be

$$V' = VC^2 . \qquad (7\text{-}9)$$

Note the relative threshold, or a particle size divided by the critical particle size, is independent of C; that is, as the design is scaled, the relative threshold does not change. This allows the presentation of curves for a few values of shift fraction, and the development of the necessary scaling to expand that situation in various sizes. These curves allow the reader to estimate the velocity necessary for a desired level of performance for a given size separation. The curves are graphed dimensionlessly, fixing all but two variables, and shown in figure 7-7A-D. One must simply choose a value of C that matches the desired design criteria.

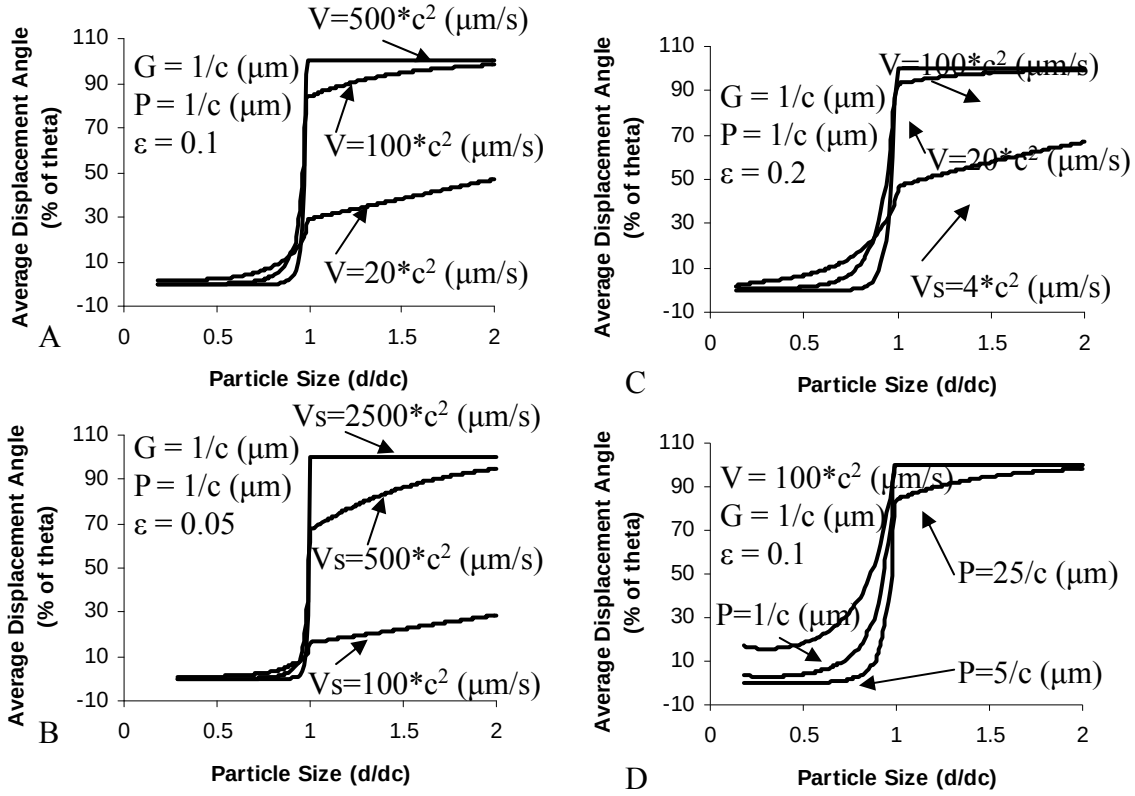

Figure 7-7: A set of curves for the design of DLD devices scaled to arbitrary size. The average displacement angle divided by the ideal is plotted versus particle size divided by the critical particle size in each case. G and P represent gap and post size, and v is the average velocity. C is a scaling factor. The average displacement caused by diffusion effects, versus r/r_C remains constant as the array is scaled down (C>1) if the average fluid velocity is increased by c^2. A-C) Three different shift fractions are shown to allow for three different size designs with a single gap size. D) The effects of Post to Gap Ratio on performance.

For example, start with a shift fraction of 0.1 and a post to gap ratio of 1 as shown in figure 7-7A. With C equal to 1, the gap size is 1 micron and a velocity of 500 micron/sec

is needed for good performance. If the C is increased to 2, the gap size decreases to 500 nm, and the velocity needed is increased to 2 mm/sec.

One only needs to calculate the velocity necessary in the most critical region (smallest shift fraction and critical size) in order to see if a particular design is feasible. For example the device with a 400 nanometer gap in figure 7-4C needs an increase in speed from 100 to 625 micron/sec, to improve the performance. It is import to note the clear critical parameter for device performance is velocity, which is stressed in these figures and equations.

7.2.7 Broadening Analysis

For this device, additional analysis was completed to better understand the effects particle density spreading or broadening. Figure 7-8 compares the model's solution of the width of the particle density to the solution of equation 7-4, (an equation estimating diffusion broadening as $(D_{dif}\,t)^{1/2}$. The model clearly shows three regions of interest. Region I shows those particles that are significantly smaller then the threshold of the region. In this region the model slightly underestimates the expected diffusion, an artifact of the resetting effect. In region III, a bumping particle was found to have a very low width, significantly lower then the $D_{dif}\,t$ value. However, this is not an artifact, but an advantage of the displacement at the post, actually resetting the amount of diffusion which may have occurred. In region II, particles very close to the threshold have the greatest probability of diffusion. Therefore this size range is going to be much more greatly disbursed.

As particles pass through successive regions with different thresholds, they will pass through each of these different effects. While the particle is still above the threshold it

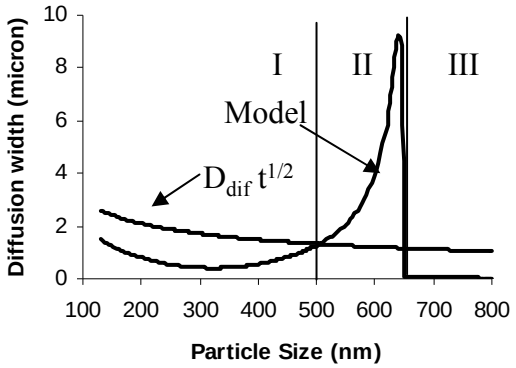

Figure 7-8: Diffusion width predicted by the model compared to standard diffusion of (Dt)½.

will be deterministically displaced, and the dispersion will be very low. When the particle is in a region near the threshold, it enters a region of greatest dispersion. Finally, after this region, the particle is in zigzag mode and disperses as expected with an amount of about $(D_{dif}\, t)^{1/2}$ (underestimated by reset of model). In summary, displacing particles diffuse less, if at all, within a device, and non-displacing particles diffuse as expected. The transition between these two modes passes through a region of significant diffusion.

8 Conclusion

The separation of a heterogeneous blood mixture into individual blood components by size is an important step in furthering our understanding of blood. The deterministic lateral displacement technique is a novel separation method with many applications. Two primary goals were set forth in the abstract: the first of which was the separation of blood components based on size, and the second was better understanding of the deterministic lateral displacement device.

Herein, the DLD technique has been explained, including its basic operation and interfaces. From an analysis of the Reynolds number, a laminar flow approximation was made. The Navier-Stokes equation was used to solve for the velocity profiles within the device. The critical parameters and equations to design a DLD device were developed and compared to simulation and experiment.

With a basic understanding of the DLD technique, a number of different types of devices were designed. Different modes of analysis such as fractionation and preparative modes as well as multiple, chirp and cascade style devices have been discussed. Each design included a discussion of the array as well as the input and output parameters for a complete device. A dynamic range for each device was defined, such that a continuous flow device is possible for more heterogeneous mixtures.

With a completed design, fabrication was presented in great detail for ease in repeatability by the reader. The microfluidic procedures usable across the wide variety of experiments with different microfluidic designs and different blood cells are discussed, with additional emphasis on particular observations of the author, so as to minimize

future mistakes. The other blood analysis techniques of hemocytometry and flow cytometry are explained.

I have shown the DLD can be used to separate the white blood cells, red blood cells and platelets. The fractionation and isolation of whole blood components occurred within a continuous flow deterministic array. The size of white blood cells has been measured and calibrated with beads, and confirmed with changes in osmolarity. The flow cytometer was used to confirm the results of the DLD separation by conventional means, and to test the resolution of the resultant separation. Cell viability has been considered for future applications of the DLD design.

A number of different effects attributed to the non-rigid and non-spherical form of some blood cells were explored. The velocity dependence on the separation of red blood cells was discussed as a possible function of deformability, orientation and rotation within the post array. The velocity dependence of white blood cells, which are spherical, was attributed to cell deformation. This effect has been measured, and two different models were developed. The elastic model and the cortical tension model were both compared to existing data on white blood cells.

Diffusion effects within the deterministic device have been considered. A model was developed which explains a number of non-ideal observed results. The scaling factor was created to use the model to estimate the necessary velocity within future devices to overcome diffusion. As devices become smaller, the importance of diffusional effects increases and will be critical in the design of sub-micron devices.

The novel deterministic lateral displacement technique shows great promise because it can continuously separate particles smaller than the feature size of the array. It has

been successfully used as part of a blood analysis device, and I look forward to seeing its future applications to even smaller biological particles.

References

[1] D. J. Beebe, G. A. Mensing and G. M. Walker., "Physics and Applications of Microfluidics to Biology" *Annual Review of Biomedical Engineering* **4**, 261-286 (2002).

[2] S. C. Terry, J. H. Jerman and J. B. Angell, "Gas-chromatographic air analyzer fabricated on a silicon wafer" *IEEE Transactions in Electronic Devices* **26**(12), 1880-1886 (1979).

[3] A. Manz, N. Graber and H. M. Widmer, "Miniaturized total chemical-analysis systems - a novel concept for chemical sensing" *Sensors and Actuators B* **1**, 244-248 (1990).

[4] C. T. Wittwer, G. C. Fillmore and D. J. Garling, "Minimizing the time required for DNA amplification by efficient heat-transfer to small samples" *Analytical Biochemistry* **186**(2), 328-331 (1990).

[5] D. Schmalzing, N. Tsao, L. Koutny, D. Chisholm, A. Srivastava, A. Adourian, L. Linton, P. McEwan, P. Matsudaira and D. Ehrlich, "Toward real-world sequencing by microdevice electrophoresis" *Genome Research* **9**, 853-858 (1999).

[6] A. Wolff, U. D. Larsen, G. Blankenstein, J. Philip and P. Telleman, "Rare event cell sorting in a microfluidic system for application in prenatal diagnosis" in *Micro Total Analysis Systems Proceedings*, Banff, Canada, (1998).

[7] A.Y. Fu, C. Spence, A. Scherer, F.H. Arnold and S.R. Quake, “A Microfabricated Fluorescence Activated Cell Sorter” *Nature Biotechnology* **17**, 1109-1111 (1999).

[8] D. Erickson and D. Li, “Integrated microfluidic devices” *Analytica Chimica Acta.* **507**, 11-26 (2004).

[9] T. Vo-Dinh and B. Cullum, “Biosensors and biochips: advances in biological and medical diagnostics” *Fresenius' Journal of Analytical Chemistry* **366**, 540-551 (2000).

[10] H. A. Stone, A. D. Stroock and A. Ajdari, “Engineering flows in small devices: Microfluidics toward a lab-on-a-chip” *Annual Review of Fluid Mechanics* **36**, 381-411 (2004).

[11] Through the Microscope: Blood Cells – Life’s Blood [cited 04-24-2007; webpage] Available from: http://www.wadsworth.org/chemheme/heme/microscope/lymphocytes.htm

[12] G. W. Schmid-Schonbein, Y. Y. Shih and S. Chien, “Morphometry of human leukocytes” *Blood* **56**, 866-875 (1980).

[13] J. V. Dacie and S. M. Lewis, *Practical Haematology.* 2001, London: Churchhill Livingstone.

[14] Education Section of the National Red Cross Site. American Red Cross [cited 04-24-2007; webpage]. Available from: http://www.pleasegiveblood.org/education.

[15] L. Y. Yeo, J. R. Friend and D.R. Arifin, “Electric tempest in a teacup: The tea leaf analogy to microfluidic blood plasma separation” *Applied Physics Letters* **89**, 103516 (2006).

[16] J. Cheng,L. J. Kricka, E. L. Sheldon and P. Wilding, *Topics in Current Chemistry.* (215-231), A. Manz, H. Becker, *Microsystem Technology in Chemistry and Life Sciences.* 1998, Heidelberg: Springer-Verlag.

[17] S. J. Abramowitz, “DNA Analysis in Microfabricated Formats” *Biomedical Microdevices* **1**(2), 107-112 (1999).

[18] A. Boyum, “Separation of blood leucocytes, granulocytes, and lymphocytes” *Tissue Antigens* **4**, 269-274 (1974).

[19] J. P. Hester, et al. “Principles of blood separation and component extraction in a disposable continuous flow single stage channel” *Blood* **54**, (1979).

[20] D. Wachtel, et al. “Fetal cells in maternal blood: recovery by charge flow separation” *Human Genetics* **6**, 162-166 (1996).

[21] J. Busch, P. Huber, E. Pfluger, S. Miltenyi, J. Holtz and A. Radbruch, “Enrichment of fetal cells from maternal blood by high gradient magnetic cell sorting (double MACS) for PCR-based genetic analysis” *Prenatal. Diagnostics* **14**, 1129-1140 (1994).

[22] D. Ganshirt-Ahlert, M. Burschyk, H. Garristen, L. Helmer, P Miry, J. Horst, H. Schneider and W. Holzgreve, “Magnetic cell sorting and the transferring receptor as

potential means of prenatal diagnosis from maternal blood" *American Journal of Obstetrics and Gynecology*, 1350-1355 (1992).

[23] M. C. Cheung, J. D. Goldberg and Y. W. Kan, "Prenatal diagnosis of sickle cell anemia and thalassaemia by analysis of fetal cells in maternal blood" *Nature Genetics* **14**, 264-268 (1996).

[24] J. Guigan, "Method and apparatus for obtaining and delivering a predetermined quantity of plasma from a blood sample for analysis purposes" U.S. Patent No. 4,788,154 (1988).

[25] M. J. Pugia, J. A. Profitt, L. S. Schulman, G. Blankenstein and R.P. Peters, "Method and apparatus for separation of particles in a microfluidic device" U.S. Patent No. 7,094,354 (2006).

[26] K. H. Han and A. B. Frazier, "Continuous magnetophoretic separation of blood cells in microdevice format" *Journal of Applied Physics* **96** (10), 5797-5802 (2004).

[27] D. W. Inglis, R. Riehn, R.H. Austin and J. C. Sturm, "Continuous Microfluidic Immunomagnetic Cell Separation" *Applied Physics Letters* **85**(21), 5093-5095 (2004).

[28] A. Zhu and Y. Chen, "High-Voltage Capillary Zone Electrophoresis of Red Blood Cells" *J. Chromatogr. A* **470**, 251-260 (1989).

[29] T. Tsuda, N. Yamauchi and S. Kitagawa, “Separation of Red Blood Cells at the Single Cell Level by Capillary Zone Electrophoresis” *Analytical Sciences* **16**(8), 847-850 (2000).

[30] R. Carlson, Ph. D. Thesis, Princeton University (1997).

[31] J. Castelino, Ph. D. Thesis, Princeton University (2000).

[32] M. K. Araz, C. H. Lee and A. Lal, “Ultrasonic separation in microfluidic capillaries” in *Proceedings of the IEEE Ultrasonics Symposium,* 1, 1066-1069, (2003).

[33] H. Li and T. Kenny, “High speed particles separation using ultrasound for microTAS and lab-on-a-chip application” in *Annual International Conference of the IEEE Engineering in Medicine and Biology - Proceedings 26*, 1, 2631-2634, (2004).

[34] S. Kapishnikov, V. Kantsler and V. Steinberg, “Continuous particle size separation and size sorting using ultrasound in a microchannel” *Journal of Statistical Mechanics: Theory and Experiment* P010112 (2006).

[35] F. F. Becker, X. B. Wang, Y. Huang, R. Pethig, J. Vykoukal and P. C. Gascoyne, "Separation of human brest cancer cells from blood by differential dielectric affinity" *Proc. Natl. Acad. Sci. USA* **92**, 860-864 (1995).

[36] S. S. Shevkoplyas, Y. Tatsuro, L. L. Munn and M. W. Bitensky, “Biomimetic autoseparation of leukocytes from whole blood in a microfluidic device” *Analytical Chemistry* **77**, 933-937 (2005).

[37] C. Blattert, R. Jurischka, A. Schoth, P. Kerth and W. Menz, “Separation of blood in microchannel bends” in *Proceedings of SPIE - The International Society for Optical Engineering*, 5345, 17-25 (2004).

[38] R.H. Austin, N. Darnton, R. Huang, J. Sturm, O. Bakajin and T. Duke, "Ratchets: the problems with boundary conditions in insulating fluids" *Applied Physics A* **75**, 279-284 (2002).

[39] L.R. Huang, E.C. Cox, R.H. Austin and J.C. Sturm, "Tilted Brownian Ratchet for DNA Analysis" *Anal. Chem.* **75**(24), 6963-6967 (2003).

[40] P. Wilding, J. Pfahler, H. H. Bau, J. N. Zemel and L. J. Kricka, “Manipulation and flow of biological fluids in straight channels micromachined in silicon” *Clin. Chem.* **40**, 43-47 (1994).

[41] J. P. Brody, T. D. Osborn, F. K. Forster and P. Yager, “A Planar Microfabricated Filter” *Sens. Actuators, A* **54**, 704 (1996).

[42] P. K. Yuen, L. J. Kricka, P. Fortina, N. J. Panaro, T. Sakazume and P. Wilding, “Microchip Module for Blood Sample Preparation and Nucleic Acid Amplification Reactions” *Genome Research* **11**, 405-412 (2001).

[43] Mohamed, H. et al., “Development of a rare cell fractionation device: application for cancer dectection” *IEEE Trans. Nanobioscience* **3**, 251-256 (2004).

[44] Panaro, N. J. et al., ”Micropillar array chip for integrated white blood cell isolation and PCR” *Biomolecular Engineering* **21**, 157-162 (2005).

[45] Huang, L. R., Cox, E.C., Austin, R.H. and Sturm J. C., “Continuous particle separation through deterministic lateral displacement” *Science* **304**, 987-989 (2004).

[46] J. A. Davis, D. W. Inglis, K. J. Morton, D. A. Lawrence, L. R. Huang, S. Y. Chou, J. C. Sturm and R. H. Austin, “Deterministic hydrodynamics: Taking blood apart” *PNAS* **103**, 14779-14784 (2006).

[47] S. Zheng, R. Yung, Y. Tai and H. Kasdan, “Deterministic lateral displacement MEMS device for continuous blood cell separation” in *18th IEEE International Conference on Micro Electro Mechanical Systems*, Miami Beach, Florida, 851-854 (2005).

[48] S. Zheng, Y. Tai and H. Kasdan, “MEMS Device for Continuous Blood Cell Separation” in *Proceedings of microTAS*, Boston, Massachusetts, 385-387 (2005).

[49] D. W. Inglis, J. A. Davis, R.H. Austin and J.C. Sturm, “Critical particle size for fractionation by deterministic lateral displacement” *Lab on a Chip* **6**, 655-658 (2006).

[50] A.J. Smits, *A Physical Introduction to Fluid Mechanics*. 2nd Ed. 2000, New York: Wiley & Sons.

[51] G. Korvacs, *Micromachined Transducers Sourcebook.* 1998, New York: WCB/McGraw-Hill.

[52] K. Foster and G. A. Parker, *Fluidics: Components and Circuits*. 1970, New York: Wiley Interscience.

[53] P. F. Davies, "Flow-mediated endothelial mechanotransduction" *Physiological Review* **75**, 519-560 (1995).

[54] C. P. Cheng, D. Parker and C. A. Taylor, "Quantification of wall shear stress in large blood vessels using lagrangian interpolation functions with cine phase-contrast magnetic resonance imaging" *Annals of Biomedical Engineering* **30**, 1020-1031 (2002).

[55] D. W. Inglis, "Microfluidic Devices for Cell Separation" Ph. D. Thesis, Princeton University (2007).

[56] S.I. Ertel, B.D. Ratner, and A. Kaul, *et al.* "In vitro study of the intrinsic toxicity of synthetic surfaces to cells." *J. Biomed. Mater. Res.* **28**, 667-675 (1994).

[57] F. Laerme, A. Schilp, K. Funk and M. Offenberg, "Bosch deep silicon etching: improving uniformity and etch rate for advanced MEMS applications" *Twelfth IEEE International Conference on Micro Electro Mechanical Systems*, 211-216 (Jan. 1999)

[58] PRISM Equipment List. Princeton University [cited 02-23-2008; webpage]. Available from: http://www.prism.princeton.edu/PRISM_cleanroom/equiplist.htm.

[59] T. McPherson, A. Kidane, I. Szleifer and K. Park, “Prevention of protein adsorption by tethered poly(ethylene oxide) layers: experiments and single chain mean-field analysis” *Langmuir* **14**, 176-186 (1998).

[60] J. P. Robinson, *Handbook of Flow Cytometry Methods.* Purdue University, West Lafayette, Indiana: Wiley-Liss 1993.

[61] H. M. Shapiro, *Practical Flow Cytometry.* Hoboken, New Jersey: John Wiley & Sons, Inc, 2003.

[62] T. C. Dombroski, L. Cisneros, S. Chatkaew, R.E. Goldstein and J.O. Kessler, “Self-Concentration and Dynamic Coherence in Bacterial Dynamics” *Phys. Rev. Lett.* **93**, 098103 (2004).

[63] S. C. Gifford, M. G. Frank, J. Derganc, C. Gabel, R. H. Austin, T. Yoshida and M. W. Bitensky, “Parallel Microchannel-Based Measurements of Individual Erythrocyte Areas and Volumes” *Biophysical Journal* **84**, 623-633 (2003).

[64] E. Evans and A. Yeung, “Apparent viscosity and cortical tension of blood granulocytes determined by micropipette aspiration” *Biophysical Journal* **56**, 151-160 (1989).

[65] E. B. Lomakina, C. M. Spillmann, M. R. King and R. E. Waugh, “Rheological Analysis and Measurement of Neutrophil Indentation” *Biophysical Journal* **87** 4246-4258 (2004).

[66] M. J. Rosenbluth, W. A. Lam and D. A. Fletcher, “Force microscopy of nonadherent cells: a comparison of leukemia cell deformability” *Biophysical Journal* **90**, 2994-3003 (2006).

[67] H. C. Kan, H. S. Udaykumar, W. Shyy and R. Tran-Son-Tay, “Hydrodynamics of a compound drop with application to leukocyte modeling” *Phys. Fluid* **10**, 760 (1998).

[68] W. Shyy, M. Francois, H. S. Udaykumar, N. N’dri and R. Tran-Son-Tay, “Moving boundaries in micro-scale biofluid dynamics” *Appl. Mech. Rev*. **54**, 405 (2001).

[69] L. D. Landau and E. M. Lifshitz, *Theory of Elasticity*. 1970, Oxford: Pergamon Press.

[70] R. Tran-Son-Tay, D. Needham, A. Yeung and R. M. Hochmuth, “Time-dependent recovery of passive neutrophils after large deformation” *Biophysical Journal* **60**, 856-866 (1991).

[71] M. A. Tsai, R. S. Frank and R. E. Waugh, “Passive Mechanical Behavior of Human Neutrophils: Power-law Fluid” *Biophysical Journal* **65**, 2078-2088 (1993).

[72] E. R. Dufresne, T. M. Squires, M. P. Brenner and D. G. Grier, “Hydrodynamic Coupling of Two Brownian Spheres to a Planar Surface” *Physical Review Letters* **85,** 3317 (2000).

Appendix

Publications and Presentations Resulting from this Work

Journal Publications

J. A. Davis, D. W. Inglis, R.H. Austin, and J. C. Sturm, "Effect of blood cell deformability on fractionation by deterministic lateral displacement", manuscript in preparation.

J. A. Davis, D. W. Inglis, S. L. Chi and J. C. Sturm, "Diffusional effects in a deterministic lateral displacement device", manuscript in preparation.

D. W. Inglis, K. J. Morton, J. A. Davis, T.J. Zieziulewicz, D.A. Lawrence, R.H. Austin, and J. C. Sturm, "Microfluidic device for label-free measurement of platelet activation". *Lab on a Chip* **8**, 925-931 (2008).

J. A. Davis, D. W. Inglis, K. J. Morton, D. A. Lawrence, L. R. Huang, S. Y. Chou, J. C. Sturm and R. H. Austin, "Deterministic hydrodynamics: Taking blood apart" *PNAS* **103**, 14779-14784 (2006).

D. W. Inglis, J. A. Davis, R.H. Austin and J.C. Sturm, "Critical particle size for fractionation by deterministic lateral displacement" *Lab on a Chip* **6**, 655-658 (2006).

Conference Presentations

J. A. Davis, D. W. Inglis, S. L. Chi, J. C. Sturm and R. H. Austin, "Diffusion effects on fractionation by deterministic lateral displacement in a microfluidic device." 2007 MRS Symposium, San Francisco CA.

J. A. Davis, D. W. Inglis, J. C. Sturm and R. H. Austin, “Continuous separation of serum from human whole blood within a microfluidic device” 2006 APS March Meeting, Baltimore MD.

J. A. Davis, D. W. Inglis, K. J. Morton, D. A. Lawrence, L. R. Huang, S. Y. Chou, J. C. Sturm and R. H. Austin, “Continuous separation of human blood components through deterministic lateral displacement” 2005 APS March Meeting, Los Angeles CA.

Patent Applications

D. W. Inglis, J. A. Davis, J. C. Sturm and R. H. Austin, “Apparatus and method for continuous particle separation” Application #60/809,933 filed on June 1, 2006.